UNIVERSIDAD DE MÁLAGA
DEPARTAMENTO DE QUÍMICA ANALÍTICA

UNIVERSIDAD
DE MÁLAGA

TIME-OF-FLIGHT MASS SPECTROMETRY EXPERIMENTAL STUDIES ON THE ONSET OF LASER-GENERATED IONS UNDER SUBTHRESHOLD PLASMA FORMATION REGIME

TESIS DOCTORAL

José Francisco Alcántara Leiva

Málaga, 2010

TIME-OF-FLIGHT MASS SPECTROMETRY EXPERIMENTAL STUDIES ON THE ONSET OF LASER-GENERATED IONS UNDER SUBTHRESHOLD PLASMA FORMATION REGIME

por

José Francisco Alcántara Leiva

José Javier Laserna Vázquez
Catedrático de Química Analítica
Universidad de Málaga

José Miguel Vadillo Pérez
Profesor Contratado Doctor
Universidad de Málaga

Memoria presentada para optar al grado de Doctor en ciencias (Química)

José Francisco Alcántara Leiva
Málaga, 17 de enero de 2010

José Javier Laserna Vázquez, catedrático de química analítica de la Universidad de Málaga y **José Miguel Vadillo Pérez**, profesor contratado Doctor del departamento de química analítica de la Facultad de Ciencias de la Universidad de Málaga,

CERTIFICAN

que el presente trabajo titulado TIME-OF-FLIGHT MASS SPECTROMETRY EXPERIMENTAL STUDIES ON THE ONSET OF LASER-GENERATED IONS UNDER SUBTHRESHOLD PLASMA FORMATION REGIME ha sido realizado por el licenciado **José Francisco Alcántara Leiva** en los laboratorios del Departamento de Química Analítica bajo nuestra dirección, reuniendo a nuestro juicio los requisitos necesarios para optar al grado de Doctor en Químicas, por lo que autorizamos su presentación.

Málaga, 17 de enero de 2010

Agradecimientos

Esta tesis se ha desarrollado en el Laboratorio Láser de la Universidad de Málaga (UMA), al que doy gracias por haberme aceptado como estudiante de doctorado y haber creído en mis posibilidades. Especialmente, quiero agradecer a Javier Laserna y a José Miguel Vadillo, pues juntos han dirigido mis pasos a lo largo de esta tesis, han guiado esta investigación y me han apoyado durante el desarrollo de este trabajo.

Además del trabajo desarrollado en Málaga, he tenido la fortuna científica de realizar estancias breves en centros de investigación tan reputados como ISAS Dortmund (Alemania), integrado en el grupo de *Materialanalytik* dirigido por el Prof. Kay Niemax, y ETH Zürich (Suiza), donde trabajé dentro del *Laboratorium für Organische Chemie* dirigido por el Prof. Renato Zenobi. Los meses que pasé en Dortmund durante 2007 y en Zürich durante 2008 representaron no solamente una experiencia personal gratificante y de la que me traje amigos y buenos recuerdos, sino una oportunidad única de aprender y desarrollar mi labor investigadora rodeado de un equipo científico exquisito. Por ello quiero agradecer a Kay Niemax y a Roland Hergenröder por aceptarme como investigador en ISAS y a Renato Zenobi por mi paso por ETH. Todos ellos depositaron en mí la confianza que demuestran a sus propios doctorandos y es por ello que quiero mostrarles mi más sincero agradecimiento, pues me permitieron desarrollar mi labor con todo el apoyo disponible.

Mención aparte al Ministerio de Educación y Ciencia, que financió mi doctorado con una beca dentro del plan de Formación de Personal Investigador que, además de permitirme crecer científicamente en el Laboratorio Láser de la Universidad de Málaga, me dio la posibilidad de realizar las tareas investigadoras anteriormente mencionadas en ISAS Dortmund y ETH Zürich.

No obstante, la realización de la tesis es un camino largo en el que,

más allá de las personas que han dirigido formalmente mi investigación, hay ocasión de tratar con muchas personas a las que, por una u otra causa, mostrar agradecimiento. A lo largo de este tiempo he tenido muchos compañeros a los que querria mencionar. Por las conversaciones, sus aportes, su colaboración querría agradecer a Jose Cuñat, Raquel, Pedro, Keith, Inma Suárez, Xavi, Javier Ruiz y Mari Carmen. De forma un tanto diferente, a quienes a lo largo de este tiempo han trabajado más cerca: Helena, con quien he compartido momentos agradables dentro y fuera del laboratorio, y Tomás, con quien tuve la ocasión de redescubrir algunas cosas en esta etapa final. Un lugar especial debo hacer a Fran por la dosis casi diaria de conversa, que fue siempre alta; a Carmen, porque estuvo ahí cuando todo comenzó en Málaga y no dejó nunca de ayudar durante el tiempo que compartimos en ISAS; y, por supuesto, a Ángel, porque antes que compañero siempre ha sido amigo.

Como ni siquiera durante la tesis la vida se reduce al laboratorio, sería injusto no mencionar a aquellos con quienes compartí momentos, alegrías y aventuras durante estos años, quienes en lo cotidiano de hacer de cada día y de cada noche algo diferente me ayudaron a descansar durante el tiempo que cubrió esta tesis, cuando mi cerebro ya no podía más. Sin la presencia todos estos años, pero muy especialmente en esta última y trepidante etapa, de Juan *Mahony*, Ana y mis amigos más cercanos, puede que nunca hubiera alcanzado el final de este sendero.

A menudo los éxitos personales se remontan hasta sus orígenes muy atrás en el tiempo. Por ello, el más especial de los huecos que reservé es, no podía ser de otra forma, para aquellos a quienes porto en mi nombre: esto va por mis padres, mis hermanas y toda mi familia. Sin ellos, nada de esto habría sucedido.

Sólo una vez más, gracias a todos.

"One has to do something new in order to see something new."

Georg Christoph Lichtenberg,
as excerpted by Wolfgang Paul in his Nobel Lecture (1989).

"I have described at some length the application of Positive Rays to chemical analysis; one of the main reasons for writing this book was the hope that it might induce others, and especially chemists, to try this method of analysis. I feel sure that there are many problems in chemistry, which could be solved with far greater ease by this than any other method. The method is surprisingly sensitive – more so than even that of spectrum analysis, requires an infinitesimal amount of material, and does not require this to be specially purified; the technique is not difficult if appliances for producing high vacua are available."

J. J. Thomson, *Rays of Positive Electricity*
and its Application to Chemical Analyses (1913).

Contents

Resumen

El análisis directo de sólidos en ausencia de manipulación en vía húmeda emergió como una herramienta importante al intentar observar la microestructura de una muestra, la cual define sus propiedades y aplicaciones. En comparación con el análisis convencional por vía húmeda, el uso de microsondas para realizar el análisis directo de sólidos repercute no solamente en la reducción del número de etapas en que se manipula la muestra, lo cual puede llevar a errores de medida reducidos, sino también en el tiempo efectivo requerido para realizar un análisis, que se reduce dramáticamente usando estos métodos.

De entre muchas otras técnicas de análisis con microsonda desarrolladas en las últimas décadas, las basadas en láser destacan debido a sus ventajas, incluídas la rapidez de análisis y despreciable daño a la muestra, así como por la simplicidad introducida por el láser en el montaje instrumental, haciendo innecesario el uso de complejos métodos de muestreo. Este hecho ha influido de forma dramática en la extensión de este tipo de técnicas, que son usadas actualmente en decenas de laboratorios de todo el mundo de forma rutinaria para llevar a cabo análisis de diversa y muy variada naturaleza.

De forma complementaria al desarrollo del láser y sus ventajas, la el-

evada sensibilidad de la espectrometría de masas y la disponibilidad de electrónica de alta frecuencia capaz de trabajar con la gran cantidad de datos experimentales producidos por los analizadores de tiempo de vuelo han ayudado a la extensión del uso de estos analizadores de iones en experimentos dedicados a obtener una comprensión del comportamiento del material eliminado de una muestra como consecuencia del proceso de interacción láser-materia. Por todo lo anterior, la Espectrometría de masas con ionización láser (LIMS, en su acrónimo en inglés, *Laser-ionization Mass Spectrometry*) es una de las más rápidas, fiables, sensibles y, por tanto, prometedoras técnicas láser, ampliamente usada para la obtención de información química de una muestra sólida.

Desde un punto de vista analítico, la utilización de una fuente de radiación láser no está exenta de desventajas. Las desventajas del uso del láser aplicado al análisis atómico aparecen como consecuencia de los mecanismos de eyección de material. Llamamos fraccionación a la ablación preferente de algunos elementos contenidos en una muestra objetivo como consecuencia de la irradiación con láser. La fraccionación produce desviaciones en el resultado del análisis. Parte del problema relacionado al análisis láser de sólidos es que los mecanismos de eyección de material no han sido completamente comprendidos y que los modelos actuales carecen de una explicación detallada y precisa para la interacción láser-materia.

La interacción de la radiación láser y la materia depende enormemente del material con el que interactúa el láser y de sus propiedades físicas. Estas diferencias entre materiales hacen posible el análisis directo de materiales sólidos que absorben la radiación láser y son modificados por ella, mientras para la realización de estos análisis se recurre a componentes transparentes al haz láser que nos sirven para redirigir el haz y controlar la energía total con la que se realiza el análisis. Que la acción de un pulso láser modifique la superficie y las propiedades físicas de un

sólido nos guía directamente a cuestionarnos qué sucedería si la energía de un pulso láser se distribuye en dos pulsos láser diferentes que alcanzan la superficie a analizar con un cierto retraso controlable, de forma que el segundo pulso encuentra una muestra que ha sido afectada por el anterior pulso.

Las consecuencias de este desacoplamiento del aporte energético que hacemos a la muestra que queremos analizar puede tener consecuencias como una disminución de la energía absoluta necesaria para realizar un análisis, o la disminución del daño superficial que se hace a la muestra. La disminución de los daños que se hacen a los sólidos que se analizan es otro parámetro de interés en el análisis directo de sólidos mediante ionización láser, ya que nos permitiría realizar análisis no sólo de sólidos másicos sino de materiales estructurados, obteniendo resultados que describan adecuadamente el problema que se quiere resolver. Una de las tendencias más novedosas que persiguen reducir el tamaño del cráter láser en la muestra problema incluye la utilización de una etapa de control nanométrico similar a la utilizada en la Microscopía óptica de barrido en campo cercano (*Scanning Near-field Optical Microscopy* o SNOM, por su acrónimo inglés). Estos instrumentos utilizan el efecto de intensificación de campos electromagnéticos que se produce cuando un sólido anisotrópico es situado a la vez en su frecuencia de resonancia y en las proximidades de otro sólido, no necesariamente anisotrópico.

En estos experimentos, una radiación láser de fluencia menor que el umbral de modificación superficial del sólido que estamos estudiando es enfocado sobre la superficie del mismo, de forma que la radiación electromagnética se vea perturbada por la presencia de un componente piezoeléctrico que hemos colocado muy cerca, a una distancia menor de $50\ nm$ y preferiblemente menor a $10\ nm$, de la superficie del mencionado sólido. Como consecuencia de esta disposición experimental, se producirá la intensificación local de los campos eléctricos y magnéticos aso-

ciados a la radiación láser, equivaliendo a un incremento *de facto* de la fluencia láser a escala muy local. Con este efecto, que se ve atenuado en distancias tan cortas como unos cientos de nanometros, se consigue confinar los efectos de la radiación láser en áreas pequeñas, de un tamaño menor al que se consigue habitualmente con métodos de enfoque convencional. Así, la información analítica –de haberla– proviene únicamente del pequeño área de la superficie del sólido que estamos estudiando. Este área puede ser tan reducida que en ocasiones podria ser menor que la mínima obtenible para una longitud de onda sin usar la interfaz SNOM, ya que con esta interfaz podemos confinar el haz láser en áreas menores a las predichas el principio de difracción y el límite mínimo de difracción.

De todo lo expuesto anteriormente, resulta clara la existencia de una necesidad, y un interés derivado de ésta, de mejora en las capacidades analíticas de las técnicas basadas en láser y, en particular, de la Espectrometría de masas con ionización láser. Eso incluye una comprensión correcta acerca de cómo se forman los iones, exista o no formación de plasma en el régimen de fluencias en el que llevamos a cabo el análisis, pero también incluye la investigación de la posible influencia de la matriz en la formación de iones, la ampliación de estos estudios al ámbito del análisis de compuestos orgánicos y el incremento de la resolución lateral del análisis mediante la reducción del daño infligido a la muestra.

Los trabajos descritos en esta memoria se han dedicado a estudiar algunos de los fenómenos comentados arriba y su influencia en el análisis de sólidos mediante Espectrometría de masas de tiempo de vuelo con ionización láser en ausencia de plasma láser. En los siguientes párrafos se describen brevemente los experimentos realizados, que son detallados en profundidad a lo largo de esta memoria, así como los resultados obtenidos en los mismos.

1. El primer capítulo de esta memoria sitúa a la Espectrometría de

masas con ionización láser en el contexto de otras técnicas láser utilizadas habitualmente con propósitos analíticos. La clasificación de las técnicas se realiza en base al régimen térmico de trabajo requerido por las mismas. Se diferencian, así, tres regímenes de trabajo principales: desorción, ionización en ausencia de plasma láser y ablación láser. En cada caso se realiza una breve descripción de técnicas representativas como pueden ser la Espectrometría de masas con desorción e ionización láser (MALDI, en su acrónimo inglés), la Espectroscopía de emisión atómica de plasmas láser (denotada habitualmente como LIPS o LIBS) y la Espectrometría de masas de plasma acoplado por inducción con ablación láser (LA-ICP-MS).

El segundo capítulo, complementando al primero, se dedica a glosar y describir los diferentes teóricos que describen el proceso de interacción entre el haz láser y la materia que se han manejado durante el desarrollo del trabajo. Dada la complejidad de estos procesos, la cantidad de factores que intervienen y el amplio rango de fluencias de trabajo que pueden considerarse, no existe un módelo que explique de forma eficaz la totalidad de los fenómenos observados, motivo por el cual se divide el proceso en pasos más pequeños para los que sí existen herramientas matemáticas, físicas y químicas capaces de dar base a modelos teóricos más o menos completos.

2. El tercer capítulo contiene la descripción de los diferentes sistemas experimentales utilizados a lo largo de la tesis, con los que se realizaron los estudios experimentales que se detallan en la segunda mitad de la memoria. La descripciíon sirve no sólo para detallar rigurosamente las peculiaridades del dispositivo experimental, que se adapta a cada experimento, sino para contextualizar la evoluciíon del instrumento mismo de trabajo, que durante el progreso de la

tesis ha visto cómo se le añadían una segunda fuente láser, un sistema de elementos ópticos que permite un mayor control sobre la energía utilizada en las medidas, un nuevo osciloscopio digital con el que adquirir los espectros de masas e, incluso, un software específico con el que almacenar y procesar los espectros en tiempo real o con posterioridad a la realización del experimento. Sin embargo, la descripción del experimental con el que se realizaron los experimentos de ablación láser en campo cercano han sido descritos en su propio capítulo, por ser un dispositivo experimental mucho más específico.

3. En primer lugar se llevó a cabo la determinación de los umbrales de formación de iones y formación de plasma mediante análisis de coincidencias LIMS/LIBS. En este experimento, se recoge simultáneamente la emisión óptica de la muestra tras el pulso láser y se analizan los iones formados como consecuencia de la acción de la radiación sobre la superficie del sólido. Este experimento apunta directamente a los parámetros del láser: cuánta energía es necesaria para llevar a cabo análisis LIMS? Como el daño infligido a la muestra depende de la energía láser depositada en la superficie, establecer una separación clara entre los regímenes de formación de iones y formación de plasma podría ser de ayuda a la hora de reducir el daño a las muestras.

   La transición del régimen térmico a un régimen con formación de plasma ha sido estudiada mediante la medición simultánea LIMS/LIPS y la búsqueda de paralelismos o diferencias en los comportamientos de estas señales. Aunque se ha encontrado que ambos procesos son diferentes, de ahí los diferentes valores umbral calculados para su aparición, se ha encontrado evidencia experimental de la naturaleza térmica tanto de la formación de iones como de la formación

de plasma.

4. Investigación de los efectos de matriz sobre el umbral de formación de iones previamente determinado, de forma que la posibilidad de análisis selectivo, así como la posibilidad de preparar el análisis de muestras complejas basándonos en los parámetros de referencia obtenidos para muestras más sencillas sea elucidada.

   Una comparación entre la fluencia umbral de ionización exhibida por un grupo de muestras metálicas puras y algunas de sus aleaciones (Ni/Cr, Fe/Ni, Fe/Cr/Ni, Fe/Cr, y bronce) ha sido realizada. El importante papel desempeñado por la matriz que rodea a los átomos en el metal y su influencia en el valor umbral para la formación de iones ha sido demostrado.

   Los resultados sugieren que mientras exista una mezcla apropiada de los componentes en la mezcla, la ionización selectiva de elementos concretos dentro de una matriz compleja no resulta factible. Adicionalmente, la influencia del tamaño de la huella láser ha sido evaluada. Los resultados experimentales muestran que al disminuir el tamaño de la huella láser, el valor de fluencia umbral para la formación de iones aumenta.

5. Estudio de los efectos sobre la señal y el daño de las muestras del desacoplamiento de la energía láser depositada sobre la muestra para formar iones. En concreto, el estudio de un conjunto de muestras metálicas usando dos pulsos con fluencia subumbral para realizar el muestro LIMS será desarrollado. La influencia del retraso entre pulsos sobre la señal analítica y la observación del daño realizado sobre las muestras será también objeto de estudio.

   Se han realizado experimentos de ionización de muestras metálicas y semimetálicas (Al, Cu, Fe, Si, Ti, y acero inoxidable AISI 314) uti-

lizando dos pulsos láser, con un retraso controlado entre ambos. Los experimentos sonda-prueba realizados con dos pulsos láser con longitud de onda visible ($532\ nm$) y colineales con fluencia subumbral demuestran la existencia de un retraso entre pulsos óptimo para el cual se alcanza un máximo en la señal de iones. Este máximo se encuentra cuando se utiliza un retraso entre pulsos de $60\ ns$. Además, se observó la presencia de otros efectos concomitantes a la aparición de ese máximo de señal, como el movimiento de las señales LIMS a menores tiempos de vuelo, que resultó ser mínimo para el retraso entre pulsos que ofrecía el máximo de señal.

Cuando dos pulsos láser con fluencia subumbral son enfocados sobre una muestra metálica, la respuesta obtenida para diferentes retrasos parece concordar con la secuencia de eventos que tienen lugar durante la interacción laser materia. Una hipótesis para este comportamiento podría estar relacionado con cambios en la muestra (rugosidad, temperatura, entre otros), como consecuencia de la acción del primer pulso láser. La duración de estas modificaciones podría variar de un material a otro y ese hecho podría ayudarnos a comprender las pequeñas diferencias observadas en el retraso óptimo para cada material.

6. Se realizaron análisis de materiales orgánicos energéticos. El conocimiento adquirido con los estudios previos, realizados sobre muestras inorgánicas, facilitó la obtención de un mayor control sobre el régimen térmico de trabajo seleccionado para realizar el análisis químico que será aplicado al análisis LIMS de muestras orgánicas en ausencia de plasma. Al evitar las altas fluencias necesarias para formar un plasma y disminuir la energía láser depositada efectivamente sobre la muestra, se permite la realización de un buen análisis de compuestos orgánicos energéticos con una cierta volatil-

idad. En condiciones energéticas que impliquen la formación de un plasma láser estos compuestos son completamente atomizados, desaprovechando las posibilidades que ofrece la Espectrometría de masas.

Los patrones de fragmentación del 2,6-DNT han sido estudiados con diferentes longitudes de onda. De entre las longitudes de onda utilizadas, los análisis de mayor calidad fueron obtenidos usando un haz láser de 266nm. El efecto de la anchura y el retraso del pulso de extracción han sido investigados y la posibilidad de realizar análisis con modulación de la señal obtenida en los cuales hay presente tanto información atómica como molecular ha sido demostrada.

7. La evaluación de la Ablación láser mejorada mediante campo cercano (NF-LA) como método de muestreo para técnicas de análisis químico basadas en ablación láser, como la Espectrometría de masas de plasma acoplado por inducción con ablación láser (LA-ICP-MS). El último capítulo experimental de la memoria describe los experimentos llevados a cabo en ISAS Dortmund (Alemania), con objeto de una estancia breve predoctoral. Este capítulo incluye una descripción de los fundamentos de esta técnica así como una detallada explicación del equipo instrumental utilizado durante los experimentos.

   El interés de acoplar la etapa de campo cercano a un instrumento LA-ICP-MS típico reside en la mejora potencial de la resolución lateral del análisis de sólidos, debido al confinamiento de los efectos de la radiación supra-umbral a un área pequeña, menor que el límite de difracción, como consecuencia de la acción de la nanosonda. Aunque en el momento en que se realizó nuestro trabajo experimental no habían sido demostrada la posibilidad de realizar estos análisis y en nuestros experimentos no fue posible culminar esa tarea pese a los

resultados obtenidos, actualmente sí que se ve más cercana la posibilidad de utilizar un dispositivo experimental similar al utilizado en estos experimentos para realizar análisis químico directo de sólidos con elevada resolución lateral.

Se realizaron experimentos de ablación láser con excelente resolución lateral utilizando un sistema SNOM para confinar el haz láser en una región de tamaño inferior al límite de difración. ésta es una aproximación novedosa para la mejora de la resolución lateral en el análisis directo de sólidos mediante espectrometría de masas con ablación láser, capaz de realizar análisis de sólidos con una huella láser que sea menor que el límite de difracción es posible. Aunque los experimentos realizados no consiguieron obtener espectros de masas, los resultados muestran que nuestra aproximación no es óptima y que la detección de iones sería posible, siempre que el sistema sea optimizado.

Scope

Direct analysis of solid samples in absence of wet manipulation emerged as an important tool when trying to observe the microstructure of a target, which is determining its properties and applications. When compared to traditional chemical wet analysis, the use of microprobes to perform direct analysis of solids repercutes not only in the reduction of manipulation steps, that may lead to reduced measurement errors, but also in the effective time required for analysis, that is dramatically decreased with these methods.

Among many other microprobe analysis techniques developed in the last decades, laser based are highlighted due to their many advantages, incluing fastness of analysis, negligible damage done to the sample, as well to the simplicity introduced by the laser in the experimental setup, making it unnecessary to use complex sampling methods. Complementary to the laser development and its advantages, the high sensitivity of the mass spectrometry and the availability of high-frequency electronics capable of managing the amount of experimental data produced by Time-of-Flight analyzers have helped to spread the use of these ion analyzers in experiments devoted to understand the behaviour of the material removed as a consequence of the laser-matter interaction process.

Hence, Laser-ionization Mass Spectrometry (LIMS) is one of the fast, reliable, sensible and, thus, promising laser techniques widely used to obtain chemical information of a solid target.

From an analytical point of view, disadvantages of the use of lasers when it comes to atomic analysis appear as a consequence of the material ejection mechanisms. Fractionation is the preferential ablation of some elements within a target as a consequence of laser irradiation. Fractionation results in biased analysis. Part of the problem regarding the laser analysis of solids is that the mechanisms of material removal are not completely understood, and that the current models lack of a detailed and precise explanation of the laser-matter interaction.

From the exposition above, it is clear that there exist an interest in improving the capabilities of Laser-based techniques and, in particular, that of Laser-ionization Mass Spectrometry. That includes a proper understanding on how the ions are formed, within or without a plasma formation, but also includes the investigation of the possible influence of the matrix on the ion formation. The aim of the work is detailed below:

1. Determination of the ion and plasma formation threshold of metals by LIMS/LIBS coincidence analysis. This points directly at the laser parameters: how much laser energy do we need to perform LIMS analysis? As the damage done to the target depends on the laser energy deposited on its surface, establishing a clear separation between the ion formation and the plasma formation regimes may help us reduce the damage done to it.

2. Investigation of the matrix effect on the ion formation threshold previously determined, so that the possibility of performing selective analysis or prepare analysis of complex targets based on the parameters of reference, simpler targets is evaluated.

3. Study the effect of the decoupling of laser energy utilized to form

ions on the ion signal and that used in sample damage. Precisely, analysis of a set of metallic samples by LIMS using two sub-threshold laser pulses will be made. The interpulse delay influence on the analytic signal will be studied and the overall influence of using two reduced-energy laser pulses to perform ionisation on the crater size will also be evaluated.

4. Analysis of highly energetic organic samples will be done. The knowledge achieved in the control of the thermal regime for the chemical analysis will be applied to the analysis of organic samples by LIMS without forming a plasma. The decrease of laser energy may lead to a good analysis of energetic organic samples that usually get completely atomized under plasma formation regime.

5. Evaluation of near-field enhanced laser-ablation to perform sampling for chemical analysis techniques as Laser-ablation Inductively Coupled Plasma Mass Spectrometry (LA-ICP-MS). The interest of coupling the near-field stage to a typical LA-ICP-MS instrument resides in the potential improvement of the lateral resolution, due to the confinement of the above-threshold radiation effects in a small area, smaller than the diffraction limit, as a consequence of the tip enhancement.

Objetivos

El análisis directo de sólidos en ausencia de manipulación en vía húmeda emergió como una herramienta importante al intentar observar la microestructura de una muestra, la cual define sus propiedades y aplicaciones. En comparación con el análisis convencional por vía húmeda, el uso de microsondas para realizar el análisis directo de sólidos repercute no solamente en la reducción del número de etapas en que se manipula la muestra, lo cual puede llevar a errores de medida reducidos, sino también en el tiempo efectivo requerido para realizar un análisis, que se reduce dramáticamente usando estos métodos.

De entre muchas otras técnicas de análisis con microsonda desarrolladas en las últimas décadas, las basadas en láser destacan debido a sus ventajas, incluídas la rapidez de análisis y despreciable daño a la muestra, así como por la simplicidad introducida por el láser en el montaje instrumental, haciendo innecesario el uso de complejos métodos de muestreo. De forma complementaria al desarrollo del láser y sus ventajas, la elevada sensibilidad de la espectrometría de masas y la disponibilidad de electrónica de alta frecuencia capaz de trabajar con la gran cantidad de datos experimentales producidos por los analizadores de tiempo de vuelo han ayudado a la extensión del uso de estos analizadores de iones en ex-

perimentos dedicados a obtener una comprensión del comportamiento del material eliminado de una muestra como consecuencia del proceso de interacción láser-materia. Por todo lo anterior, la Espectrometría de masas con ionización láser (LIMS, en su acrónimo en inglés) es una de las más rápidas, fiables, sensibles y, por tanto, prometedoras técnicas láser, ampliamente usada para la obtención de información química de una muestra sólida.

Desde un punto de vista analí[U+FFFD]tico, las desventajas del uso del láser aplicado al análisis atómico aparecen como consecuencia de los mecanismos de eyección de material. Llamamos fraccionación a la ablación preferente de algunos elementos contenidos en una muestra objetivo como consecuencia de la irradiación con láser. La fraccionación produce desviaciones en el resultado del análisis. Parte del problema relacionado al análisis láser de sólidos es que los mecanismos de eyección de material no han sido completamente comprendidos y que los modelos actuales carecen de una explicación detallada y precisa para la interacción láser-materia.

De la exposición arriba, resulta claro que existe un interés en mejorar las capacidades de las técnicas basadas en láser y, en particular, de la Espectrometrí[U+FFFD]a de Masas con Ionización Láser (LIMS, por su acrónimo inglés). Eso incluye una comprensión correcta acerca de cómo se forman los iones, con o sin formación de plasma, pero también incluye la investigación de la posible influencia de la matriz en la formación de iones. El objetivo de este trabajo se detalla debajo.

1. Determinación de los umbrales de formación de iones y formación de plasma mediante análisis de coincidencias LIMS/LIBS. Este experimento apunta directamente a los parámetros del láser: [U+FFFD]cuánta energí[U+FFFD]a es necesaria para llevar a cabo análisis LIMS? Como el daño infligido a la muestra depende de la energí[U+FFFD]a láser

depositada en la superficie, establecer una separación clara entre los regí[U+FFFD]menes de formación de iones y formación de plasma podrí[U+FFFD]a ser de ayuda a la hora de reducir el daño a las muestras.

2. Investigación de los efectos de matriz sobre el umbral de formación de iones previamente determinado, de forma que la posibilidad de análisis selectivo, así[U+FFFD] como la posibilidad de preparar el análisis de muestras complejas basándonos en los parámetros de referencia obtenidos para muestras más sencillas sea elucidada.

3. Estudio de los efectos sobre la señal y el daño de las muestras del desacoplamiento de la energí[U+FFFD]a láser depositada sobre la muestra para formar iones. En concreto, el estudio de un conjunto de muestras metálicas usando dos pulsos con fluencia subumbral para realizar el muestro LIMS será desarrollado. La influencia del retraso entre pulsos sobre la señal analí[U+FFFD]tica y la observación del daño realizado sobre las muestras será también objeto de estudio.

4. Se realizarán análisis de materiales orgánicos energéticos. El conocimiento adquirido con los estudios anteriores permitirá un mayor control sobre régimen térmico de trabajo seleccionado para realizar el análisis quí[U+FFFD]mico que será aplicado al análisis LIMS de muestras orgánicas en ausencia de plasma. El descenso de la energí[U+FFFD]a láser podrí[U+FFFD]a permitir un buen análisis de compuestos orgánicos energéticos, que generalmente son completamente atomizados en un régimen de formación de plasma.

5. La evaluación de la Ablación láser mejorada mediante campo cercano (NF-LA) como método de muestreo para técnicas de análisis quí[U+FFFD]mico basadas en ablación láser, como la Espectrometrí[U+FFFD]

de masas de plasma acoplado por inducción con ablación láser (LA-ICP-MS). El interés de acoplar la etapa de campo cercano a un instrumento LA-ICP-MS tí[U+FFFD]pico reside en la mejora potencial de la resolución lateral del análisis de sólidos, debido al confinamiento de los efectos de la radiación supra-umbral a un área pequeña, menor que el lí[U+FFFD]mite de difracción, como consecuencia de la acción de la nanosonda.

Chapter 1

Introduction and Scientific Context

1.1 Introduction

Since J.J. Thomson described the positively-charged ions as "rays of positive electricity",[1] the physical and chemical implications for the materials science raised by his work didn't stop growing, due to the scientific advances that came to unveil a whole new vision on matter and, consequently, the chemical diagnostic of matter. Few years later, in 1917, Einstein proposed a theory for the stimulated emission of radiation.[2] Again, the new perspective on how matter emits radiation was so advanced than many years were needed to get an application based on this theory.

In recent years, direct analysis of solids became an industry-driven requirement. As the design of new materials is getting increasingly complex and their function is progressively linked to its structure (distribution of constituents through the material) with lower tolerance to fabrication errors, the assessment of the exact structure of these materials is a matter of great economic interest. In this context, laser-based mass spec-

trometry has been described as one of the more promising tools for solid characterization.[3]

There is no perfect technique capable of offering a full description of any solid including atomic and molecular information, electric/magnetic properties, roughness, ... Instead, a full tree of spectroscopy techniques, each one giving a piece of the puzzle, has been developed to carry on these kind of analysis on any possible sample. We can be reasonably sure that the huge advances in materials science wouldn't be possible without the unprecedented blooming in the material analysis field achieved since the advent of microprobe analysis that allowed for localized analysis on complex targets.

Despite these advances, several decades were to be needed (until 1946) before the first time-of-flight analyzer was built.[4] Still a few more years (mid-1950s) were needed before the first laser was developed and tested, in 1960. This first laser was made out of Ruby and was first operated in 1960 by Theodore H. Maiman,[5] though, the concept of the laser had already been successfully tested in systems emitting lower energy photons, such as masers (microwaves). The maser was first presented by Charles H. Townes in 1955.[6] Townes had also stepped into the "infrared and optical masers", as he published in 1958, two years before Maiman published his now ubiquitous paper.[7] The maser system designed by Townes had a major problem: it couldn't be operated in continuus mode as it had a two-level excitation scheme. At the same time that Maiman was developing the Ruby laser, Nicolay G. Basov and Aleksandr M. Prokhorov had worked to solve the problem of the Maser described by Townes. Basov and Prokhorov developed a three-level aproximation that allowed a greater population inversion and also allowed the laser to be used in continuus mode. This scheme was also present in the ruby laser developed by Maiman. However, Townes, Basov and Prokhorov were awarded a shared Nobel Prize in 1964 for their effort in the field of

quantum electronics, while Maiman would never get this award.

Not surprisingly, as soon as the time-of-flight analyzer and the laser source were designed, the joint of lasers, mass spectrometry and analytical chemistry came along so that these devices improve the handset of resources that a chemist may use in order to get chemical and structural information out of a solid sample and first applications combining this three elements emerged. The first time this was accomplished was in the R. E. Hönig and J. R. Woolston experiments published in 1963,[8] three years later than the ruby laser discovery. Even though, the development of any laser-assisted Mass Spectrometry instrument was slow in the next years mainly due to two reasons. First, instability of the lasers in the pulse-to-pulse made them get hardly precise data. Second, laser technology was expensive. Nowadays, both the design of mass spectrometers and laser sources has evolved and made possible new and more precise applications at affordable prices.

The challenge for mass spectrometry advanced in many different directions. There were a lot of developments in the ionization step. In fact, the race for ion sources didn't stop during the whole 20^{th} century, leading to the development of many new ion sources apart from using laser radiation for ion formation. Starting from the simplest electronic impact for organic analysis,[9] a whole diversity of ion source including chemical ionization (CI) in 1966,[10] and Secondary-ion Mass Spectrometry (SIMS).[11] The latest ion source to add was the electro-spray ionization (ESI), firstly introduced in 1984,[12] that expanded dramatically during the decade of 1990, due to the many advantages it offers in the analysis of biological and biochemically active samples (metabolites, proteins, nucleic acids).

Despite this array of ion sources, since the arrival of lasers, they became a preferred ion source for some mass spectrometry setups. Nevertheless, it took only 3 years between the first laser being operated and

the first documented attempt by Hoñig and Woolston of coupling this new radiation source to a mass spectrometer. Still a decade was needed to see the first commercial instrument offering these elements coupled. It was the laser-microprobe mass analyzer (LAMMA) instrument.[13] In the LAMMA, ions formed by irradiation of the sample with a laser were then analyzed by time-of-flight mass spectrometry (ToF-MS) and, even though it had some scientific acceptance in the beginning, it was far from being a big commercial success and was soon replaced by softer-ionization approaches. Just a few years after the launch of LAMMA, a new major improvement in this field would happen. In the beginning of the decade of 1980, Michael Karas and Franz Hillenkamp were working in a new ionization source using lasers. They used a low energy laser pulse to make the ionization of the analites, that will usually get ionized by acquiring an extra proton from a reactive added to the medium.[14]

They called this technique matrix-assisted laser desorption/ionization (MALDI). After 20 years, MALDI has become a routine technique and a land of scientific and research fields has grown around it, due to its low-sample requirements, fast analysis, good resolution and even capabilites of getting structural information of big molecules as proteins or DNA/RNA sequences.[15, 16] We will pay more attention to MALDI in Section 1.3.

Not all applications of lasers and mass spectrometry involve solid analysis, as many problems solved with these tools concern the analysis of liquid and gas samples. However, this Memory will be centered on experiments studying the analysis of solid materials and the the laser-matter interaction process at moderate fluence, using an analytical point of view.

1.2 Introducing the Analysis: Energetic Regimes

The laser interaction with the solid depends on both the laser energy and its temporal profile. These two parameters determine not only the processes taking place, based on the different threshold fluence, but also how fast will it take for the changes in the solid to occur.

Different effects on the solid as a consequence of having a laser beam focused on its surface may range from a negligible excitation to explosive boiling of the target. If material removal is present, as it can be seen on Figure 1.1, the dominant effect in the laser-matter interaction will depend on the energetic input.

Modern applications of lasers can be divided attending to the permanent damage on the irradiated sample. Hence, a general distinction between applications not involving relevant and permanent physical changes to the irradiated material and the ones producing irreversible modifications can be done. In most cases, laser energy absorbed by the solid is dissipated through the thermal channel (solid heating). When a laser impinges a solid surface, consequences may include:

- Slight excitation of the surface with radiative and non-radiative emission and no permanent damage on the solid. Despite the fact that it can be spectroscopically measured, this excitation has no application in the field of mass spectrometry.

- Permanent damage to the solid due to heating of the surface without material affection. As it happens to the excitation-only interaction, these changes are sometimes measured by electron microscopy (inspection of bubbles and foaming formation) but are unlikely to be used for mass spectrometry as no material is being removed from the solid.

- Soft material removal through desorption. This is more likely to

occur in organic species and there's no need of the ionization of the species to occur. Neutral species will dominate, even though this ionization may be enhanced/provoked through proper design of the solid. As molecules are being desorpted from the surface, mass spectrometry information may be acquired.

- Material removal by normal boiling of the target. This process is dominant when the laser fluence is high enough to heat the target up to its boiling temperature but not high enough (and not fast enough) to make temperature rise too fast so that no sub-surface heating or explosive boiling can happen. Ions formed both in the boiling step and due to in-plume collisions may be detected by mass spectrometry.

- The highest energetic regime on the laser-matter interaction involves the material removal and the formation of a plasma plume within the ejected material. The mass removal per laser pulse is much higher than in the previous phenomena, as it is the average temperature of the formed plume. As a consequence, ions will be present in the ejected material and mass spectrometry can be coupled to a laser-sampling system working in this fluence regime.

As they do not offer direct interest for mass spectrometry studies, non destructive excitation regime and damage-only laser irradiation will not be considered along this chapter. We will focus more into the processes leading to material ejection from the solid, may it be desorption, laser ablation or ionization under ablation-threshold conditions. A general overview of the material removal channels after application of a laser pulse can be observed in Figure 1.1, adapted from Salvatore Siano.[17]

Out of these material removal channels, three main regimes may be described: desorption, normal boiling without plasma formation and

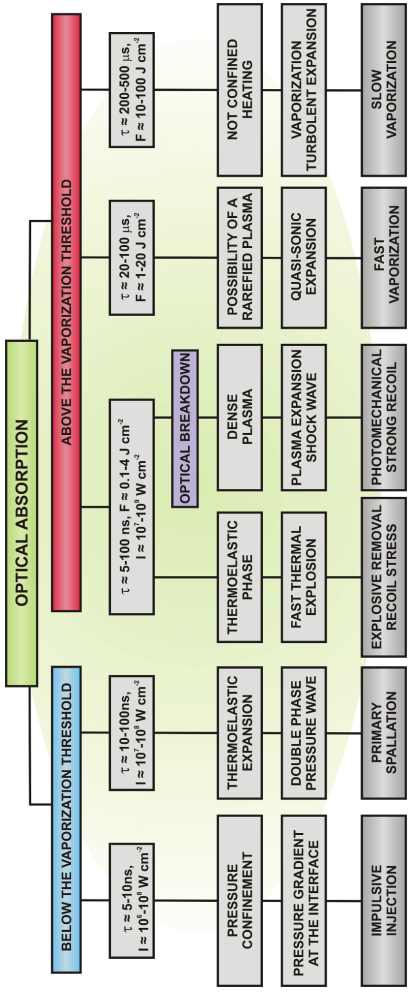

Figure 1.1: Different material removal channels that may appear depending on the laser parameters and material properties. Adapted from reference [17].

fast, explosive boiling with plasma formation. Both desorption and ablation have been widely studied. Desorption experimented a huge jump when the techniques for soft ionization were developed in the middle of the decade of 1980.[14] On the other hand, it is relatively easier to perform laser-ablation of solids and measure whatever we are interested of optic emission of the plasma [18] or ions.[3] To perform ablation all we need is to focused a laser with energy enough to surpass the ablation threshold.

Between these two working regimes, a normal-boiling sub-threshold ablation mode can be found. Despite desorption and ablation being very extended and studied, this energy regime, in which laser-ionization mass spectrometry (LIMS) in sub-ablation threshold conditions may be performed, seems to have been less studied.

1.3 Laser Desorption

Laser desorption of a solid is one of the more important analytical applications of lasers, including the characterization of organic compounds without biochemical activity but, more importantly, the analysis of biochemical metabolites and other biological species.

Despite the existence of many desorption techniques, if there is one that has been widely adopted in many research and routine laboratories around the world, it is matrix-assisted laser desorption/ionization (MALDI). Along with many soft-ionization techniques that bloomed in the decade of 1990, such as electro-spray ionization, the MALDI technique (developed in the decade of 1980) is one of the essential pilars that sustain modern advances in proteomics, metabolomics and many fields in current biochemistry.[19] The next section will depict MALDI as a representative approach of the laser-based analysis under desorption regime.

1.3.1 Matrix-assisted laser desorption/ionization

Matrix-assisted laser desorption/ionization (MALDI) was first depicted in the decade of 1980.[14, 20, 21] Until the development of MALDI and soft ionization techniques, analysis of organic compounds of relatively high mass by mass spectrometry was limited to the plasma desorption mass spectrometry (PDMS).[22, 23]

To work under these conditions, the amount of energy being deposited on the target is strongly limited. In fact, the desorption and ionization steps are assisted by the addition of a matrix, helping in the reduction of the energetic contribution of the laser.

However, due to the limited amount of energy being deposited to get assisted soft ionization, information obtained through this experimental approach is mostly limited to molecular information. Under some conditions, information in the fragmentation of complex organic molecules can be gathered, allowing tasks as hard as the sequenciation of proteins to be fulfilled.[24, 25] On the contrary, atomic analysis using MALDI is rarely used and it is usually helped by other techniques like LA-ICP-MS.[26]

MALDI: setup, advantages, drawbacks

Experimental setup for MALDI is rather similar to the one used for LIMS. Main differences arise in the preparation step, that usually requires wet manipulation of the samples. The sample preparation is critical in MALDI: from choosing the proper matrix to properly use the required concentration of matrix.[25] This makes MALDI lose one of the more important advantages of using a laser for sampling –the absence of sample manipulation– in order to gain the capability of analyze huge biomolecules.

The sample preparation in MALDI usually includes mixing a small amount of analyte with an absorbent compound (the matrix) that will assist the desorption and ionization of the sample. This mixture of ana-

lyte and matrix is dried at atmospheric pressure and the solid residue is introduced in the mass spectrometer for analysis. Common matrices are small organic compounds with H-donor capabilities (i.e. nicotinic acid), even though recent research has tried to use a variety of compounds (like carbon nanotubes or gold nanoparticles) as matrix.[27, 28]

In order to perform MALDI analysis, an absorbing compound is mixed with the analyte. This compound will interact with the laser beam and the resulting excitation will trigger some chemical interaction with the analyte. Hence, this added compound act as an absorbing matrix, easing the ionization of the analyte at lower irradiances.[29, 30]

On the other hand, MALDI still owns rapid analysis capabilities with the strength of acquiring a whole mass spectra for every laser event. Between the disadvantages of MALDI we can count the limitation of samples: metallic and, in general, inorganic targets are far beyond the applicability of the technique, and are better analyzed by LIMS or LA-ICP-MS.

Despite it helps to elucidate structures, there is another problem that only appears in reflectron-MALDI: the post-source fragmentation of the analyte, also noted as post-source decay in literature. As post-source decay we mean the fragmentation that an ionized molecule or fragment suffers after being extracted to the analyzer, during its drift along the flight tube.[31] In-source decay includes all the fragmentation occurring between the desorption/ionization step and the delayed extraction. This in-source formed fragments will have different velocities, as usual in TOF-MS, and each original fragment may be detected as a different peak in the mass spectrum.

In linear mode, post-source decay is not significant, as the ion has been already accelerated and the fragments, obeying the conservation of momentum, will have the same velocity and reach the detector at the same time. So, even fragmented, this post-source decay in linear mode is detectable if a superconducting ion detector is used,[32] but the analy-

sis performs without problems if using conventional microchannel plates. When the reflectron comes into play, new signals appear corresponding to the fragments formed during the flight (post-source decay), as they will be affected in a different way by the electric field applied in the reflectron region. Hence, they will receive a new impulse, transformed into different velocities (depending on their m/z ratios) and reaching the detector at different, non calibrated, times. This signals may be unwanted as this makes the spectrum look different. Even though this opens a new door to structural interpretation and further analysis.[33] If the new fragments are of low mass, their deleterious effect on the quality of the spectrum just adds to the typical interference in the low mass range (up to $1.5\ KDa$) due to massive signals from the matrix.

An undesired effect during the desorption/ionization steps is that analysis is hardly quantitative. Ion formation is not equally efficient for every single species, and enrichment of the desorbed material on ions coming from one or more analytes may occur. Even though modelization has tried to overcome this limitation,[34] it has not been completely solved. Despite this process is fundamentally different than fractionation of inorganic targets (see Section 2.1.3), the consequence is rather similar: the composition of the ionized material differs from the one of the sample.

1.4 Laser Ablation

Laser-ablation is one of the first applications of lasers, first described in 1962.[35] However experimental setup and devices have evolved dramatically in the last half century.

When a sample undergoes the action of a laser pulse with high energy enough, a plasma with high temperature and electronic density is formed, as a consequence of the energetic apport. Diagnostic of this plasma via atomic emission or ion detection is suitable for the determination of the

chemical species contained in the starting matrix to where the action of a laser pulse was applied. Despite sometimes plasma formation and collection of its optical emission are the ultimate goal of the laser-ablation, for many applications laser-ablation is merely used as a sampling method, as it occurs for LA-ICP-MS, where ablated plume is transported to an ICP torch were the whole sample is fully atomized and ionized before a detection system (OES or MS) acts.

As it happens to the desorption regime, laser-ablation applications with different approaches have been widely covered in recent years.[3, 36–39] There are many applications of laser ablation in modern spectroscopy. As this memory deals with laser-ionization mass spectrometry we will consider two main applications of laser ablation: laser-induced breakdown spectroscopy (LIBS) for its simplicity and versatility and LA-ICP-MS as it combines ablation with the ultra-high sensitivity of mass spectrometry.

1.4.1 Laser-induced Breakdown Spectroscopy

Despite the fact that LIBS is not a mass spectrometry technique, we will pay some attention to it for two reasons:

- Due to its simplicity and advantages, it is one of the more extended laser-based modern spectroscopic techniques.
- It uses laser-ablation as a localized sampling method and the wide use of LIBS was also a trigger for many studies concerning how the laser is absorbed by the solid in a way that ablation can occur.

Laser-induced breakdown spectroscopy is one of the most flexible techniques involving lasers for chemical analysis, capable of obtaining information from any kind of sample.[37] It is versatile and has been applied for a broad range of applications,[18] also for in-situ analysis.[40]

Mainly, LIBS measures atomic emission, even though emission corresponding to molecular fragments can also be detected. The laser is used to induce heating, boiling and excitation of the target.[36] When we focus a laser beam on a sample, we make it possible to form a plasma with high temperature and electronic density. This plasma, during its relaxation phase, will emit photons that can be collected and measured.

The technique was first used in the decade of 1960.[35] Since then, it has received large attention due to their capability to obtain the elemental fingerprint of any sample and, hence, deduce its composition.[41] In the decade of 1980, due to improvements on laser development, LIBS started to be applied to solve analytical problems.[42]

LIBS, basic setup

Typical instrumental design for LIBS is so open that it allows for analysis of many types of samples under different conditions.

A graphic description of the setup can be observed in Figure 1.2. The figure shows a high energy laser pulse impinging on a surface, with the subsequent plasma formation. As a variation to the basic setup, laser pulse may be guided to the sample by means of a fiber optic, adding the ability of perform remote analysis.[43] The optical emission of the plasma is collected and focused onto the entrance slit of an spectrograph. The spectrograph will proceed to the separation of the emitted radiation. In parallel, a pulse and delay generator synchronizes the output of the laser beam (acting as a trigger) with the detector (typically a charge-coupled device, sometimes intensified for better sensibility).

The simplicity of the setup, together with the improved stability of lasers and the decreasing prices of the devices has led the presence of LIBS in many analytical fields, but also in basic research.[44–46]

Despite it has many advantages, LIBS has also a few drawbacks when

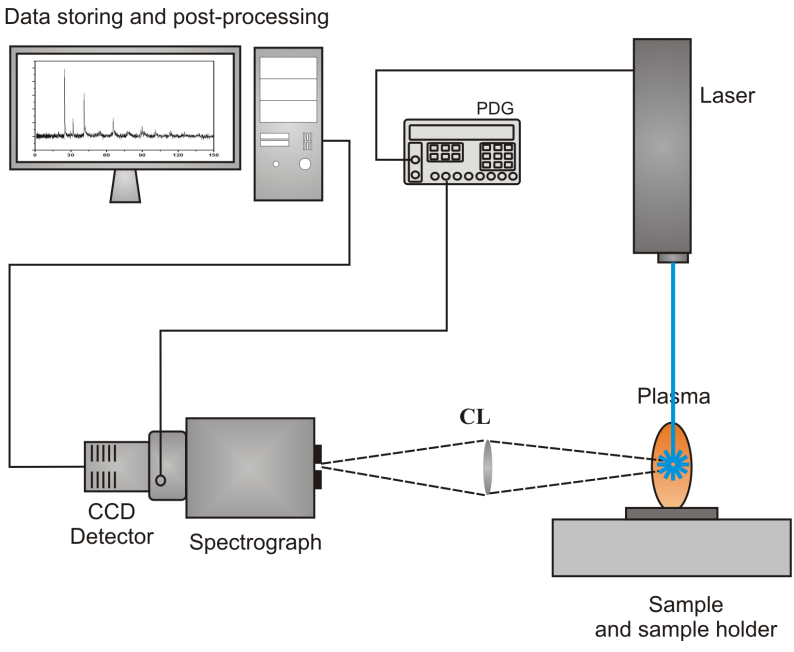

Figure 1.2: Basic setup for LIBS. Laser is focused over the surface of the target. A pulse and delay generator (PDG) controls and triggers the acquisition.

compared to another instrumental techniques that combine lasers with mass spectrometry. The first point would be sensitivity, mainly due to the improved performance of ion detectors.[47] The second disadvantage is the absence of isotopic information.

1.4.2 LA-ICP-MS

Laser-ablation inductively-coupled plasma mass spectrometry (LA-ICP-MS) is the most widely-used inorganic-analysis tool involving lasers. Though LA-ICP-MS have been used to perform speciation on organic and bioinorganic samples,[48, 49] its more important use has been the inorganic analysis of elements down to trace levels.[3, 50]

In LA-ICP-MS (Figure 1.3), a laser is focused on a target so that it is

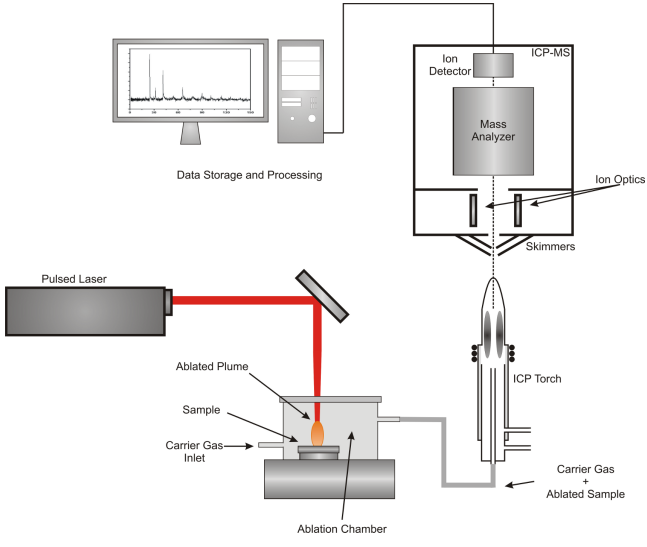

Figure 1.3: Basic setup for LA-ICP-MS. Laser is focused over the target's surface. The carrier gas transports the analytes to the ICP torch and the fully ionized mixture of gases enters the mass spectrometer.

capable of generating a plasma. Most of the time this target is a solid, inorganic sample. The sample is placed inside an ablation chamber, designed to allow easy access of the laser to the sample. The ablation chambers incorporate one side apertures to the carrier gas. The gas pushes the solid aerosol out of the chamber using a second lateral orifice on the opposite side. In the entrance of the ICP, the ablated particles transported by the carrier gas (typically, He or Ar gas) are mixed with a gas (more typically, Ar) that is being ionized in the ICP torch, forming a very high temperature plasma with a high ionization degree.

Perhaps the ICP torch is the more special device in a LA-ICP-MS instrument. In this torch, argon flowing inside the tube is ionized by a spark coming from a Tesla bobine. The tubular torch is partially surrounded by a induction bobine capable of producing a power of $2\ kW$ at a frequency

of $27\ MHz$, whose function is to heat up the gas flow. Due to this spark and heat apport, any sample carried by the gas gets atomized. The result is an almost fully-ionized flame with temperatures as high as $8000\ K$.[51]

The efficient transport of the ions from the high-pressure torch to the mass analyzer requires the use of a series of skimmers that induce supersonic expansion of the gas due to the different vacuum levels. By this method the sample is introduced into the mass spectrometer under high vacuum.

Ion analyzer in LA-ICP-MS is usually a quadrupole, as there is no need of a high-mass ion detector. Despite quadrupoles have been traditionally treated as limited detectors, in comparison with panoramic, full-spectrum analyzers like time-of-flight, modern quadrupoles work well if the sample we are going to monitor has a limited number of signals of interest. Under this conditions, even in-depth analysis, that usually requires the whole spectrum to be acquired with every single laser event, can be performed successfully.[52, 53]

Advantages of LA-ICP-MS include ultra-high sensitivity that allow for the analysis at ultra-trace levels.[50] The laser-formed plasma is the input for the ICP torch. The cloud of particles are transported to the ICP where they get reheated and ionized to the fullest extent. In this way, the laser plasma is used for sampling purposes, while the ICP is used for analysis, providing the advantage of more precise resultes due to its robustness.[47] As a consequence of the high ionization degree, almost 100% for every element, ICP-MS is one of the few mass spectrometry setups with quantitative capabilities, as the ICP torch (where temperatures of $8000 - 10000\ K$ may be found) has an extremely-high ionization efficiency and, thus, greatly minimizing the influence of the different ionization efficiency for many different species. When laser-ablation is used, the fractionation of the initial ablation will remain the bigger problem in quantitative analysis, and much work has been recently done to minimize

it.[54]

Despite the advantages, the lack of molecular information, the sample restrictions to fit the ablation chamber and the number of isobaric interferences due to the Ar presence, remain the major drawbacks of LA-ICP-MS.

1.4.3 High-fluence LIMS

Laser-ablation can be also used as sampling method for time-of-flight mass spectrometry. In this case, a fluence high enough to form a plasma is used to ionize a target. Despite these experiments are commonly noted as LIMS, regardless of the thermal regime taking place,[55, 56] they are sometimes noted in literature as Laser-ablation Mass Spectrometry (LAMS).[57]

Advantages of LA-TOF-MS against other ablation techniques like LIBS include the better sensitivity of mass spectrometry. As the laser parameters remain constant, the permanent damage on the target, as well as the almost total atomization of the sample and, thus, the restricted information on molecular species will be identical.

1.5 Sub-plasma formation Regime

The energetic regime above the desorption where negligible mass transfer occurs is probably the less studied from the three intervals we described previously.

The sub-plasma formation regime lies between the desorption (Section 1.3) and ablation (Section 1.4) regimes. In this intermediate conditions, ionization of the solid can be achieved by thermal heating of the solid when we focus a laser beam on its surface, while keeping the laser fluence below the plasma formation threshold.

For this regime, the amount of analytical work found in literature is substantially smaller, even though some authors have investigated it recently.[58] The instrumental description of the LI-TOF-MS technique may be found below (Section 1.6).

Despite this, LI-TOF-MS owns some important advantages against other similar techniques. While it uses laser radiation to perform sampling and a fast time-of-flight to separate the ions, the technique benefits of the laser capability for rapid and localized analysis.

If we compare LIMS against techniques in the desorption regime, LIMS is still able to give some molecular information while adding all the atomic information. Desorption is not able to give atomic information and other techniques requiring only the excitation of the target, as Raman spectroscopy, are also unable of providing any atomic information while having the additional problem of lower sensitivity.

As the energetic requirement for plasma formation is higher,[58] avoiding the plasma formation in LIMS reduces the amount of energy deposited on the sample and, thus, sample damage. Sample damage consequences may be evaluated from two different points of view: permanent damage done to the target and transformations underwent by the molecule under analysis. Even though, LIMS is still minimally destructive and sample introduction has some size restrictions, as the sample needs to be introduced into the vacuum region.

When the permanent damage, typically a crater, left by a laser pulse in any given solid is measured, a significant reduction of the sample damage under sub-plasma threshold conditions is found.[59] As reducing the fluence minimizes the thermal stress induced by the laser, molecular fragmentation as a consequence of low fluence laser irradiation may appear (see Chapter 6). This fact represent an advantage, when comparing with the limited features of the organic analysis in LA-ICP-MS or LIBS.[60,61] Additionally, as no carrier gas is needed, *Ar*-related interferences, that

limits the LA-ICP-MS and GD-MS analysis, are not present.

As a limitation, quantification in LIMS is hard to accomplish, as it is in many other MS techniques. This quantification is difficult not only as a consequence of fractionation,[62] but also as a consequence of the different ionization degree within the constituents of the plume. However, attempts to quantify this measurements, applied to geological samples, have been made.[57]

After comparison, LIMS emerge as a trade-off tool for rapid atomic and molecular analysis whose analytical capability is independent from the state of aggregation of the matter and even independent of the environment.[55] Moreover, it is independent of the electric and magnetic properties of the solids, making possible the analysis of conductive, semiconductive and dielectric solids. Multielemental and simultaneous analysis of major, minor and trace elements with a wide dynamic range of up to 10^9 in any kind of solid can be easily done.[50] These advantages, added to the non-existence of moving parts inside a TOF, explain the use of LIMS for extraterrestrial analysis in solar-battery powered instruments.[63]

1.6 Instrumentation on Laser-ionization time-of-flight Mass Spectrometry

In laser-ionization time-of-flight mass spectrometry, many instrumental sources combine to build a robust but complex technique.

Basic instrumentation to perform LI-TOF-MS (see block diagram in Figure 1.4) include a laser source, the optics needed to guide the laser beam to the target and the electrodes to deflect the ions to the ion analyzer. Also, an ion analyzer and a ion detector are also needed, as well as a read-out system to measure the ion current reaching the detector.

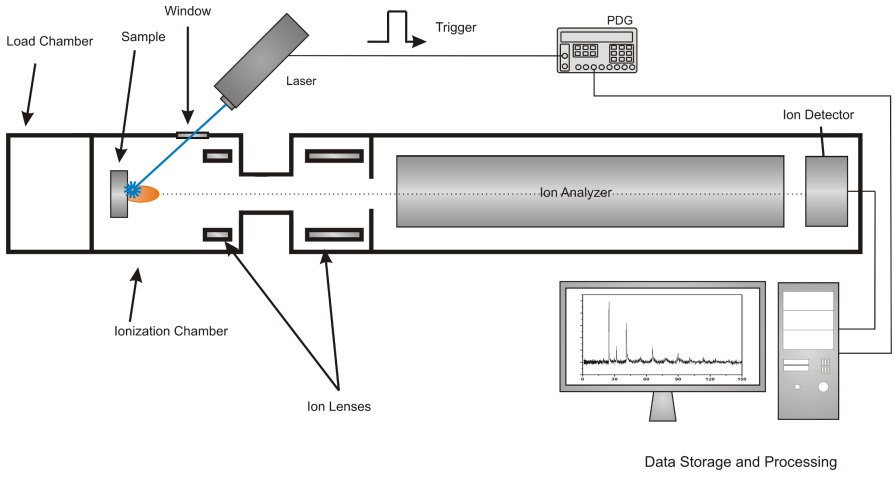

Figure 1.4: Basic setup for LIMS. Once the sample has been loaded into the vacuum stage, a laser is focused over the target's surface. Ions formed are extracted to the analyzer and detected. Both the laser pulse and the detector are synchronized by means of a digital pulse and delay generator.

Additionally, the whole instrument must be equipped with a pumping system to get high vacuum or ultra-high vacuum inside the chambers were ions are formed/transported.

1.6.1 Laser

The laser is used as a sampling method. When the laser is focused on the target, ions are formed that will be later analyzed and detected.

Many properties of the laser beam, including energy, stability, pulse width, wavelength, divergence and mode of operation of the laser do influence the way the solid interacts with the beam. Each laser type presents a series of advantages, and some drawbacks, as well.

Nowadays, the most used laser for LI-TOF-MS is the *Nd:YAG*, a solid state laser with a garnet of ytrium and aluminum doped with neodimium

as active medium. This laser is usually operated in combination with an electrooptic modulator or Q-switch, whose operation is based in the Pockels effect. The Pockels cell confines the laser within the optical cavity and gives origin to short pulses (duration in the range of $3 - 10\ ns$). Subsequently, the energy per pulse increases. This increasing of energy, as well as the pulse stability, can be controlled to some extent by modifying the parameters of operation of the Q-switch.

Nd:YAG lasers are robust and compact laser sources requiring low mantenience, an important factor that leaded to the great adoption of *Nd:YAG* lasers for laser-based mass spectrometry.

As a tendency in recent years, the growing adoption of solid-state mode-locked femtosecond lasers as *Ti:Sapphire* leaded the increasing use of this type of lasers for many laser-based spectroscopy techniques, including LIMS.

1.6.2 Optics and Laser Beam Guiding

Optic elements are needed to redirect the laser beam from the output in the laser head to the target. These elements are mirrors, prisms and lenses that simply change beam direction and focus it. But also include elements that modify several properties of the incoming beam. This second group of elements include polarizing crystals, beam splitters, half-wave and quarter-wave plats, telescopes, beam expanders, band filters and optical attenuators.

1.6.3 Ion Optics and Collection

Ion collection is a critical step for any mass spectrometry analysis. In LIMS, as the ions will be formed from the solid material after fast heating, they tend to exit with high kinetic energy and great spatial dispersion.

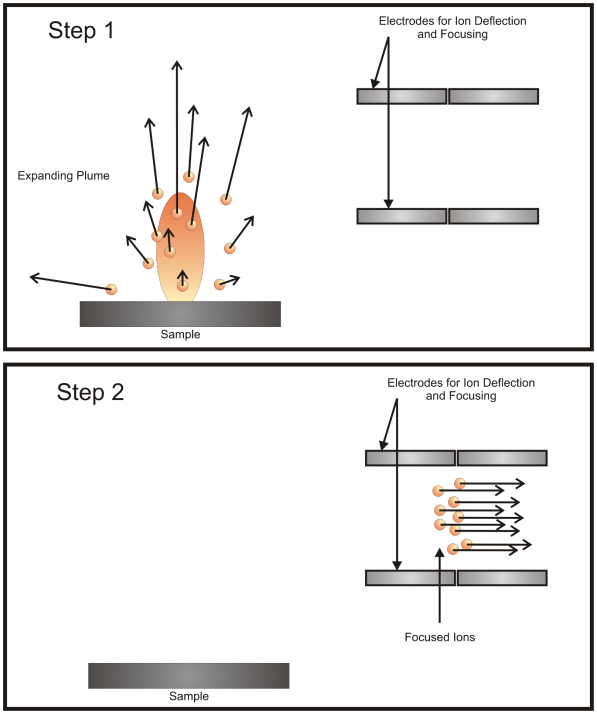

Figure 1.5: Dispersion minimization by ion optics. The figure simulates an orthogonal extraction in which arrows represent direction and velocity of the ions before and after the action of the deflection and collection by the ion optics.

To reduce this dispersion, a set of ion optics needs to be used for proper ion focusing before they enter the analyzer. Fig. 1.5 shows an schematic description of how the ion optics reduce dispersion on direction and velocity of ions in the expanding plume. First, the early formed ions will have some initial dispersion. By means of pulsed extraction, the resulting ion packet will be collimated and focused. After the ion optics, the analyzer will separate ions based on their m/z ratio.

1.6.4 Time-of-flight Analyzer

In 1919, Francis Aston (an advanced pupil of Thomson) designed the first velocity focusing mass spectrometer, a precursor of what would later be the time-of-flight analyzers. However, we have to step in time nearly three decades to get the first real time-of-flight concept, designed by William Stephens and presented in the American Physical Symposium in April 1946, as remembered in the APS website.[4] A few years after the first concept of the time-of-flight was presented by Stephens, Wiley and McLaren who improved the achieveable resolution of the instrument by adding a synchronized and delayed extraction system that made possible to make some corrections for the initial spatial and kinetic energy dispersion.[64] Wiley and McLaren were hired by the Bendix Corporation. This company is credited to have been the pioneers in developing and selling commercial time-of-flight instruments. The improvement brought to the technique by this delayed extraction were so important that their names were assigned in the literature to coin the new setup as the Wiley-McLaren configuration.

Nearly two decades later, in 1974, Boris Mamyrin presented the next major improvement for the time-of-flight mass spectrometry: the reflectron. The reflectron, also called "ion mirror", is a device including some electrodes that correct some of the kinetic energy dispersion of the ions, thus improving the resolution of the instrument.[65]

Figure 1.6 shows a linear and a reflectron time-of-flight. The linear TOF is able to separate ions with different mass-to-charge ratio, but is unable to correct the initial dispersion of the ions with identical similar mass-to-charge ratio. Using a reflectron makes it possible not only to perform a better separation of ions with different m/z ratio, but to compress the packet of ions with the same m/z ratio. The first aim is achieved as a result of the increased the total length run by the ions be-

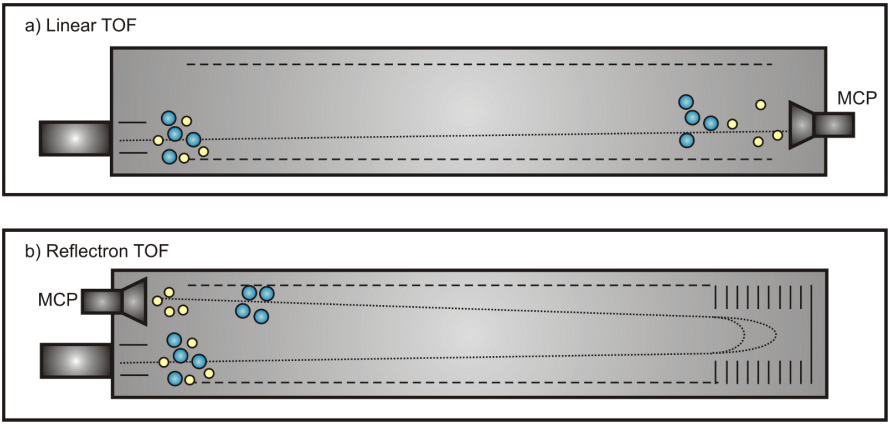

Figure 1.6: a) Linear TOF. Ions with different m/z get separated, but no dispersion among ions with similar m/z is corrected. b) Reflectron TOF. Ions with different m/z get separated and, additionaly, dispersion among ions with similar m/z is partially corrected.

fore reaching the detector. On the other hand, ions with identical m/z ratio and different initial kinetic energy will be forced to describe different trajectories inside the reflectron flight-tube, so that the ion packet (and the subsequent peak) will be narrower.

The combination of pulsed and delayed extraction with a reflectron turns a time-of-flight in one of the most powerful ion analyzers available for mass spectrometry. In this analyzer, all ions generated in the ion source and collected by the electric field of the ion optics fly through the analyzer (a field-free drift region) and reach the detector sequentially. However, all formed ions will reach the detector and this is a main difference with other analyzers such as quadrupoles.

Before ions enter the flight tube, they must be accelerated and focused using ion optics (electrodes). A critical point in the analysis is to apply a voltage high enough so that we can consider that every ion to be analyzed has the same kinetic energy (E_k). As we already know, kinetic energy of a

particle is proportional to its mass and also is proportional to its velocity (see Equation 1.1).

$$E_k = \frac{1}{2}mv^2 \tag{1.1}$$

If we assume all the ions to have the same kinetic energy and we substitute the m value for the m/z ratio, then its velocity will depend only on its mass-to-charge ratio.

$$\left(\frac{m}{z}\right) = \frac{2E_k}{v^2} \tag{1.2}$$

From the Equation 1.2, the time it takes an ion to reach the detector will vary for different m/z ratios. So, depending on this value, ions will reach the detector sequentially, sorted by their time-of-flight. A TOF analyzer is not simultaneous as the ions reach the detectors at different times. However, the time difference is so small that TOF are commonly referred as quasi-simultaneous or panoramic.

When compared to other well known sequential analyzer as quadrupoles, their panoramic operation mode view and its theoretically unlimited mass-to-charge working range represent clear advantages.

1.6.5 Ion Detection

Ion detection is one of the critical parts of any mass spectrometer.

As any other detector for modern spectroscopy, the ideal ion detector will be required to have some properties:

- Sensitivity.
- High linear dynamic range.
- Speed of operation.

Specially, time-of-flight anayzer commented above requires a very fast detector with times responses as lower as possible to get a good resolution on the signal from ions with slightly different mass-to-charge ratio. Microchannel Plates (MCP) are typically coupled at the end of a TOF. Linear range of MCP is impressively good and sensitivity and speed are notable. As a disadvantage, MCP detectors lack sensitivity for extremely high-mass ions that impinge the conductive surface of the plate with less speed.

Cryogenic detectors can also be used with TOF analyzers. Cryogenic detectors are a fairly new type of detectors for mass spectrometry. This kind of detector show many advantages against other mass spectrometry detectors. Specially, cryogenic detectors are suitable to be used after a time-of-flight analyzer, a role that has been long reserved to the MCP detectors, but these detectors do not lack the sensitivity the MCP lacks for huge ions.[66] In cases where TOF analyzers are used and ions are too heavy for the MCP detector to be sensible enough, cryogenic detectors operating at extremely low temperatures (near $0\ K$) are used.

Two main groups of cryogenic detectors have emerged since they were presented in the decade of 1990: superconductive tunnel junction,[66] and ion conversion detector.[67]

1.6.6 Vacuum Equipment

As for any instrumental technique dealing with charged particles, the existence of a collision-free environment placed under reduced pressure to the level of high-vacuum (aprox. $10^{-5}\ mbar$) or ultra-high vacuum (aprox. $10^{-8}\ mbar$) is essential.

Vacuum pumps are usually clasified considering the way they operate: Does a pump operate directly against atmospheric pressure or does it require to be connected to another pump in order to operate? Following

this criterium, primary, secondary and tertiary pumps may be found.

Primary pumps work directly reducing the pressure of a system and throwing the exhausted gas to the atmosphere. These pumps are called primary because they can operate autonomously without being connected to an additional pump. This pumps allow for reduced pressure down to $10^{-1} - 10^{-3}\ mbar$. This category includes rotary pumps (needing oil to operate) as the more extended type. Primary pumps operating with water are also available, even though the vacuum level achieveable with this pump is much lower.

Secondary pumps cannot discharge directly into the atmosphere, so a mechanical forepump (primary pump) is typically used to maintain an outlet reduced pressure. First type of secondary pump depicted was the diffusion pump. However, turbomolecular pumps are nowadays the most used secondary pumps. Even though diffusion pumps have no moving parts (unlike turbomolecular, that spins at speeds as high as $75,000\,rpm$), they are getting abandoned as a consequence of the backstream of oil to the system. In fact, turbomolecular pumps do not use any oil, and represent a clean alternative to work in ultra-high vacuum conditions around $10^{-10}\ mbar$.

Tertiary pumps require a second pump (also connected to a primary pump) in order to get proper operation. Sputter-ion pumps are the prototype of tertiary pumps. Advantages of sputter-ion pumps include the absence of any moving parts, as well as the no requirement for any oil. Following this properties, sputter-ion pumps represent a clean pumping system capable of achieving a vacuum as low as $10^{-12}\ mbar$ with the addition of a long life-expectation. As a drawback, sputter-ion pumps can't operate at pressures above $10^{-4}\ mbar$ and recommended pressure to take profit of the full life of the cathode is under $10^{-6}\ mbar$.[68] As a consequence, a secondary pump (typically a turbomolecular pump) is fitted to the discharge of the sputter-ion pumping.

1.7 Conclusions

In this chapter we provide a descriptive introduction to Laser-ionization Mass Spectrometry (LIMS), its field of study and its scientific context. A broader insight on the theoretical models available will be given in the next chapter, where recent literature on the topic will be treated.

It must be noticed that the LIMS technique has a much broader interest that the one we centered on in this introduction. A similar notice must be made for the scientific context and applications of LIMS. Nevertheless, this introduction tries to focus in the solid analysis by laser-assisted mass spectrometry, as the experimental part of this memory is mainly based on this type of studies on solid targets. This memory describes a collection of studies developed using laser-ionization mass spectrometry. From the analytical point of view, the goal was to investigate the feasibility of new approaches that may lead to an improvement of the analytical performance of known techniques.

The work described throughout this memory include ionization and ablation threshold calculations on metallic targets (both pure and alloy), as well as the investigation of the matrix effect and different wavelength on the ionization threshold for this kind of targets. Also, different energetic approaches have been studied, as the one represented for the decoupled upload of energy via two different laser pulses. Additional investigations on the energetic regime required for analysis of a different type of targets (organic compounds) will also be discused. Finally, a chapter is included that let us take a peek on some of the new challenges of mass spectrometry: solid analysis with lateral resolution in the nanometers range.

Most of this work tries to throw some light on the laser-matter interaction process, linking the result to current models as a way to understand properly the way the solid responds to the excitation produced by

the laser beam so that ions are generated.

Chapter 2

Fundamentals of the Laser-Matter Interaction

2.1 Introduction

The present chapter will provide a small overview of the current models for laser-matter interaction. The theoretical knowledge on the subject has a dramatic importance for any experimentalist on laser, even though the work described in the next chapters will be centered more on analytical implications of the results obtained in the laboratory.

Despite the many applications currently available for laser ablation, the exact mechanisms for mass removal from a solid using laser radiation remain unclear. Many efforts have been made in this area so that laser ablation is described based on a thermal mechanism, the mechanical effects and the particle formation mechanisms, all of them being understood. In fact, this is one of the problems faced by theoreticians: depending on which type of material (gas, liquid, solid), the laser characteristics (pulse length, irradiance) and the environment (vacuum, air, atmospheres of different gas), the role that different mechanisms play in the laser-matter interaction vary and, thus, the model to properly de-

scribe this interaction may also adapt to these changing conditions.

As a first step, the focus will be placed on the application of nanosecond laser pulses for the ablation of metals.

2.1.1 Overview of Different Modeling Approaches for LA

A theoretical approximation for the laser-matter interaction model has been taken by many researchers in recent years. As said above, these works reflect the complexity of the laser-matter interaction process so that a wide variety of models exist that properly described specific cases (for example, *for solids only* or *for metals only*).

A variety of models for laser ablation are published that adjust to many different regimes of wavelength (UV, Vis, IR), laser irradiance, pulse length (fs, ps, ns), target material (metals, organic solids, liquids, aerosols), gas environment (vacuum, ambient gas).[1–8] Most of these models describe the laser-solid interaction from a macroscopic point of view, attending to the thermal heat conduction equation.[2, 4, 5]

This thermal assumption is justified especially for metals and for pulsed lasers with pulse duration in the nanosecond range. Indeed, in metals, light is absorbed by interaction with electrons. A photon is absorbed by an electron, which is raised to a higher energy state, most probably passing to the conduction band. The excited electrons collide with lattice phonons, thereby transferring the absorbed energy to the lattice. Since the relaxation time for these electrons (around $10^{-13}\ s$)[9, 10] is much shorter than the duration of a nanosecond laser pulse, the optical energy transmitted from the beam to the solid turns into heat instantaneously. As a consequence of this sudden energy transfer from the beam, the solid experiences a great stress. Relaxation of the solid under this circumstances implies the generation of a shockwave that in the end results in target damage and/or material ejection. This process is

described in literature as photo-mechanical damage.[10] As mentioned above, the material removal using longer pulses (from nanosecond pulses to longer durations) will be controlled by the photo-thermal process involving melting, vaporization, boiling and phase explosion of the target.

So, for laser ablation with nanosecond pulses, the thermal equation is applicable. While applicable for nanosecond laser ablation, the equation cannot be used in the picosecond and sub-picosecond range, where a more complex approximation (considering two different temperatures in the solid) will be more accurate.[11]

2.1.2 Plume Expansion

Despite laser ablation applications are mainly performed at atmospheric pressure, due to the simplification of the experimental setup, most of the theoretical models describe the plume expansion in vacuum or against a low pressure gas. In fact, as the modelization of these expansions is less complex when interactions with the surrounding gas can be treated as negligible.

The overall influence of the gas when we study the laser generated plume expansion is the confinement of the plume,[12] as well as its slower expansion in comparison to that in vacuum. When we irradiate a sample placed into a high vacuum environment, the resulting plume will expand up to the range of few centimeters and the speed of the particles will be much higher than the speed of the same particles when they are generated at atmospheric pressure. In the latter case, material can also move backwards and redeposite on the surface due to the collision with the dense media.[13] To consider the transfer of momentum from the plume to the background gas, some terms need to be added to the vacuum expansion model to take into account the increasing scattering of the particles due to collisions (as a function of the pressure of the gas) while

the plume expands. Even though, existing models[14] account only for a background gas with a maximum pressure of $50\ Pa$, far from the atmospheric pressure regime. Different models consider higher pressure ($1\ atm$), but at laser irradiance values ($10^4 - 10^5\ W$) where no plasma formation occurs.[15]

Many of the more extended applications of lasers to the analysis of solids include the formation of a plume inside a high pressure ($1\ atm$) environment. This accounts for LA-ICP-MS, where plume is formed inside an ablation cell filled with a carrier gas (tipically He or Ar) and LIBS, as many of these experiments are also performed in air. It is clear that the gas in the chamber influences the measurements in these techniques, as a gas with higher ionization potential will form a less dense plasma and, therefore, plasma shielding will be reduced.[16] Even though, the incorporation of the gas influence on the plume expansion to the models remains a task, the plume temperature and hence the electron density are not too much different for expansion in vacuum or in 1 atm background gas.[17] The major difference is expected in the rate of change of physical properties, which will be much faster under reduced pressure conditions.[18]

2.1.3 Particle Formation

When a plume is formed by laser irradiation of a solid surface, it contains a mix of ions, atoms and particles. Particles may be directly formed during the laser excitation but they may be also formed as the plume expands and collisions resulting in condensation take place. Particles are important when it comes to laser based analysis, as they are supposed to be the main source of fractionation.[19]

The effect of the particle formation has consequences for many techniques. In ICP, the particle size influence the transport so that small

particles can be easily guided into the ICP torch, while this sample introduction gets more difficult as this size increases. In other laser techniques, such as LIBS, the amount and size of the particles will determine the extention of scattering and shielding.[20] Fractionation also depends on particle size, and smaller particles show a more stoichiometric composition.

Particle formation in the laser plume during expansion has been well described in different models.[15] The background gas plays an important role, as the cluster formation depends on the collision rate between atoms, previously-formed clusters and the background gas, being this rate a function of the density of atoms coming from both sample and sourrounding gas.

This collisionally-driven particle formation explains the condensation of particles in the nanometer range. The formation of bigger particles (micrometer range) is due to direct ejection from the solid as a direct consequence of the laser-matter interaction. A pathway based on collision is ruled out due to the excessive number of collisions required.

The process by which material is ejected in the form of clusters depends on the type of material and its mechanical properties, but it also depends on the laser properties. When a laser pulse is focused on a solid surface, the sudden deposit of energy induce stress on the solid that may result in particle ejection. This ejection is due to photothermal effects, but if the pulse duration is shorter than the time needed to reach thermal equilibrium, fracture of the surface and spallation of material can take place.[21] In the case of metals, most expected mechanism is liquid ejection, as this liquid is a consequence of the undergoing thermal process derived from laser excitation. This liquid can be ejected as a result of the melting movement, but also may be a consequence of the impact of the recoil pressure due to plume expansion. This last process is called liquid splashing and will be more present at higher pressures of the buffer

gas.[22]

In addition, when high irradiance or ultrashort pulses are used, ejection of large particles is possible due to phase explosion (explosive boiling of the target material beneath the surface layer). This phase explosion takes place after the laser pulse finishes and its presence may be diagnosed by an increase in the crater size above a given threshold.[23]

Elemental Fractionation

Elemental fractionation during laser ablation is the preferential ablation of particular elements in the sample. When preferential ablation of any element in a sample occurs, the plume will have a different composition than the target. Usually, preferential ablation is more important at low fluences[24, 25] and involves an enrichment of the plume in lighter elements. When fractionation occurs, the plume composition is not representative of the solid composition. When fractionation occurs, the plume is usually enrichted in lighter, easier-to-ablate components, as there may be preferential boiling of these lighter elements.[26] Reports of volatile elements enrichment in the plume can be found in literature for nanosecond[27] and femtosecond laser,[25] even though negative effects of fractionation on analytical performance can be sucessfully reduced.[28] Fractionation is more present when we use nanosecond pulses, as bigger and less stoichiometric particles are formed.[29] Also, greater particles are formed when liquid splashing occurs.[30]

The laser interaction with the solid is one of responsible factors for the fractionation. The total elemental fractionation will depend on the particle size generated in the excitation process. The smaller the particle size, the smaller the degree of fractionation.[31] So, achieving a proper control on the particle size is very important to limit fractionation.[32]

To reduce the particle size and, thus, to reduce the fractionation, the

use of femtosecond lasers is proposed,

2.2 Models

The complexity of the laser ablation process makes preferrable first to study independently the different aspects of the whole process, as the whole model may be seen as a complex puzzle built step by step using the information gathered for each single and essential process (Figure 2.1).

At higher fluences, normal boiling of the upper layers is not the main process linked to material removal. Instead, at these higher fluences, phase explosion occurs and accounts for the larger portion of ejected material.[33] Moreover, a laser irradiance threshold is found for the ablation rate and the plasma formation in the plume. While below this threshold the ejection of material is assigned to normal boiling, at fluences above the ablation threshold, ablation accounts for a great portion of ejected material.[34]

In the next sections, we will consider specially the laser interaction with solids at low or moderate pressure (up to $1\ atm$).

For these targets, we will consider separatedly the thermal process on the target (including heating, melting and boiling), the plume expansion, the plasma formation and, even, the absorption of the laser beam in the plasma plume. Finally, a rapid insight of the coupling of these models will be taken.

2.2.1 Target Heating, Melting and Boiling

When a laser impinges a solid surface, energy is transferred from the beam to the target so that its surface temperature rises. Eventually the solid will melt and, even, boil. The temperature profile in the solid can be estimated using the heat conduction equation (Eq. 2.1).

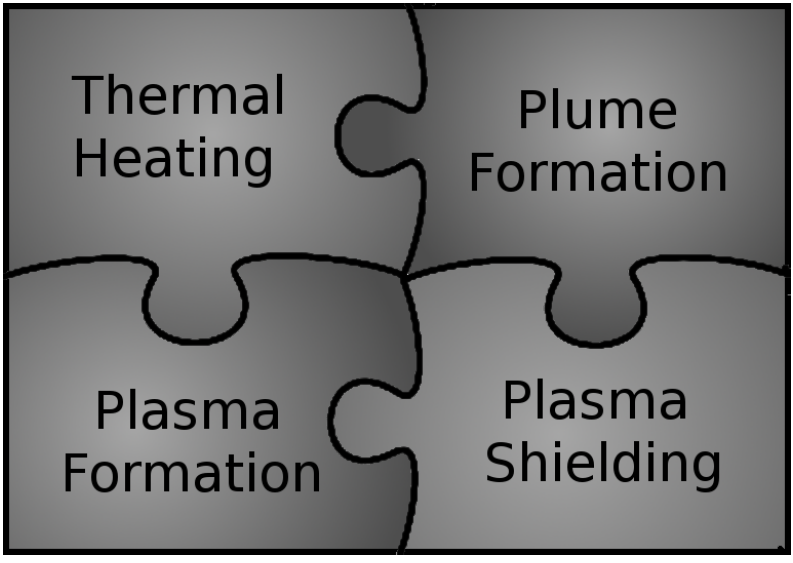

Figure 2.1: As no full model exist that explain each and every step of the laser-matter interaction that leads to a plume and plasma formation, the full process will be divided into small parts.

Considering that the optical penetration depth of the beam is, generally for metallic solids, much smaller than the beam diameter, the temperature equation can be simplified[35] from a four-dimensional case (x, y, z, t) to a two-dimensional (x, t) and has the form expressed in Ecuation 2.1, where T represents the temperature inside the target, x is the depth measured from the surface, t is the time, κ represent the thermal conductivity, C_p is the specific heat capacity, ρ the density and α is the coefficient absorption of the target material.

$$\frac{\delta T(x,t)}{\delta t} = \frac{\delta}{\delta x}\left[\left(\frac{\kappa}{C_p \rho}\right)\frac{\delta T(x,t)}{\delta x}\right] + \frac{\alpha}{C_p \rho} I(x,t) \tag{2.1}$$

The first term of the right side stands for the heat conduction, while the second expresses the contribution by laser absorption. $I(x,t)$ describes the laser irradiance as a function of time and position in the tar-

get. This laser irrandiance term can be rewritten:

$$I(x,t) = I_0(t)e^{-\alpha x}(1-\Re) \tag{2.2}$$

, where I_0 is the irradiance at the solid surface and $\Re$ is the surface reflectivity. Usual $\Re$ values for metals are approximately 1, but this reflectivity drops to levels as low as 0.1 during laser excitation at high enough irradiance ($10^8\ Wcm^{-2}$.[4] The decrease in the $\Re$ values is attributed to roughening due to heating, as well as to removal of material and melting of the surface.[36] Melting starts at the surface, but it extends into the material as the temperature continues to rise. For a typical nanosecond pulse, thermal affected zone in the target extends beyond the region directly irradiated by the beam.[37] Figure 2.2 shows the difference between the optically affected zone (region directly irradiated, delimited by the optical depth penetration of the beam into the target) and the heat affected zone (region affected by the heat tranfer from the beam and the optically affected zone).

As temperature rises, boiling of the target material gets relevant. The vapor pressure can be assessed by integrating the Clausius-Clapeyron Equation (Eq. 2.3).[38]

$$p_{vap}\left(T_s\right) = p_0 e^{\left[\frac{\Delta H_{lv}\left(T_s - T_b\right)}{RT_sT_b}\right]} \tag{2.3}$$

where T_s and T_b are the surface temperature and the normal boiling point at pressure $p_0 = 1atm$, ΔH_{lv} is the heat of vaporization, and R is the gas constant.

Despite the wide extension of the term "vaporization" to describe the phase change due to target heating after laser irradiation, some authors prefer to use "boiling", arguing that vaporization accounts only for the gas formed under normal conditions, and not the gas generated by irradiating the sample with a focused laser beam.[39]

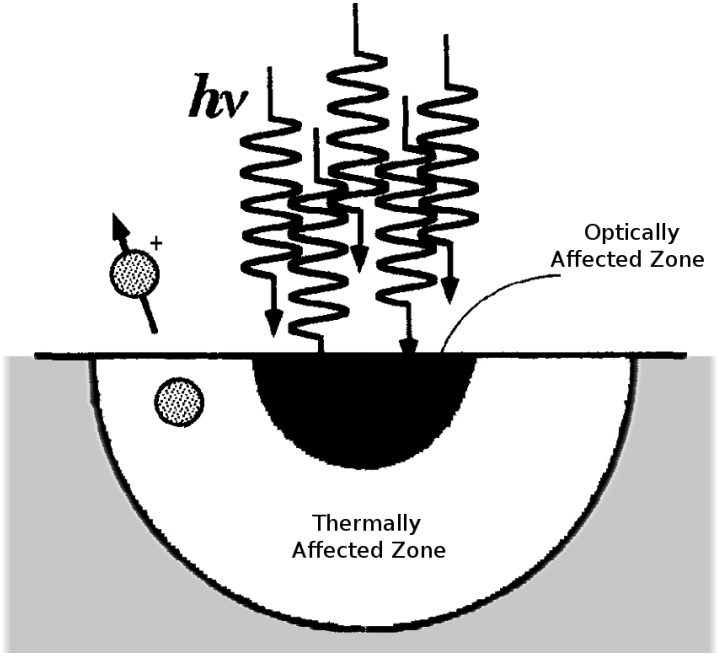

Figure 2.2: Schematic representation of the optically affected zone (limited by Optical Depth Penetration) and the heat affected zone. Relative sizes of these regions may vary depending on the laser pulse. Ions may come from both areas. Adapted from [37].

The model developed by Bogaerts et al.[4] considers the pressure low enough to use the ideal gas law and calculate the boiled gas density on the surface. Also, assuming that a one-dimension expansion takes place, the flow velocity of the gas is approximated by the average of the normal velocity component at temperature T_s.

When the effect of a 10-ns FWHM pulse with an irradiance of $10^9\ Wcm^{-2}$ is considered, the maximum temperature is predicted at the surface of the target. Temperature rises dramatically to reach a maximum within $10-20\ ns$ from the arriving of the laser pulse. After the pulse has finished,

target temperature begins to drop. Even though, it is not until $60\ ns$ that solidification occurs in the first $2\ \mu m$ of the surface.[4]

Boiling of the material can be also assessed. Closely following the reaching of the pulse to the surface, the rate at which atoms from the target leave the surface reaches a maximum when laser intensity at the target is at its maximum. After that, boiling speed decreases. If we consider boiling of the material due to heating as the only source for material removal, a lower-level for removing-rate per pulse under these conditions of energy and pulse duration can be marked at $70\ nm$. However, a $2\ \mu m$ thickness layer of molten material can be formed after pulse arrival. If we consider that all the molten is ejected due to liquid splashing before resolidification, that $2\ \mu m$ layer may be considered as an upper-level ablation rate. In literature, some authors report liquid splashing due to recoil of the plume as a responsible of a large percentage of the material removed and so, it should not be neglected.[40] Other authors point out the dominant role of liquid splashing only in some cases.[41] Interestingly, resolidification of the molten material has been proposed as a source for fractionation.[42]

Influence of the state of aggregation on the material ejection step

Many studies on material ejection using lasers have been carried out on condensed targets (both solid[33] and liquid[43]). Even though, a full model that succesfully describes the influence of the state of aggregation of the target on the ablation process has not been yet developed.[7]

In the absence of phase explosion, ejection is generally said to occur due to an electronically mediated processes, due to the repulsion between fragments during photolysis or to the repulsion between the electronically excited molecules and their neighboring molecules.[44–46] The photodesorption yield increases linearly with laser fluence,[7] evidenc-

ing its key role. Molecular dynamics simulations of heat transfer has provided additional understanding of the ejection process.[47]

In addition to the considered optical phenomenon, mechanical ejection of material may be considered. This mechanical ejection of whole molecules at a temperature lower than expected was in the base of the success for the analysis of molecular solids with nanosecond laser pulses.[7]

Different process may play a role during the ejection step. Laser arrival to the target change the temperature on the surface steeply. This fast change in temperature implies also a volume change that induces the generation of high-amplitude pressure waves, which can result in material ejection via mechanical rupture (spallation). Other processes may play a significant role, if targets with different properties are considered. For example, under UV excitation, most organic molecules photodissociate, while it is a minor process if metals are irradiated. Even though, these different processes will have a different importance depending on the target, the whole ejection process is determined by the sum of all these steps, that may take place in parallel.

Efforts have also been made to understand and explain the mechanisms for ion formation,[5,37,48] but, despite the work done to explain the influence of a laser pulse on inorganic compounds, these mechanisms still remain to be fully understood and modelized.

Despite the advances made, as a consequence of the enormous computing power required to simulate the laser-matter interaction processes, many simplifications are required to be able to get a representation of the target and irradiation conditions. Given this situation, it is not difficult to understand that many uncertainties remain concerning the role of the phase/state of the target during the irradiation and ejection of material.

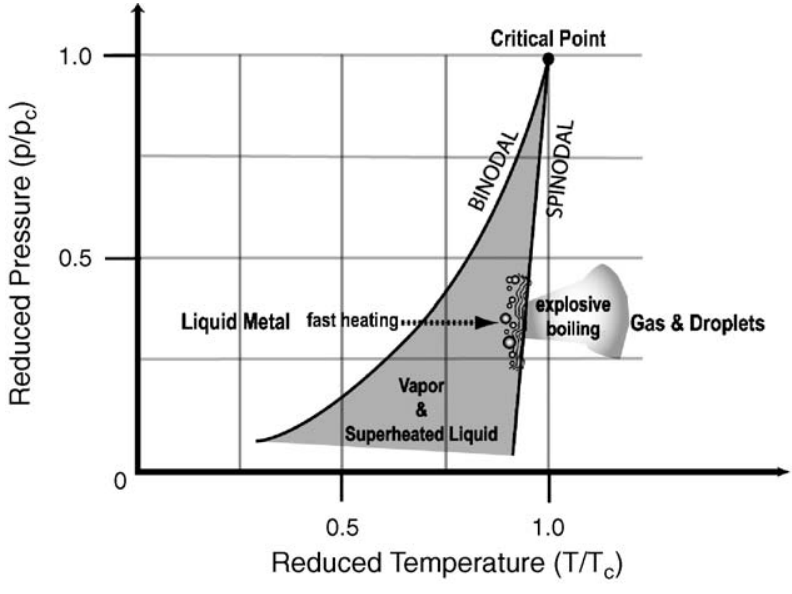

Figure 2.3: Phase explosion is linked to the apparition of a metastable overheated liquid that subtlely evolves to an unstable state via spinodal breakdown. When this happens, massive ejection of gas and liquid droplets occur. Taken from [30].

Phase Explosion

Laser ablation, strictly speaking, is any process of laser-induced material ejection. However, and even though the just made definition is strongly general, laser ablation is only said to occur when macroscopic changes are effected on condensed phases upon irradiation with intense laser pulses.[49]

Phase explosion is the explosive boiling of a superheated target material, occurring close to the critical temperature. Figure 2.3 shows the temperature-pressure (in terms of the reduced magnitude) diagram for an arbitrary molten metal. For this figure, the binodal line is the thermodynamic equilibrium boundary that separates coexisting liquid and vapor phase for a given combination of p and T. Laser pulses with dura-

tion shorter than $1\ \mu s$ can easily tresspass this binodal line, as the heat is delivered in a short time scale. Under this conditions, a superheated, metastable, melt is obtained. The limit for metastability is the spinodal line, where the liquid collapses into an unstable system. Then, massive ejection of gas and liquid droplets occurs.

The question concerning the identification of the ablation process by means of specific physical characteristics, and if it may allow its distinction from other processes occuring at lower fluences, has been treated in literature. For several applications, the only important parameter is the amount of material removed, at a expense of many other physical parameters.[7]

The degree of overheating necessary for material ejection is found to be lower than that suggested by conventional thermodynamic considerations,[50] indicating that the process is under kinetic rather than thermodynamic constraints. Therefore, material is removed by means of a non-equilibrum process taking place in the target, the so-called phase explosion.

To consider this phase explosion, an extra criterion to compare the rate of normal thermal desorption with ablation needs to be introduced. This may be achieved by comparing the rate of homogeneus bubble formation with evaporative rates or with the rate of energy consumed for bubble formation in the presence of nuclei promoting heterogeneus nucleation.[7] As a consequence of these comparisons, a fluence threshold is found. Below the threshold, the material removal rate follows the trend of bubble formation and normal boiling of the material. Above this threshold, the material removal rate increases dramatically and the homogeneus bubble formation does not describe the situation of the metal.

As mentioned above, the material removing process is complex, with many simplifications made. These approximations allow us to have models that provide a good explanation for the process, at a expense of many

uncertainties that still remain.

2.2.2 Plume Expansion and Plasma Formation

When considering the laser-matter interaction, we can assume the *adiabatic limiting case*. Acording to this regime, laser absorption by the target and the subsequent heating, boiling and plasma formation take place simultaneously and therefore, before the plume expansion. According to this limiting case, the laser ablation process can be divided in two different steps: a first step including boiling of the solid target and plasma formation and a second step in which plume expands. This simplistic approximation is not accurate as target heating, boiling and plume formation take place almost simultaneously[51] and the expanding cloud will interact with the laser light (reheating of the plume, plasma shielding). However, it allows the generation of models that explain many of the processes taking place without the non-linear phenomena of difficult mathematical treatment.

The expansion of the ejected plume can be treated according to the hydrodinamic model, with conservation of mass density, momentum and energy. Propagation of the plume will have a dominant direction normal to the surface and, at least for the first $300\ ns$ following the laser pulse, adiabatic expansion takes place and the expanding plume behaves as an ideal gas.[18] The Euler equations for hydrodinamics can be used to describe the expansion.[52]

$$\frac{\delta \rho}{\delta t} = -\frac{\rho\,(\rho v}{\delta x} \tag{2.4}$$

$$\frac{\delta\,(\rho v)}{\delta t} = -\frac{\delta}{\delta x}\left[p + \rho v^2\right] \tag{2.5}$$

$$\frac{\delta}{\delta t}\left[\rho\left(E+\frac{v^2}{2}\right)\right]=-\frac{\delta}{\delta x}\left[\rho v\left(E+\frac{p}{\rho}+\frac{v^2}{2}\right)\right]+\alpha_{IB}I_{laser}-\epsilon_{rad}$$

(2.6)

In these three equations, I_{laser} is the laser irradiance and α_{IB} is the absorption coefficient due to inverse Bremsstrahlung. Product of both terms represents the gain for the internal energy of the formed gas due to absorption of the laser radiation. ϵ_{rad} stands for the amount of energy emitted by the vapor (per unit volume and time) in the Bremsstrahlung process. These two terms are non-linear, as they depend on electron and ion densities (and, thus, depends on the gas density itself). This gas density can be very different along the plume, ranging from near-solid density to vacuum-like. In general, it drops with time as temperature does, as a consequence of the plume expansion.[53]

Despite the fact that hydrodinamic approach is valid, it has been reported on Cu[54] and Al[55] that the distribution of kinetic energies for the ions in the expanding plume can be shifted to higher values than the ones predicted if we consider only thermal energy transfer from the laser beam. This is assumed to occur due to the appearance of Coulomb repulsions between the ions forming the plume. These Coulomb repulsions, along with multiple particle collision, are responsible for the increased kinetic energy measured.[54] At high fluence, when material removal increases, collisions in the plume are more frequent. Under these conditions, the initial assumption of a positive expanding-only particle movement following a Maxwell-Boltzmann distributions needs to be modified to take into account the whole range of posible translations, even those ones redirecting the ions to the target's surface. This crucial stage

where these collisions occur is named Knudsen layer. Beyond the Knudsen layer, the plume expands.[56]

Density drops gradually as a function of distance in the plume, and very rapidly at the plume front. As time evolves, the plume becomes longer. If expansion against vacuum is considered, plume length is estimated to be around $0.1\ mm$ after $20\ ns$ and $2\ mm$ after $100\ ns$. For expansion in a background gas at $1\ atm$, plume expansion will be much smaller.[4] Shadowgraphy studies have probed this temporal schemes for plume formation and expansion.[57] This significant variation is supposed to be in the origin of the shock-wave generating process.[4] Temperature distribution in the plume is also a function of time. Temperature in the plume reaches a maximum at $20\ ns$, as the tail of the laser pulse gets to heat the ejected material. When the laser pulse ends, cooling due to plume expansion occurs.

The process leading to the plume formation usually takes place at high temperature. When this temperature is high enough, the gas gets partially ionized and, therefore, a plasma is formed. In general, the plasma will be considered in local thermal equilibrium (LTE), given the high number of collisions that may take place. In addition, the grade of ionization in the plume can be calculated using the Saha–Eggert equation (Equation 2.7).[58] The resulting non-linear system of equations applies to every position in the plume but for the nearest to the surface, the main source of ions near the target surface is not the collisions between particles, but thermoionic emission from the solid.

$$\frac{n_{i+1}n_e}{n_i} = \frac{2}{\Lambda^3}\frac{g_{i+1}}{g_i}\exp\left[-\frac{(\epsilon_{i+1}-\epsilon_i)}{k_BT}\right] \tag{2.7}$$

In Eq. 2.7, n_i is the density of atoms in the *i*-th state of ionization; g_i is the degree of degeneracy of states for the *i*-ions; ϵ_i is the energy required to remove *i* electrons from a neutral atom, creating an *i*-level

ion; n_e is the electron density; Λ is the thermal de Broglie wavelength of an electron; m_e is the electron mass; T is the temperature of the gas; k_B is the Boltzmann constant; and h is the Planck's constant.

Effect of the surrounding gas

The plume expansion is influenced by the presence (or absence) of a surrounding gas. As mentioned above, under reduced pressure conditions, plume length will be much greater. Apart from this effect due to gas pressure, there may be some influence due to the exact composition of the atmosphere surrounding the sample.

Although background gases with a lower ionization potential exhibit a higher ionization degree in the plasma, this effect is of minor importance compared with the ionization of the vapour plume. Subsequently, the model predicts that the background gas has no significant influence on the plume temperature and electron density in the early steps of ablation and plume expansion (first $100\ ns$). Nevertheless, the effect of the gas is large enough to yield some differences in the target ablation depths, which are calculated to be slightly deeper for He than for Ne, Ar and Kr.[59]

Laser Absorption in the Plasma

The formation of a plasma in front of the target surface leads to partial absorption of the beam in the plume. This process is known as plasma shielding and its importance grows when optical density of the plasma increases.[60] Even though plasma shielding may be seen as a drawback for the laser-matter interaction process, it is actually an advantage for many applications as it helps to excite the plasma to a higher level.

As laser absorption in the plasma mainly takes place in the vapour plume, and in total agreement with the slight influence of the surrounding gas on the plume temperature and electron density, plasma shielding

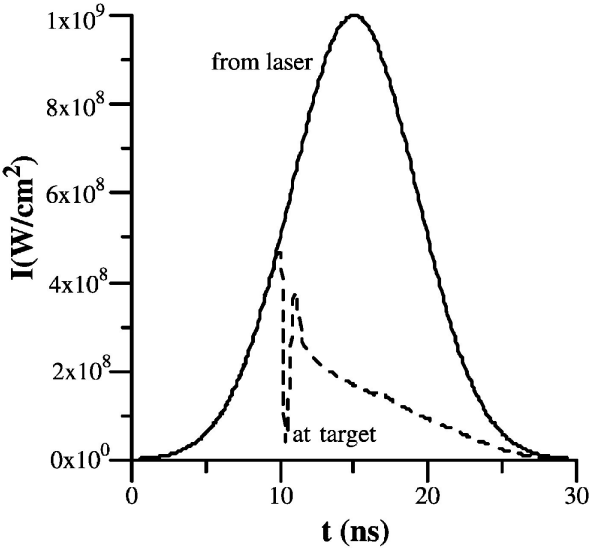

Figure 2.4: Laser intensity-time profile assumed in the model by Bogaerts et al. It is a Gaussian-shaped pulse with $10\ ns$ full-width at half-maximum (FWHM), and maximum irradiance of $10^9\ Wcm^{-2}$. The dashed line represents the calculated laser intensity arriving at the target, after passing through the plume (plasma). Taken from [4].

is only slightly affected by the background gas.[59] The first source of plasma shielding is the inverse Bremsstrahlung (IB). This phenomenom involves the absorption of the beam by free electrons that, as a consequence, raise to a higher level. Under these circumstances, the photoionization process is considered irrelevant, as the amount of atoms being ionized and leaving the discipline of the solid on its own is really small. An exception to this assumption is found for energetic photons and easily ionized gas, as photoionization in this case is not so hamperred.[58]

Figure 2.4 shows the theoretically-predicted energy reaching a target's surface when a Gaussian-shaped laser pulse with $10\ ns$ of FWHM is focused onto a surface with and without considering the effect of the

plasma shielding. It can be seen how, as a result of the plasma shielding, intensity reaching the surface decreases sharply. The decreasing of energy reaching the sample ends up in a less intense plasma. Along with this weaker plasma, expansion of the plume decreases its density, reducing its opacity to the laser pulse[54] and, thus, producing a weaker plasma shielding so that energy passing through the plasma and reaching the target starts rising again.

Plasma shielding is not constant and, therefore, its influence on the energy reaching the target can not be taken into account just by considering a constant attenuation. From the same studies performed by Bogaerts et al., it seems that plasma shielding starts to appear at laser intensities above $2x10^8\ Wcm^{-2}$. The larger the intensity above this value, the more important the plasma shielding becomes. In the limit, increasing the laser energy will not result in more laser energy reaching the sample. The main effect will be on target heating and plume formation, up to a certain value.[6]

2.2.3 Relation between the Different parts of the Model

The processes described in the upper sections strongly link the different physical changes taking place as a consequence of the laser beam reaching the sample. When the beam impinges the surface, a fraction of the target can boil. The formed gas will have a density, temperature and velocity whose values will be used to describe the plume expansion and plasma formation. Moreover, the plume itself will have effects on the target (splashing) and the formed plasma will lead to the apparition of some plasma shielding, reducing the amount of laser radiation reaching the surface and the efficiency of the irradiation process.

2.3 Effect of Target Reflectivity

The target surface reflectivity ($\Re$) included in the equation used is not known in detail. As a general value, it is approximately 1 for metals, but during the irradiation process this value drops to levels as low as 0.1.[4] Properly choosing the value for $\Re$ is of great importance in order to get accurate information about how much of the laser radiation will be absorbed by the target. Bogaerts et al. estimate this value in 0.34 for its model calculations. Figure 2.5 investigates the influence of $\Re$ in the laser-absorption model and have been taken from these authors and considers $\Re = 0.34$.[4]

When the target surface reflectivity increases, less energy can be properly coupled to the target and be transferred to it, leading to a lower temperature in the target (Fig. 2.5a), less melting (Fig. 2.5b), less evaporation (Fig. 2.5c,d), and consequently a lower gas density (Fig. 2.5e), a shorter plume (Fig. 2.5f), a lower plume velocity and temperature (Fig. 2.5g), and a less ionized plasma (Fig. 2.5h). As $\Re$ decreases, the energy entering the target increases, thus temperature, boiling rate, plume length, velocity and temperature and ionization grade in the plasma increases. However, this effect is more pronounced when $\Re$ changes from 1.0 (ideal behaviour, no laser energy is absorbed) to 0.9 than it is when $\Re$ drops from 0.1 to 0.0. This is explainable if we consider the relative increase of the energy getting to the target as reflectivity changes.

2.4 Effect of Laser parameters

Among the laser parameters influencing the interaction with the solids, there are three that play an important role: laser intensity (normalized to area in the form of irradiance or fluence), pulse duration and radiation wavelength.

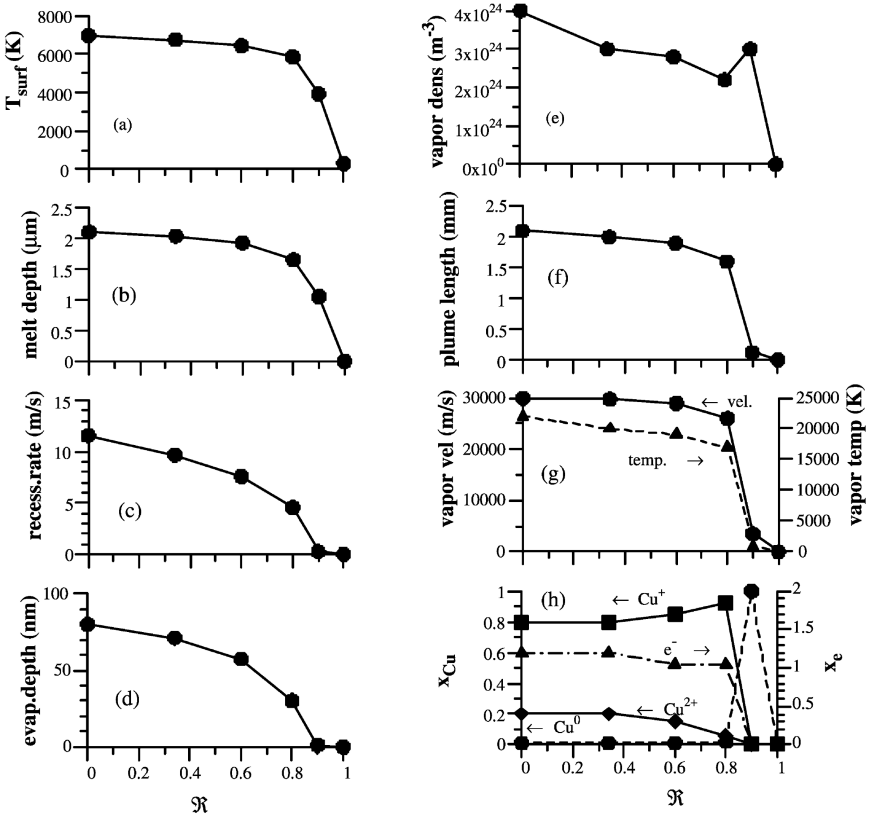

Figure 2.5: Calculated target surface temperature (a), melt depth (b), surface recession rate due to evaporation (c), evaporation depth (d), average vapor density in the plume (e), plume length (f), vapor velocity and average temperature in the plume (g), and typical fraction of Cu^0 atoms, Cu^+ and Cu^{2+} ions and electrons in the plume (h), assuming different values of the target reflectivity, $\Re$. Taken from [4].

2.4.1 Irradiance

Laser irradiance is one of the most important parameters modifying the response of the target. Typical fluences for laser ablation range from 10^8 to $10^{10}\ Wcm^{-2}$. Below these values, neither boiling nor melting is taking place.[17] Above this irradiance level, different processes, like phase explosion, may become important.

In the model by Chen and Bogaerts,[17] increasing the laser irradiance will increase the target heating, melting and boiling. Also, plume expansion velocity and temperature, ionization degree and both ion and electron densities in the plume will increase. As a consequence of all these increasing parameters, plasma shielding in the plume will also get more important. Thresholds for melting, boiling and plasma formation are theoretically predicted to be sequentially higher. This prediction for thermal boiling to plasma transition threshold was experimentally probed for a frequency-doubled Nd:YAG laser pulse.[61]

2.4.2 Pulse Duration

As a general trend, the melting and the boiling depth per pulse increase for longer pulses, as the target is exposed to the laser pulse for a longer period and plasma shielding is less pronounced due to the decrease in irradiance. However, higher ablation rate is found for shorter pulses.[62]

Anyway, for the pulse duration effect two trends may be observed depending on whether constant irradiance or constant fluence are considered. If we consider constant irradiance, longer pulses induce more heating and boiling of the target, as more fluence is needed to equal the irradiance of shorter pulses.[62] For constant fluence, shorter pulses have more irradiance and so target heating and ablation rate increases for shorter pulses.[17]

Looking at the mechanisms of material removal, it has been argued

that nanosecond laser pulses lead to slower heating under electron-phonon equilibrium and, as a consequence of the melting, greater damage for the surrounding area (photo-thermal damage).[63] In comparison, when picosecond or femtosecond pulses are considered, laser pulses generate a non equilibrium situation between electron and phonons, which is supposed to be responsible for material ejection (photo-mechanical damage).[10]

Concerning the heat affected zone, shorter pulses (especially, subpicosecond laser pulses) reduce the damage done to the target and help to confine the laser energy in the zone that has been directly irradiated.[64] Schematically, the effect of pulses with different duration in a given target can be seen in Figure 2.6.

Concerning the plume, for nanosecond pulses, the laser beam absorption, its scattering, and its reflection in plasma are said to be the limiting factors for efficient laser ablation.[65] After a certain time, the plume characteristics are identical, regardless the type of laser pulse. This is taken as a confirmation that the fluence (and not pulse duration) determines the plume behaviour.[17]

2.4.3 Wavelength

The wavelength of the laser beam will also influence the interaction with the target. In some theoretical calculations, it was found that laser irradiance threshold for target melting, boiling and plasma formation at $1064\ nm$ was considerably higher than at $532\ nm$ and $266\ nm$, while at $532\ nm$ it was found to be slightly higher than at $266\ nm$.[17] Therefore, shorter wavelengths yield more efficient ablation, which agrees with available literature and correlates well with experimental evidence.[66] However, this difference seems to be less pronounced when comparing wavelengths in the UV range.[67]

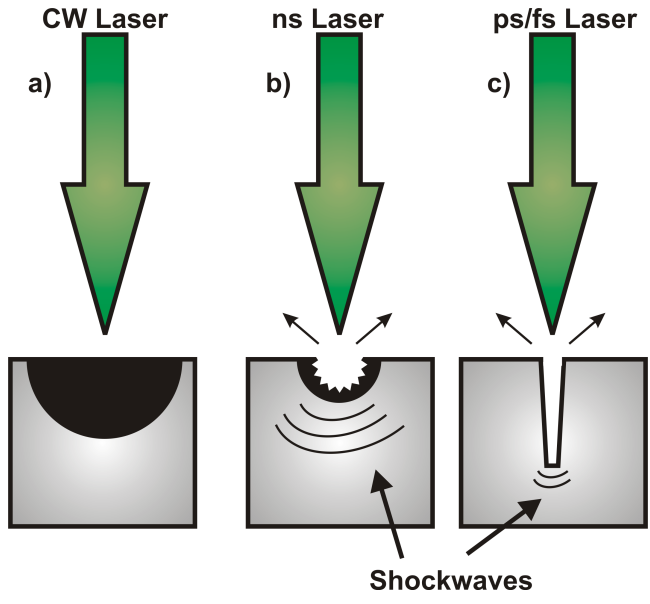

Figure 2.6: Schematic representation of the effects on the target due to different pulse duration. a) CW lasers produce the largest affected zone, with no phase explosion but greater thermal effects. b) ns-pulses reduce the heat affected zone and give rise to some explosive boiling effects. c) ps/fs pulses confine the thermal energy to the irradiated volume, have a bigger drilling power (higher irradiance) but leave craters with smaller diameter.

2.5 Conclusions

This chapter has summarized some of the most important advances in the explanation of the laser-matter interaction process by means of theoretical approximations. Existing models have been compared with experimental data when possible and a description for ablation of metals in pressures ranging from vacuum to $1\ atm$ has been given, taking into account different conditions in laser irradiance, pulse duration (ns to fs range) and laser wavelength.

Despite efforts made in theoretical studies, all encouraged to achieve

a fine understanding of the laser-matter interaction dinamics, the comprehension of the laser-matter interaction as a whole process remains unfinished and the exact influence of many parameters remain unclear.

However, in recent years many groups are developing an important work in the field of computer simulations, which may assist and improve the comprehension and the development of the models. Also, the efforts of experimentalists and many other people involved in technical engineering and fluid dynamics may converge in a better understanding of the laser-matter process.

Chapter 3

Experimental

3.1 Introduction

In this chapter we are going to get a deeper view of the experimental setup used in this memory. We will pay attention to the main setup and to the minor changes accomplished during the work.

The fact that this instrument is not a commercial one made it easy to design, modify and adapt every piece to fit specific needs. Evolution in the work scheme leaded us to change and improve different aspects from the improvement of the sample handling using a 3D manipulator to the design of a new acquisition software.

The basic experimental setup employed throughout this memory was modified sequentially, corresponding to four different configurations (as indicated in Figure 3.2), being Configuration N4 the one that will be detailed in Figure 3.2

The different system configurations will be treated separatedly, but the description of all the common settings and devices (such as the flight tube or the ionization chamber) will be merged into its own section. Figure 3.1 will help the reader to understand which equipment has been used in every single experiment, as in the next experimental chapters we

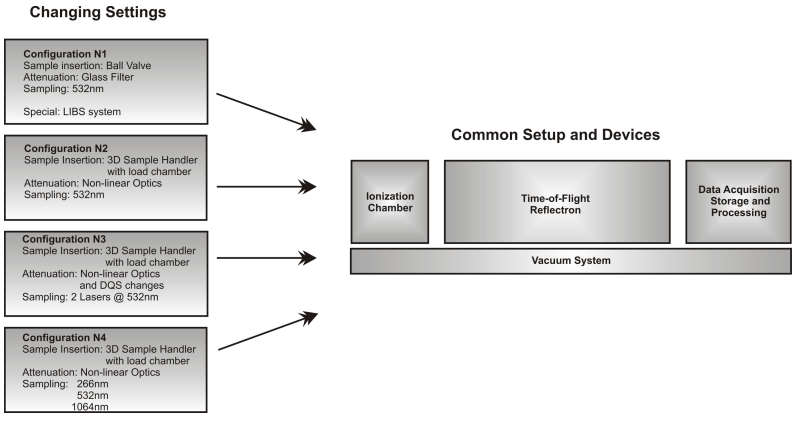

Figure 3.1: Schematic representation of the different representations. Common devices and settings for every setup are shown in the centered square. Specific elements are included in the numbered circles.

will refer the different setups as they are numbered here and detailed in the next sections of this chapter.

3.2 Common settings

In short, the Laser-ionization time-of-flight mass spectrometer (LI-TOF-MS) described below uses a pulsed laser as a sampling method. This laser is focused on the surface of a solid sample placed into the ionization chamber (evacuated to an ultra high vacuum level). As a consequence of the laser-matter interaction process the solid gets warm, eventually melts, boils and gets ionized. The ions formed will be transferred to the flight tube by means of a set of electrodes devoted to extract, accelerate and focus the ions. The flight tube is located in a field-free region so that ions can be analyzed and separated by their different mass-to-charge (m/z) ratio. In this case, ions with higher speed (lower m/z ratio) will reach first the detector.

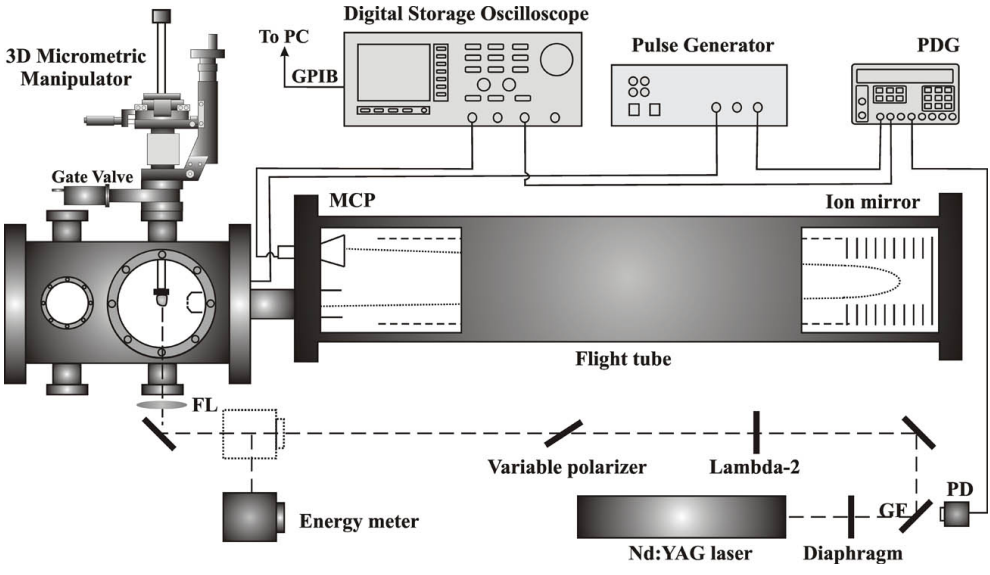

Figure 3.2: General setup used in most of the experiments in this Memory. CL: Collection lens; MCP: Microchannel plate; PD: Photodiode; FL: Focusing lens; GF: Glass filter; ICCD: Intensified Charge Coupled Device; PDG: Pulse/Delay Generator.

The arrival of the ions in the microchannel plate (MCP) produces the signal gaining as a consequence of a series of collisions. Electrons generated in the detector are finally collected in the final anode and transferred to a digital oscilloscope. This oscilloscope has the ability of plotting and storing the mass spectrum, or transfering the data to a computer through a general purpose internet bus (GPIB) interface. Usually, post processing of the stored spectra included the use of MATLAB^{TM} routines, as well as the use of other mathematical and plotting software.

The mass spectrometer was always employed in non-linear mode (also referred as reflectron mode in mass spectrometry literature). Positive ions generated as a consequence of the laser-matter interaction were detected. No repelling electrode was used to extract the ions to the drift

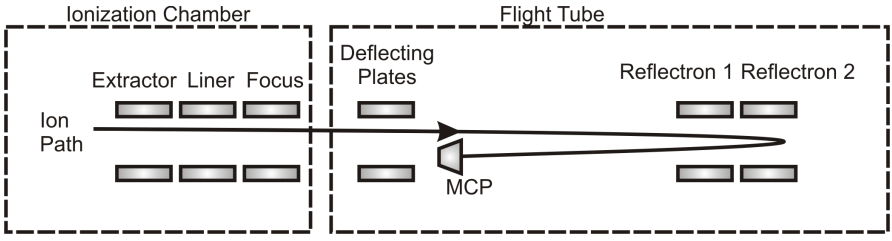

Figure 3.3: Schematic distribution of ionic lenses (electrodes) used to guide ions from the sampling spot to the ion detector.

Electrode	Location	Voltage
Extractor	Ionization Chamber	$-1450V$
Liner	Ionization Chamber	$-1100V$
Focus	Ionization Chamber	$-250V$
Deflecting Plates	Tube Head	$-1010V$
Reflectron 1	Tube End	$-50V$
Reflectron 2	Tube End	$+430V$
Detector	Tube Head	$-3030V$

Table 3.1: General settings for the electrodes used to guide the positive ions to the detector. See Figure 3.3 for an schematic distribution of the lenses.

tube. Instead, a pulsed extractor electrode (up to $-1500V$) placed close to the sample plate was used to suck the ions into the drift tube. An schematic distribution of the lenses inside the spectrometer can be seen in Figure 3.3, while Table 3.1 resumes the settings used for all the electrocstatic lenses.

For a general view of the instrument, Figure 3.4 is a photography showing one of the lasers, the ionization chamber and the flight-tube. As it can be seen in the picture, the whole experimental setup (from the laser to the post-processing computer) is mounted in the same rack.

Figure 3.4: General view of the time-of-flight Mass Spectrometer.

To help getting a better understanding of the instrument and the performed experiments, each and every important component of the instrument will be detailed below. This includes ion source, ionization chamber, sample handler, flight tube, detector and acquisition software, but it also includes some information on the vacuum system employed.

3.2.1 Vacuum System

As any other mass spectrometry, LIMS requires the system to be evacuated to a high vacuum level so that the ions can be transferred from the ionization region to the detector without experimenting collisions.

In order to get a level of vacuum good enough in the ionization region, the pumping system is composed of rotary and turbomolecular pumps.

Three turbomolecular pumps were employed in the ionization chamber (Varian 300H, $300\ L/s$), the flight tube (Varian 250, $250\ L/s$) and the ion gun (Varian V-70, $68\ L/s$). The rotation speed of the turbomolecular pumps was of $56,000rpm$ for the $V-300$ and $V-250$ models, and $75,000rpm$ for the $V-70$.

The vacuum system included also three primary pumps. Two *Varian (MDP12)* rotary pumps connected to the *V-300* and *V-250* and an *Edwards 8 Two Stage* rotary pump connected to the *V-70* turbo pump.

With this setup, typical vacuum in the ionization chamber was in the range of $4x10^{-8}mbar$. To measure the ultra high vacuum a Bayard-Alpert (*Varian 571*) probe was used. A termocouple was used to measure the primary vacuum obtained with the rotary pumps.

This vacuum system assure that the ions were able to impact the detector without any chance to collide with gas molecules during the flight trajectory. In the reflectron mode used, the ions had to cross a distance of about 2 meters. Under the presusure conditions used the mean free path was significantly larger.

This was calculated using the Ecuation 3.1, in which λ is the mean free path, c is a tabulated constant whose value depend on the gas (for air, $6.67x10^{-5}m\ mbar$) and P is pressure.

$$\lambda = \frac{c}{P} \tag{3.1}$$

3.2.2 Ionization Chamber

The system is a multiport stainless steel ionization chamber, capable of working at ultra high vacuum regime. The diagrams for the ionization chamber are shown in Figure 3.5. The chamber is connected to the flight tube from the $CF150$ flange on one side, while the sample manipulator is placed in one of the $CF35$ flange in the upperside and the turbo pump

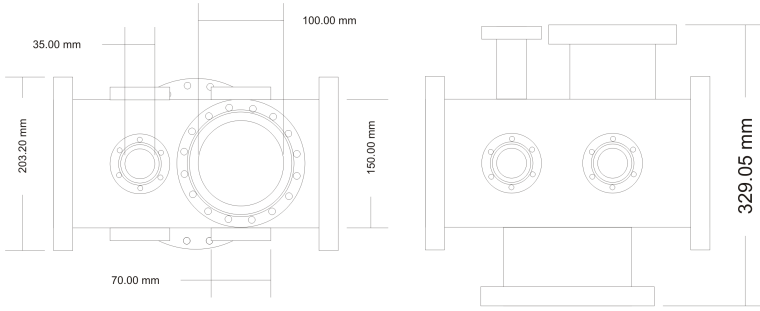

Figure 3.5: Detailed plans for the ionization chamber.

is connected in the $CF150$ flange at the bottom.

3.2.3 Reflectron Flight Tube

One of the problems that time-of-flight analyzers had in the past was its relatively low resolution. Nowadays, big achievements have been proved using a focusing technique developed in the decade of 1950 by Wiley and McLaren[1] and the reflectron developed by Mamyrin in 1973.[2] In our setup, we use both delayed extraction and a non-linear trajectory for ions by using a reflectron in the rear side of the tube.

After being extracted from the ionization chamber, the ions fly to the drift region. The flight tube has a length of $1m$. In the first region of the tube, the deflecting plates allow to redirect the ions by applying a voltage ranging from $0V$ to $-2000V$.

The use of a reflectron improves the resolution by increasing the drift region run by the ions, but also by performing energy compensation. In the first case, ions with different mass-to-charge ratio travel a longer distance, allowing a better separation of different species. In the second case, ions with identical mass-to-charge ratio but different kinetic energy due to the initial dispersion are forced to follow different trajectories

within the reflectron to correct the energy differences. As a consequence, the ion packets are narrower, improving the resolution.

Calibration of a time-of-flight analyzer

Assigning an accurate m/z value to an ion whose flight time has been measured requires the mass spectrometer to be properly calibrated. This is usually accomplished by measuring the flight times of at least two compounds whose molecular weights are well known or with well-defined fragmentation patterns.

The obtained flight time for the selected peaks of the standard sample will then be correlated with the mass-to-charge ratio of these peaks using the flight-time Ecuation (Equation 3.2).

$$\frac{m}{z} = \frac{mt^2}{2} \tag{3.2}$$

3.2.4 Detector

The detector after the flight-tube analyzer is a microchannel plate (MCP) in Chevron configuration and operated in positive mode. Figure 3.6 shows a photography of the MCP taken from the Jordan Inc. website.[3] The plates have a diameter of $18\ mm$. The collision of an ion on the first microchannel plate generates a first ion that goes through one of the channels on the plate and generates more electrons by collisioning with the walls. The MCP detector can be operated up to $-3300V$, but due to safety reasons it was never operated above $-3150V$. Typical work is carried out with the first MCP placed at $-3030V$. The second plate is always at a 54.5% of the first MCP voltage, while the third plate is at 9.1% of the initial voltage.

Each MCP has a thickness of $0.5mm$ and the channels had a diameter of $10\mu m$. The spacing between channels was $12\mu m$. The whole structure

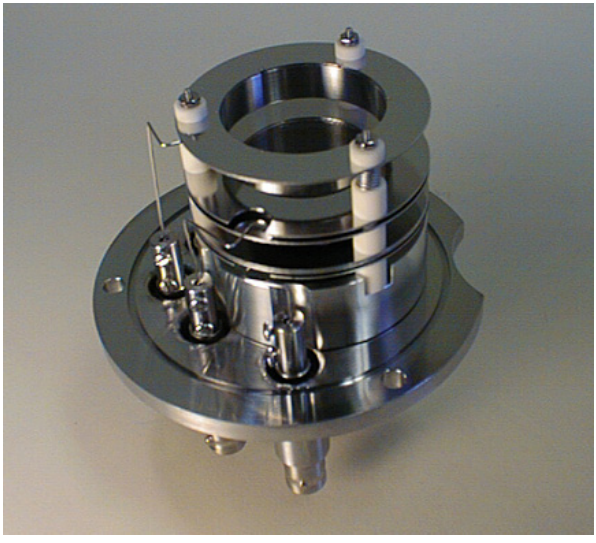

Figure 3.6: Photograph of the 3 MCP detector.

that holds the plates is made of steel, while the channels and the contacts are made of Nickel. The anode is made of steel and is always connected to ground. Beyond the anode collection, signal is transferred to a digital phosphor oscilloscope (DPO) using a $50 - \Omega$ impedance cable finished in a Bayonet Neill-Concelman (BNC) connector.

As the efficiency of the detection strongly depends on the kinetic energy of the ions (not noticeable at low mass range but easily observable while working with macromolecules),[4] the MCP has a grid placed to ground voltage so that ions get accelerated before striking the MCP surface. This allow for greater signal gaining, estimated around 10^6 in our case.

3.2.5 Data Acquisition System

The data acquisition system is composed of two main elements: the DPO and the software devoted to the processing, storage and data post-

processing.

Digital Oscilloscope

Most of the experiments carried out in this memory make use of a four-channel DPO by Tektronix (*Model TDS 5054B*) shown in Figure 3.7. This oscilloscope has a $500\ MHz$ bandwith capable to work at a sampling rate of $5Gsample$. Acquisition of the mass spectrum is performed via the 50Ω transient signal from the MCP, connected to one of the input channels of the oscilloscope. Additionally, the oscilloscope allow GPIB control from an external device for extra features.

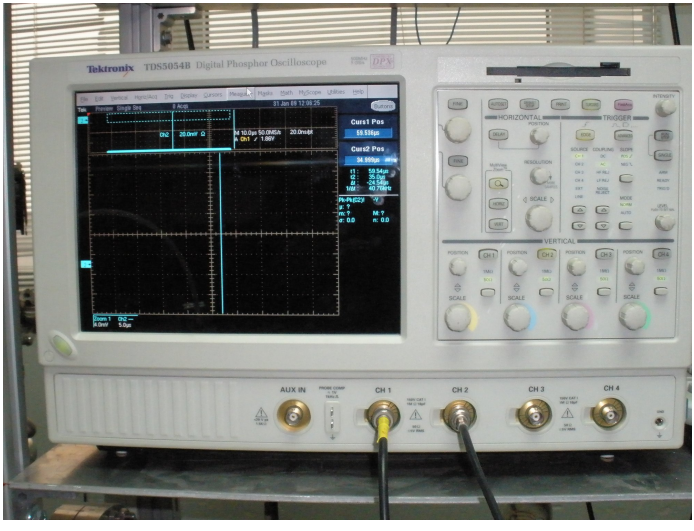

Figure 3.7: Photograph of the Tektronix TDS5054B digital phosphor oscilloscope.

Additional Optoelectronics

A fast photodiode (*Thorlabs DET210*) with a time response of $1ns$ was used to trigger for the experiment. It was usually placed so that it could

receive some scatter light from the laser beam, in order to avoid saturation that could decrease its rise time.

The signal coming from the photodiode was sent to a pulse and delay generator (PDG) by Stanford Research System (*SRS DG535*). This PDG made possible the delay of the ion formation and ion extraction steps. The PDG sent two signals: one goes to the oscilloscope to start the acquisition. The Second one is connected to a pulsed power supply (up to $-1500V$). This pulsed power supply is connected to the extraction electrode so that the ion extraction is delayed in a controlled manner.

Software

The experiments that will be later described make use of two different software interfaces. The first one is the oscilloscope software provided by the vendor (*TekScope*™) and the second one is a Labview™ graphic user interface developed in our laboratory and codenamed *MASAS* (MAss Spectra Acquisition Software). Post processing of the data included the use of some MATLAB™ scripts.

The code for both MATLAB™ scripts and *MASAS* is available in the Anexo I, appended at the end of this Memory.

Tektronix TekScope The digital oscilloscope used includes a computer embeded on it running under *Microsoft Windows 2000*™, where the oscilloscope itself is a *win32* application developed by Tektronix™ that allows to interact with every single control of the instrument. The application is called *Tektronix TekScope*. The look-and-like of this application emulates a typical osciloscope, and it can be seen on Figure 3.8.

Main features of TekScope include the ability of acquiring simulteanously the four independent channels of the oscilloscope, process (math processing, average, ...) them in real time and store the waveform (both directly

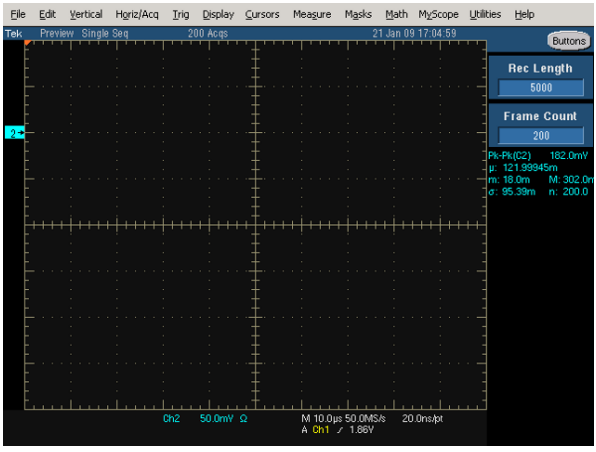

Figure 3.8: TekScope Screenshot. The appearance of the applications emulates the classical look of a phosphor oscilloscope.

acquired waveform or the processed one).

Clearly, one of the most important features of this software is the FastFrame acquisition mode, whose interface can be seen in Figure 3.9. In FastFrame mode the oscilloscope stores in the RAM memory of the computer the waveforms of a selected channel in response to an specific trigger signal. This allowed us to acquire kinetic series for a limited number of events. Depending on the number and resolution of the waveform, a different number of waveforms could be stored before overloading the memory buffer. As a backward, when using FastFrame, only one of the channels of the oscilloscope (at choice) can be acquired. Despite this limitation, the FastFrame mode is a powerful tool that allowed us to perform many of the experiments described in this memory.

MASAS Labview Interface The *MAss Spectra Acquisition Software* (MASAS) is a home developed software that has a graphic user interface to interact with the instrument, acquire mass spectra and store data. When devel-

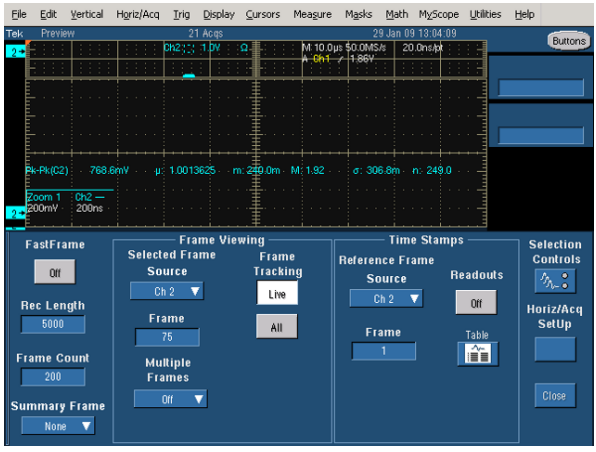

Figure 3.9: TekScope Screenshot showing the interface of the FastFrame work-mode used to acquire kinetic series.

oping a software, there is one crucial decission that can makes you save time and helps you getting and efficient software: choosing the language in which the software will be coded. Our case wasn't an exception.

Despite Tektronix provides documentation on how to write appropiate drivers for the *TDS5000* series, we decided to use the vendor's drivers for the *National Instruments Labview* framework.

Among the advantages of MASAS when we compare it with the default software provided by the oscilloscope vendor, it has some specific features not allowed by *Tekscope* that were needed in our experimental setup. Figure 3.10 shows a screen capture of the main window of the program.

Remarkable features include the ability to perform unlimited kinetic series, as this software saves the data to the hard drive in real time, while *TekScope* just store it in the RAM memory. Another remarkable feature is the ability to analyze data in real time. Basic operations, like baseline correction, can be automatically performed. But also, nice and useful

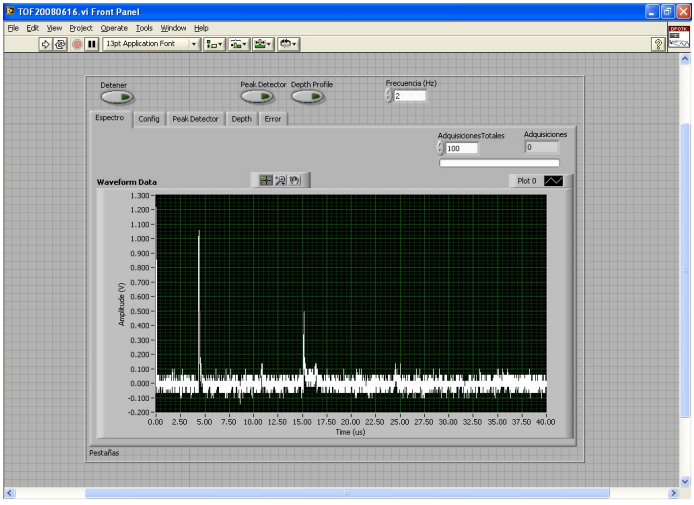

Figure 3.10: MASAS Labview Interface Screenshot showing the main window of the application and the tab containing the plot for real time viewing of the mass spectra.

features like the ability to obtain a depth profile of selected signals in real time are available. The plot of the depth profile will be shown also in real time and the date can be saved to the disk. This task can't be perform using the old vendor's software, and required post-processing work until we developed this new interface.

MATLAB™ Routines Apart from the two main software applications we have used to acquire data in these experiments, different MATLAB™ routines were written to help in the post-processing work. Firstly developed to work with the output file from the TekScope data (a comma separated value with an specific format), this routine could be easily adapted to make some work also with the files coming from MASAS.

This routine was a command-line script written in MATLAB™ language that works with sequential files under an specific naming and puts

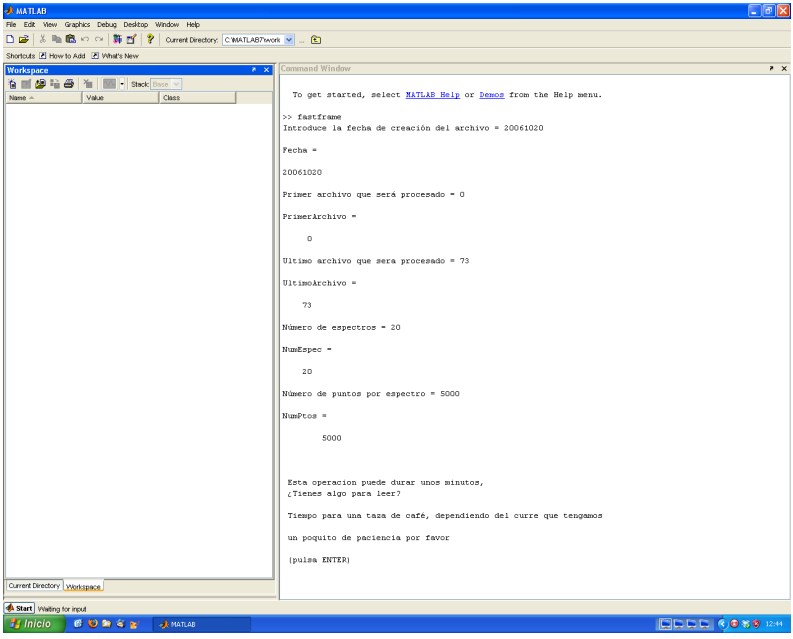

Figure 3.11: MATLAB™ script. The screenshot shows the typical appearance of the rutine when it's run to process some files at a clip.

them into a desired comma-separated value (CSV) format. When the routine is run, it prompts the user for some information about the data to be processed (filename, number of files to process, number of spectra per file, number of points per spectra). Figure 3.11 shows a screen shot of the routine being run, at the time it is asking for these parameters. Despite being a simple routine, the time required to perform this task was reduced ten times upon its use. Hence, a work that used to take half a day of work required only half an hour.

3.3 Specific Configurations

This section will describe the different specific arrangements, settings and devices used throughout the experiments detailed in this memory. The purpose of organizing all the different configurations in one section is providing the reader with the evolution of the experiment, as well as giving a standing point of reference when a given experiment is being detailed.

3.3.1 System Configuration N1

This experimental setup was designed to simultaneously perform mass spectrometry and optical emission spectroscopy of solids irradiated by a pulsed laser.

A general view of this setup is shown in Figure 3.12. For proper understanding of this setup, specific elements are detailed below.

Sample Insertion Probe

The sample is introduced into the ionization chamber using an insertion probe with diameter of $0.5\ in$ already developed in our laboratory.[5] This probe is introduced into the system through a typical ball valve. A detailed description of this sample handler can be seen in Figure 3.13. In this experiments, the chamber was pumped down to $5x10^{-7}\ mbar$ using the vacuum system described above.

Ion Source

The ion source was a *Nd:YAG* (Continuum, *Model Surelite I-20*) operated with its second harmonic output ($532nm$). This pulse has a typical temporal width of $5ns$. Figure 3.14 shows a photograph of the laser. Maximum repetition rate of the laser was $20Hz$, but usually it was operated at a

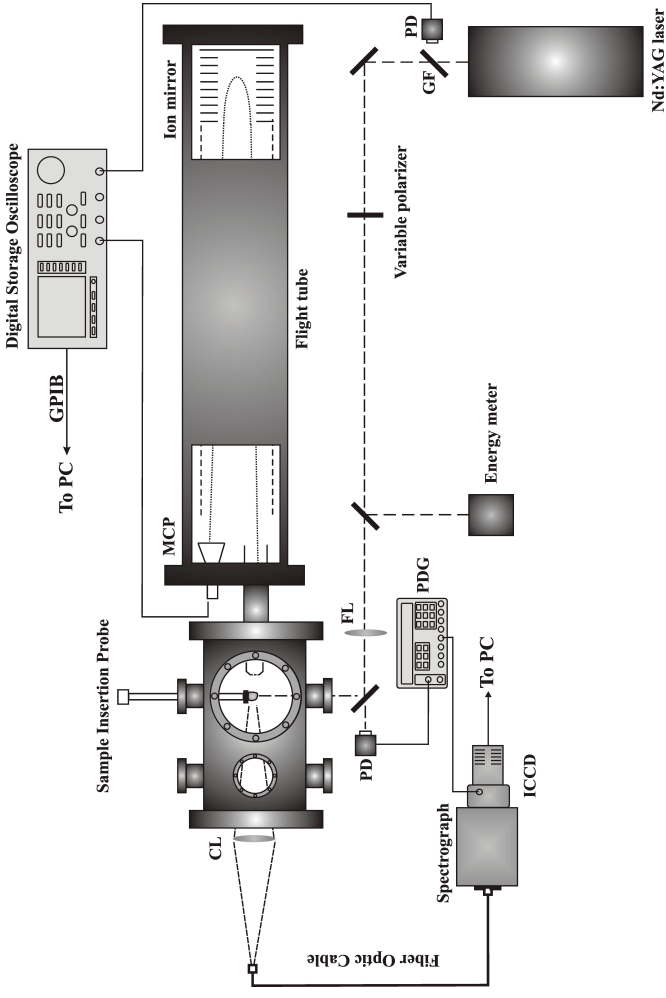

Figure 3.12: Experimental setup. CL: Collection lens; MCP: Microchannel plate; PD: Photodiode; FL: Focusing lens; GF: Glass filter; ICCD: Intensified Charge Coupled Device; PDG: Pulse/Delay Generator.

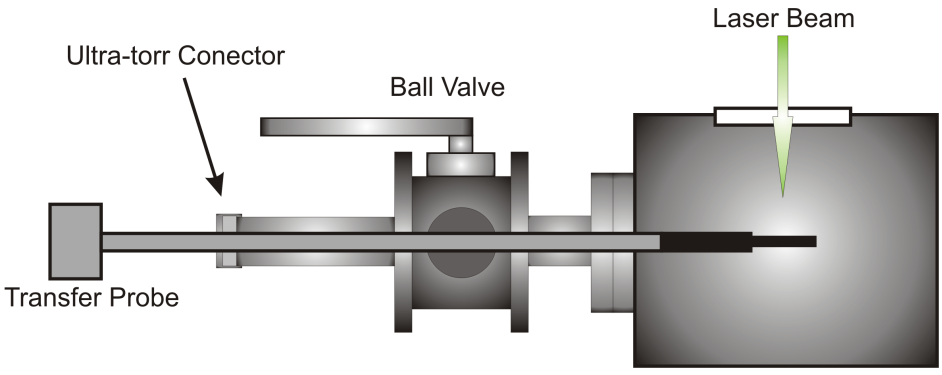

Figure 3.13: Diagram showing the Sample Insertion probe, the Ball Valve and the Sample holder that is screwed at the end of the Transfer Bar.

frequency ranging from $2Hz$ to $10Hz$. Despite the laser has a maximum output of $200mJ$ at $1064nm$ (fundamental output), the usual energy used in the experiment was in the range of a few mJ. Energy was strongly limited and finely controlled to avoid the formation of dense plasmas and preventing the ions from having a too high average velocity in the plasma. High values for this initial velocity of the ions reduce the effectiveness of the extraction field[6] and, subsequently, reduce the quality of the mass spectrum. The laser was focused using a focal lens ($f = 150mm$) at normal incidence to the surface. Also, the laser was operated at its maximum flashlamp voltage and repetition rate to avoid distortions in the spatial profile due to thermal lens effect in the laser rod.

An orthogonal extraction was always used in the experiments described in this Memory.

Energy Control

In order to obtain accurate control over the laser energy, a set of spectroscopic-grade coloured glass filters (GF) exhibiting absorption in the spectral green

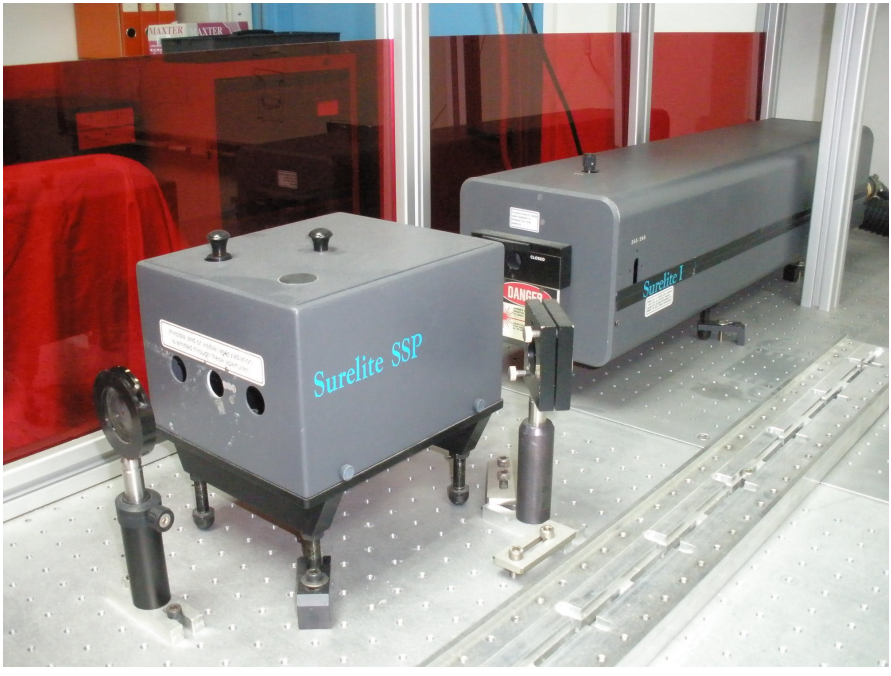

Figure 3.14: Photography of the Continuum Surelite Nd:YAG laser.

region was used to lower the laser energy per pulse to a maximum of $22mJ$. Additional control over the delay in the Pockels cell in the range between 120 and 155 microseconds allowed the generation of pulses between 14 and $21mJ$ with RSD values better than 2% as shown in Figure 3.15. The RSD values correspond to the average of 25 laser shots. A fixed value of 140 microseconds was selected, providing constant pulses of $20\,mJ$ per pulse. For our fluence-controlled experiments, the laser energy was modified in the range between $0.1 - 7mJ$ using a variable polarizer crystal. A thin microscope slide was inserted in the optical path after the polarizer in order to generate a calibrated reflection of the incident beam that was used for individual laser pulses energy readings.

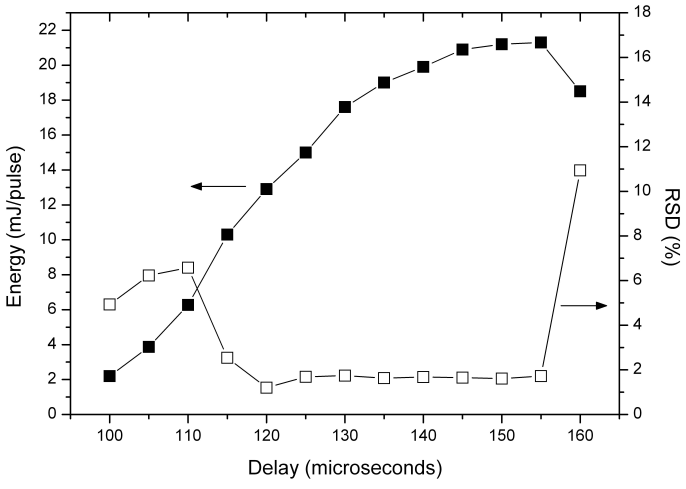

Figure 3.15: Average value and RSD of the laser output as a function of delay in the Pockels cell. Each point corresponds to the average of 25 individual laser shots attenuated by glass filters.

Spectrograph

As observed in Figure 3.12, the selected configuration allows the simultaneous monitoring of both ions and photons generated in the sample after laser incidence.

For optical emission spectroscopy (OES), the emitted plasma light was collected with a quartz lens and delivered to the entrance slit of an Acton Research Corp. (Model *SpectraPro-275*) spectrograph using a fiber-optic cable. The spectrograph has a CzernyTurner configuration with a focal-length of $275mm$ and an aperture ratio of $f/3.8$. The spectrograph is equipped with 3 gratings (300, 600 and $1800grooves/mm$). The spectral windows accessed for each measurement was $293nm$, $143nm$ and $67nm$, respectively, for each one of the gratings. Maximum resolution is $0.1nm$ when the $1800grooves/mm$ grating is selected and slits are set to $10\mu m$.

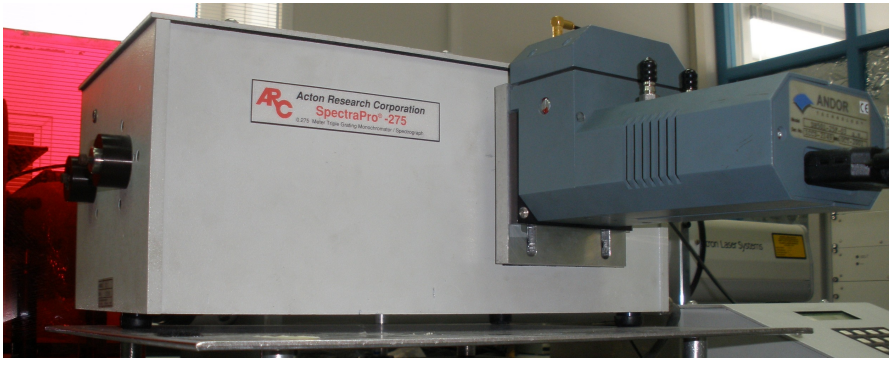

Figure 3.16: Photograph shows the acquisition system for the Atomic Emission composed by the Acton Research Corp. (Model *SpectraPro-275*) spectrograph and the Andor Inc. (Model *DH501-25F-03*) intensified CCD.

Intensified CCD

The dispersed light on the spectrograph was detected with an intensified charge-coupled device (iCCD) by Andor Inc., model DH501-25F-03. The iCCD has an array of $1024x128$ pixels. Pixel area is $26\mu m^2$ and the intensifier diameter is $25\ mm$.

The photograph in Figure 3.16 shows both the spectrograph and the photon intensified CCD detector employed in this setup.

The whole LIBS system was triggered by a fast photodiode (PD) connected to a pulse and delay generator.

3.3.2 System Configuration N2

Ion Source

This system uses for ionization the same *Nd:YAG* laser previously described for configuration N1. Even though, for this configuration we improved both the optic system used to gain energy control and the sample handling system. The setup is shown in Figure 3.2.

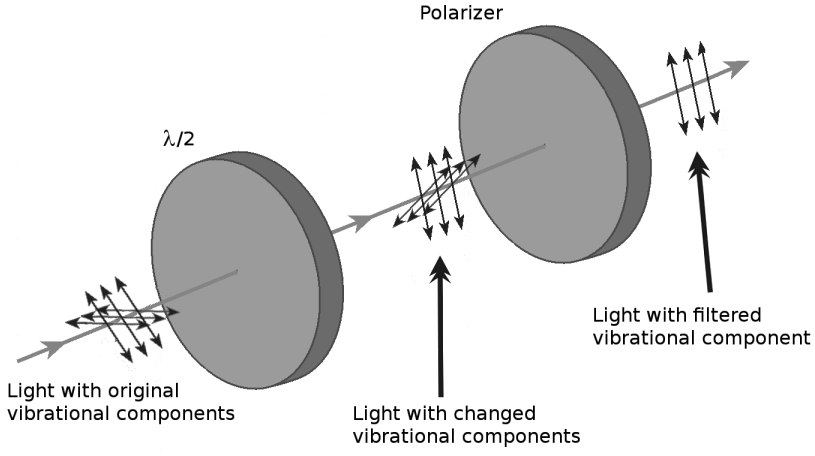

Figure 3.17: Figure shows the effect of the non-linear optics system composed of a $\lambda/2$ waveplate and a polarizer crystal on the polarization of the radiation. The first element will allow us to rotate the vibration plane of the radiation as much as we want. The latter will transmit one component and reflect the other, thus allowing us to control the energy being transmitted to the sample by changing how much we rotate the vibration plane with the waveplate.

Energy Control

To gain fine control on the laser energy, non-linear optics were used. The use of this kind of optics provided a fine control of the energy that was being deposited on the sample's surface without modifying the spatial profile of the beam.

This system includes a half waveplate mounted on a rotating holder and capable of changing the vibration plane of the polarized light. The second element of the system was a polarizer. When working sequentially, we can control the percentage of energy that crosses the polarizer by controlling the vibration plane of the radiation. A detail of this system is shown in Figure 3.17.

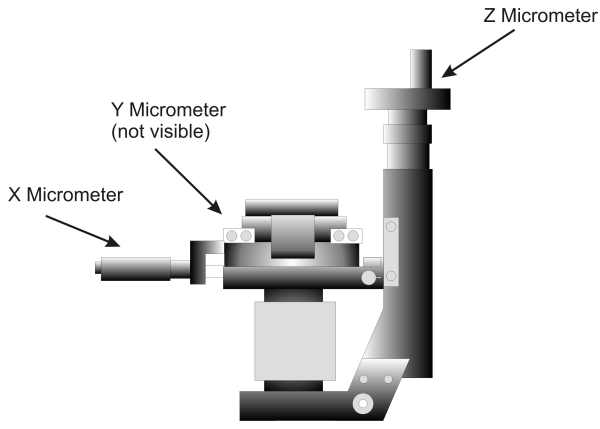

Figure 3.18: 3D micrometer for fine position of the sample.

Sample Handler

The modification performed in configuration N2 allowed control of the sample position with 4 degrees of freedom (x, y, z, θ). An scheme of the 3D manipulator can be seen in Figure 3.18. An additional gate valve provided isolation of a first region of the system, that would act as a load chamber for fast sample replacement.

The new 3D manipulator had three micrometers. The one in the Z axis allowed for a displacement of the sample up to $100mm$, while both X and Y micrometers allowed for a $20mm$ displacement.

3.3.3 System Configuration N3

This configuration shares the same elements as in configuration N2 with the only difference of the use of two laser beams to perform sampling and ionization. New electronics and a synchronization scheme were needed to have the two lasers properly synchronized. An schematic view of the Configuration N3 can be observed in Figure 3.19, showing both new and previously detailed elements.

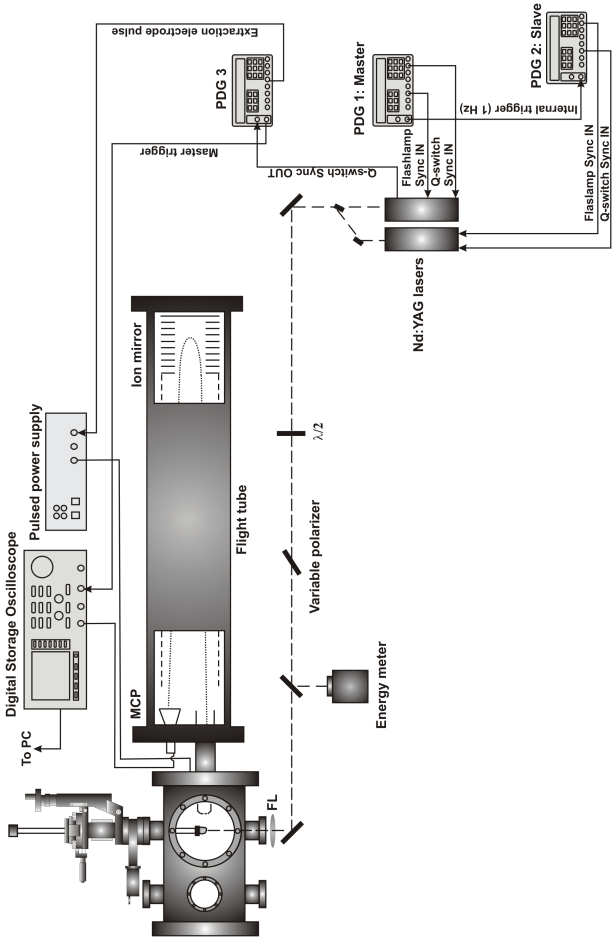

Figure 3.19: Schematic Representation of the Configuration N3, showing all elements from the laser head to the mass spectrometer, including associated electronics.

Ion Source

The ion source for this configuration was composed of two *Nd:YAG* laser heads from Quantel (*Model Brilliant B Twins*). Both lasers were fitted with SHG modules, so that two pulses of $532nm$ (pulse width, $5.0ns$) were obtained. Maximum repetition rate for these lasers is $10Hz$ and maximum pulse energy is $380mJ$, but they were attenuated so that only a few mJ reached the sample. Laser was focused on the sample's surface at normal incidence using a quartz lens ($f = 150mm$).

As in previous configurations, maximum voltage and repetition rate of the flashlamps have been used to avoid distortions in the laser pulse and any possible thermal lens effect that may damage the laser rod.

Figure 3.20 shows a photograph of the two lasers as they have been used with the time-of-flight experiment.

Energy Control

Energy control of each individual laser was performed by controlling the delay in the Pockell cell of each one. As both beams were recombined to provide a collinear output, the variable optic attenuator was used to apply the same attenuation factor to both beams. By proper adjustment of both attenuation steps, it was possible to assure fine energy control without modifications to the beam spatial profile.

Electronics

The addition of a new pulse and delay generator (Stanford Research Systems, Model *SRS DG535*) was used to allow independent control of both laser sources.

As it can be seen in the Figure 3.19, the first PDG acts as the master, controlling the first laser and the second PDG (slave). The second PDG

Figure 3.20: Photograph of the LIMS experiment showing Quantel Brilliant B Twins used as ion source and the time-of-flight experiment.

controls the second laser. Using fast photodiodes (*Thorlabs DET210*) it was possible to monitor both laser pulses in the DPO, to adjuste and correct the delay introduced with the PDG. Figure 3.21 shows the schematic representation of the electronics for this configuration.

3.3.4 System Configuration N4

The configuration N4 is made of small modifications to the previous ones. As the sample manipulation and spectrometer itself remained unchanged, most of the changes in this configurations relate to the ion source (now an ultraviolet laser pulse) and the optical atenuation of the beam. Direct triggering using the TTL pulse of the Q-switch output from the laser was

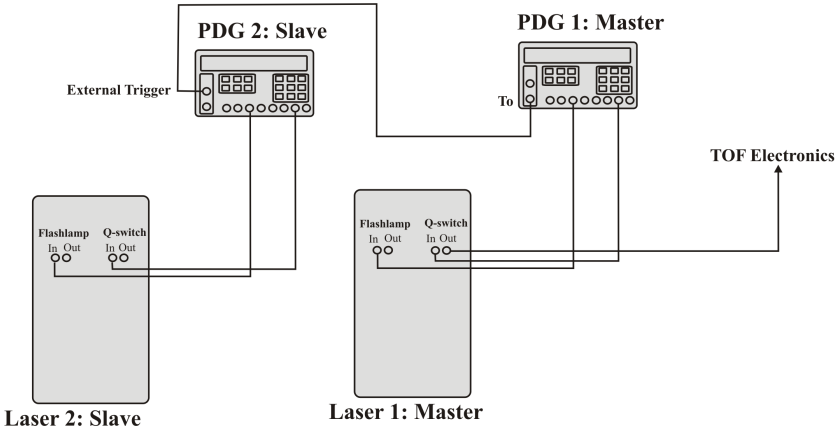

Figure 3.21: Synchronization Scheme for the two lasers and the time-of-flight Electronics.

used instead of the photodiode in previous configurations. This modification was due to the excellent electronics of the new laser source, that provided a TTL pulse with negligible delay with respect to the beam output.

Ion Source

A $Nd:YAG$ from Quantel (*Model BRIO*) with a forth harmonic generator (FHG) to generate a beam at a wavelength of $266nm$ was focused to perform ionization of the sample. Maximum energy for the laser was $100mJ$ when using the fundamental output, and $12mJ$ when using the $266nm$ output.

Energy Control

The configuration N4 includes an advanced attenuation system. Limitations imposed by the new ion source made impossible to use neither the previously detailed non-linear optics system nor the change of the delay

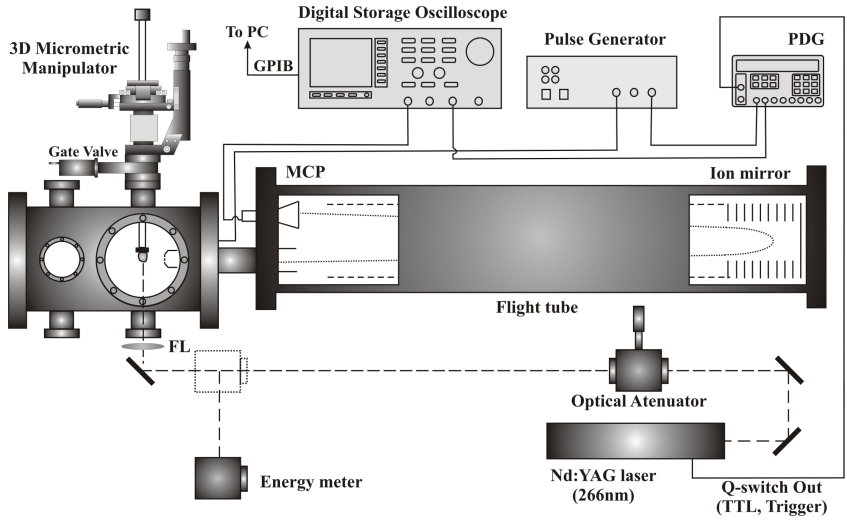

Figure 3.22: Scheme for the Configuration N4, showing $266nm$ laser beam, Newport Atenuator (*Model 935-3/5-OPT*) and new triggering with TTL pulse.

of the Q-switch (DQS) of the laser head. The non-linear optics could not be used as they were not compatible with $266nm$ laser beam.

The DQS could not be modified as the FHG module of the laser produced the frequency sum operates under thermal control. Modifications in the DQS modify the temperature of the crystal, modifying its refraction index and the $266nm$ output in a non-controlled manner.

As none of the previously detailed devices to attenuate the laser beam were feasible, a new optic element capable of attenuate the $266nm$ laser beam was introduced into the system. The chosen element was an optical attenuator by Newport (*Model 935-3/5-OPT*). Planes with an optical configuration can be observed in Figure 3.23. This attenuators is based on the principle of Fresnel reflection from four uncoated, counter-rotating UV fused silica wedged plates. The working range of the attenuator goes from wavelengths as short as $200\,nm$ to the maximum infrared wavelength of $2.1\ \mu m$, covering all the available outputs of the laser head ($266nm$,

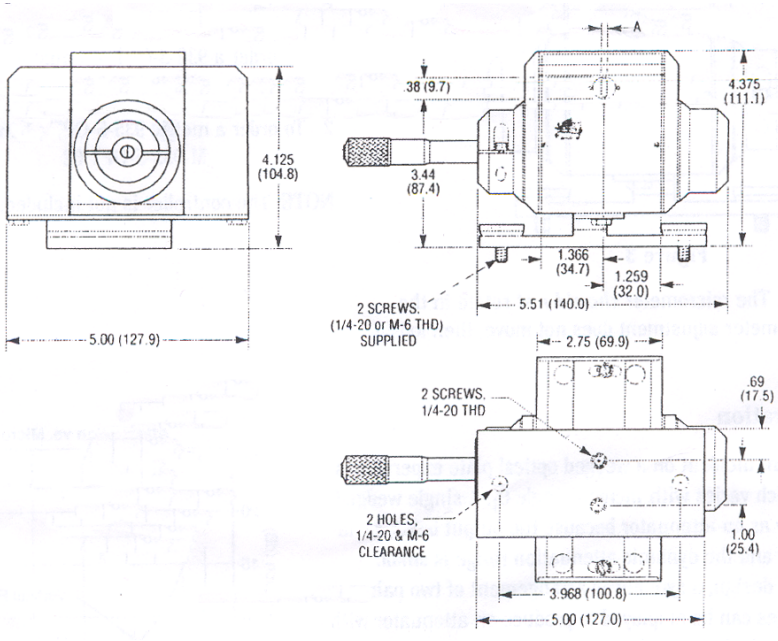

Figure 3.23: Schemes of the Newport 935-3/5-OPT optical Attenuator.

$532nm$ and $1064nm$). The threshold damage for the crystal is 3 Jcm^{-2}, measured with a 1064-nm laser beam.

When a collimated beam reaches the first pair of wedged crystals, the beam suffers some Fresnel reflection. The intensity of this reflection vary depending on the incident angle (θ_τ). This is the basic process by which this optical attenuator reduce the beam energy. A pair of crystals is needed because when a single crystal is used, final deviation depends on the incident angle and, thus, the dynamic range is very limited. By using two crystals, we enlarge the dynamic range of the attenuator and reduce the beam deviation. This design is optimized to reduce the output beam deviation: when two pairs of counter-rotating wedged crystals are used, the second pair can be symmtrycally placed so that the beam deflection is corrected and, therefore, negligible deviation for the output

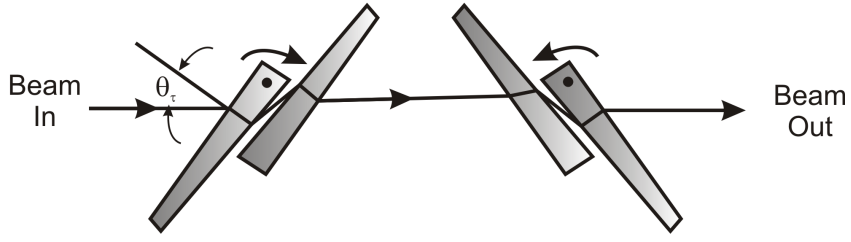

Figure 3.24: The optical attenuator uses two pairs of wedged crystals to produce a controlled level of Fresnel reflection without modifying the optical path for the output beam.

beam from the initial path is obtained.

Chapter 4

Ionization Thresholds on Pure Metals and Metallic Alloys by Laser-ionization Mass Spectrometry

4.1 Introduction

The use of lasers to generate charged particles from solid samples was early discovered by Hönig and Woolston.[1] Laser microanalysis of solids involves the local laser excitation of the target and the subsequent collection and interpretation of the detected signal, which carries the information on the chemical composition of the probed spot.[2, 3] Since then, laser-related mass spectrometry techniques have been widely used to characterize the properties of both bulk and layer structured materials and has also been important sources of fundamental studies in laser desorption, laser vaporization, or laser breakdown processes.[4–7] Several analytical techniques make use of the lasers in such way, among which

laser ionisation mass spectrometry (LIMS) and laser-induced breakdown spectrometry (LIBS) are the most versatile.[8, 9] However, the physics governing the processes is complex and still poorly understood despite of the effort made by different authors.[10, 11]

It is generally accepted that laser-solid interaction is based on a thermal process, where as a result of the laser impact onto the solid target, the temperature of the surface rises, and eventually, the target can melt, and even vaporize.[12] An overall picture of the nanosecond laser-mater interaction involves a thermally activated process induced by surface heating of the sample with little mass transfer, as a nanosecond laser pulse has a duration lasting away the lattice relaxation time. Under this model, the amount of energy reaching a solid sample greatly influences the type of phenomena occurring at the sample surface. While at high irradiance extensive fragmentation, particle emission, and plasma formation is the dominant situation, at low irradiance levels, surface desorption and thermoemission are the common processes. Different efforts to rationale the details of laser-matter interaction have led to the distinction of at least there regimes in opaque materials exposed to Q-switched lasers: a) a low fluence regime ($10^{-3} - 10^{-2} Jcm^{-2}$) dominated by surface heating and soft ionisation of target particles and characterized by a negligible mass transfer across the solid/vacuum interface; b) a medium fluence regime ($10^{-2} - 10^{-1} Jcm^{-2}$) where evaporation of the sample becomes significant, the laser energy is absorbed by both the ionised vapour in front of the target and the target itself and several secondary and non-linear processes occur in the expanding plume, and c) a high fluence regime (over $1\ Jcm^{-2}$) where the deposition of laser energy is governed by the strong absorption of the expanding plasma cloud. So, as laser irradiance energy increases, different sequential processes occur that in the simplest case involves the following macroscopic events: surface heating with thermal desorption, surface melting with surface

evaporation, volume evaporation, formation of an optically thick plume, plasma absorption in the plume and optical breakdown.[13]

The oversimplified description hides a variety of interaction mechanisms that may occur when applying laser light to a solid sample particularly affected by sample characteristics (optical and thermal properties at specific wavelengths) and laser parameters as wavelength, pulse duration, exposure time/accumulative dose and energy density.[14] For fixed sample, laser type, and excitation/collection conditions, the progressive increment of the laser energy released to the target allows the determination of the energy threshold to overcome the different enthalpic steps for each on the energetic steps from simple surface decolouration to phase explosion.[15–17] As soon as a specific fluence threshold is reached, the sample temperature on the irradiated area is high enough to induce significant mass transfer, producing a visible crater, a population of atoms in ground or excited states, ions, electrons and a dispersion of particles in gas phase that can be conveniently transported to secondary excitation techniques to perform atomic or mass spectrometry.[9] Each threshold has own distinctive features and specific enthalpic barriers that will be determined by a single dominating process or several competing processes that makes difficult a microscopic description of the whole process.[18] Each process will be characterized by a different sample behaviour that will need different techniques to be monitored. Thus, time-resolved reflectivity, optical emission spectrometry, mass spectrometry, or time-resolved interferometry techniques are required to determine the different thresholds associated to the laser-matter interaction at the different fluence regimes.

As monitoring of laser-produced events in direct solid analysis is commonly carried out by atomic emission spectroscopy (AES) or mass spectrometry, (MS) and ion formation and plasma expansion take place at different fluence intervals, it is interesting to determine precisely the

transition between the different regimes in order to tune the excitation conditions to the analysis needs. Besides, simultaneous monitoring of the mass spectrum and emission spectrum can also provide information on issues such as calculations of density of ions compared to neutrals, electronic temperature and target surface temperature, among others.

Laser ionization of metals occurs at lower laser fluences that those required for plasma formation/photon emission processes, regardless the physical, thermal or electric properties of the metals studied.[19] The most obvious benefit of performing excitation in the low energy regime comes from the reduced thermal affection in the sample, representing an optimum scenario for laser ablation direct solid analysis.[4,20] However, analysis involving atomic spectrometry needs the formation of a visible plasma that at fluence values close to its threshold is non-stoichiometric with the sample composition, exhibiting selective enrichment in the more easily vaporized elements. From the analytical chemistry point of view the important question arising is the existence or not of fractionation effects in the ionization at the low fluence regime, as it occurs in optical emission spectrometry of laser plasmas.[21] In this case, a careful control of excitation parameters, the use of different matrix-matched standards, or the calculation of relative sensitivity factors are common solutions to correct the bias introduced by the different matrix in the number of detectable species reaching the detector.

In this chapter, seven pure metallic elements are exposed to different laser energies and signals will be simultaneously detected for the produced ions and photons, in order to describe the transition between the different processes. The detection is performed with two sensitive low-noise multichannel detectors (an intensified optical spectrometer and a time-of-flight mass spectrometer) that provide accurate measurements, while the energy is varied in a precise and controlled way not affecting the spatial distribution of the incoming laser beam.

Complementary, experiments investigating the matrix effects in LIMS from a different perspective will be treated. These experiment will establish the differences in the ionization threshold when a given element is analyzed as a pure component or alloyed. For all the samples, the laser energy was finely adjusted while recording time-of-flight mass spectrometry (TOFMS). The relative intensities at close-to-threshold conditions were also studied to improve the perspective of the technique and the comprehension of the underlying process behind the laser-induced solid samples ion formation.

4.2 LIMS/LIBS Coincidence Analysis of Pure Metals

The experimental setup for these experiments have been previously described in Section 3.3.1. Figure 3.12 shows the experimental setup used. The samples were introduced in a multiport stainless steel vacuum chamber using a direct insertion probe previously described.[4] A detail of the ball valve can be seen in Figure 3.13 The chamber was pumped down to $5x10^{-7}$ mbar.

The 532-nm output of a *Nd:YAG* laser was focussed using a $150\ mm$ focal length lens (FL) onto the sample at normal incidence to the sample surface. The laser was operated at its maximum flashlamp voltage and repetition rate to avoid distortions in the spatial profile due to thermal lens effect in the laser rod. Under these conditions, the maximum output was $250mJ$ per pulse. In order to obtain accurate control over the laser energy, a set of spectroscopic-grade coloured glass filters (GF) exhibiting absorption in the spectral green region was used to lower the laser energy per pulse to a maximum of $22mJ$. Additional control over the delay in the Pockels cell in the range between 120 and 155 microseconds allowed the generation of pulses between 14 and $21mJ$ with RSD values better than 2% as shown in Figure 3.15. The RSD values correspond to the average of

25 laser shots. A fixed delay of $140\ \mu s$ was selected for the Q-switch, providing constant pulses of $20\ mJ$ per pulse. For our fluence-controlled experiments, the laser energy was modified in the range between $0.1-7\ mJ$ using a variable polarizer crystal. A thin microscope slide was inserted in the optical path after the polarizer in order to generate a calibrated reflection of the incident beam that was used for individual laser pulses energy readings.

As observed in Figure 3.12, the selected configuration allows the simultaneous monitoring of both ions and photons generated in the sample after laser incidence. For AES, the emitted plasma light was collected with a quartz lens (CL) and fiber-optic delivered to the entrance slit of a $275\ mm$ focal-length spectrograph. Light was dispersed by using the $600\ grooves\ mm^{-1}$ grating of the spectrograph, with a reciprocal linear dispersion of $6\ nm\ mm^{-1}$. The dispersed light was detected with an intensified CCD. The following emission lines were used: $Al(I)$ at $396.15\ nm$; $Zn(I)$ at $334.50\ nm$; $Cu(I)$ at $521.82\ nm$, $Ni(I)$ at $508.05\ nm$; Fe(I) at $495.76\ nm$; $Mo(I)$ at $418.83\ nm$ and $W(I)$ at $407.44\ nm$. A fast photodiode (PD) connected to a pulse and delay generator was used to time the atomic emission measurements. Typically, the ICCD shutter was opened for $1\mu s$, using a delay acquisition after the laser firing of $1\ \mu s$. Real-time single shot spectra were taken, and individually accumulated for post-processing. For mass spectrometry measurements, the generated ions after the incidence of each laser shot were extracted by means of ion lenses and guided to a time-of-flight mass spectrometer operating in the ion mirror (reflectron) mode. After the flight, the ions were sequentially detected with a microchannel plate (MCP). The $50\ \Omega$ transient signal from the MCP was recorded by a $500\ MHz$ digital storage oscilloscope (triggered by a second fast photodiode) and transferred via GPIB to a personal computer for storage and subsequent analytical signal conditioning.

Samples Pure metallic foils of the elements of interest (Zn, Al, Cu, Ni, Fe, Mo and W) were used. The samples were directly affixed to the insertion probe using conductive double-sided tape to ground them. Crater area was estimated for the seven samples exposed to 100 laser shots. The average crater size was $1.46x10^{-3}cm^2$ (with a standard deviation of $0.046x10^{-3}\ cm^2$), corresponding to laser fluences between $0.069\ Jcm^{-2}$ and $4.79\ Jcm^{-2}$ and irradiances between $14.1x10^6\ Wcm^{-2}$ and $0.95x10^9\ Wcm^{-2}$.

4.2.1 Results and Discussion

The experimental determination of the ion formation and plasma formation thresholds was performed by careful control of the energy deposited on the sample and monitoring of the individual events generated. In previous literature on the experimental determination of ablation thresholds,[22] the averaging of a given number of events was chosen in order to improve data statistics. However, under the cited approach, the possibility of correlating single-shot LIMS and LIBS can not be used. As a laser plasma is capable of producing multiple measurable signals coincidental in time (in our case photons and ions), coincidence ion-photon counting may represent a way to internally normalize the analytical signals as it is performed in ion-ion, electron-ion or ion-neutral coincidences in mass spectrometry.[23, 24] Figure 4.1 shows the LIBS and LIMS signals for simultaneous 25 events at three different fluences: $1.88\ Jcm^{-2}$ (Fig. 4.1a, top), $1.19\ Jcm^{-2}$ (Fig. 4.1b, middle) and $0.87\ Jcm^{-2}$ (Fig. 4.1c, bottom).

The relative standard deviation (RSD) for LIBS was improving as the fluence decreases: 4.05%, 3.51% and 1.32%, respectively, for the three fluences plotted. This fact is logical taking into account that over a certain fluence value, the ablation process is highly explosive generating particles of larger size with non-homogeneous distribution. These particles can not be properly vaporized and the result is an impoverishing in the

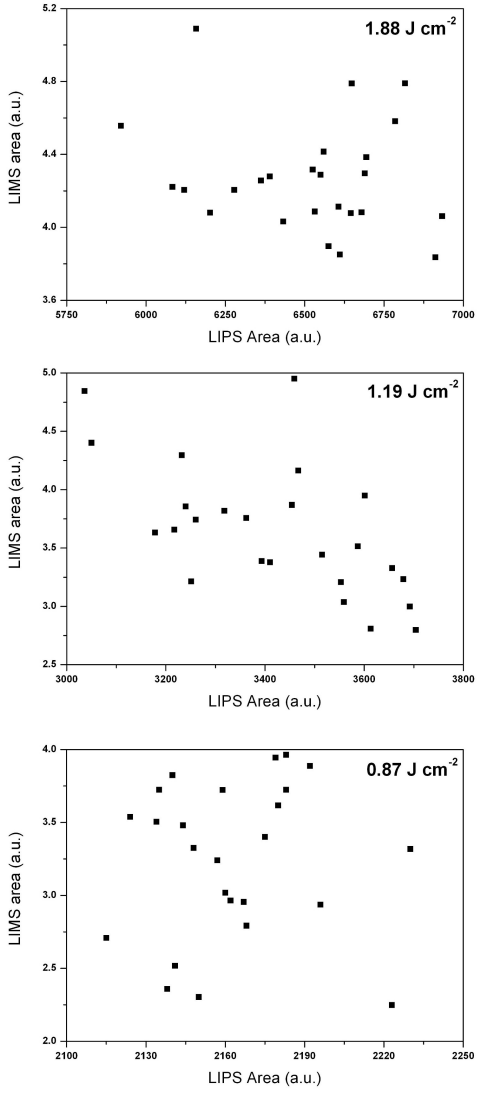

Figure 4.1: Correlation diagrams between LIMS and LIPS signal (as peak areas) for the Al foil and three different fluence values: $1.88\ Jcm^{-2}$ (top), $1.19\ Jcm^{-2}$ (middle) and $0.87\ Jcm^{-2}$ (bottom).

intensity stability. For LIMS, the result was the opposite; the precision deteriorates (7.10%, 15.5% and 16.29%, respectively) as the fluence is lowered. A clear explanation is not found for this experimental fact although taking into account the thermal dependence of ion generation (see below) it might be plausible that this dependence is related to the initial heating of the surface layer and the subsequent thermal emission of ionic fragments. Laser pulses are absorbed by valence electrons of the substrate and the energy is rapidly converted into thermal energy[14] leading to the generation of a strong electric field and the generation of ions by the Coulomb explosion mechanism. By increasing the laser energy, the secondary mechanisms involved in ion generation (additional heating, laser light absorption by the ion cloud among others) dominate the process[15] thus uncoupling the ion generation from the primary mechanism. As a result, the ion current is more stable, and the precision improves. Apart from the differences in RSD values, it is clear from the figure that photon and ion emissions do not correlate. This fact is not taken as a disadvantage as it provides two simultaneous analytical signals originated from different mechanisms that provide complementary points of view of the same phenomena.

Figure 4.2 shows the aspect of the 25 individual events collected for each experiment at three different fluences (from bottom to top, 0.80, 0.83 and 0.92 Jcm^{-2}) for the *Al* sample collecting the ions and photons simultaneously. The plots are shown in 3D to allow the observation of the differences within each data series. As observed, at low fluence (bottom) there is no evidence of ions in any of the recorded events. A slight increase in the fluence (middle) allows the observation of Al ions in 7 out of 25 spectra, while a further increase in the fluence (top) allows the observation of Al ions in every single event. The three plots have been normalized with the peak of highest intensity in the upper plot ($0.15mV$). The three spectra shown have been registered in the flu-

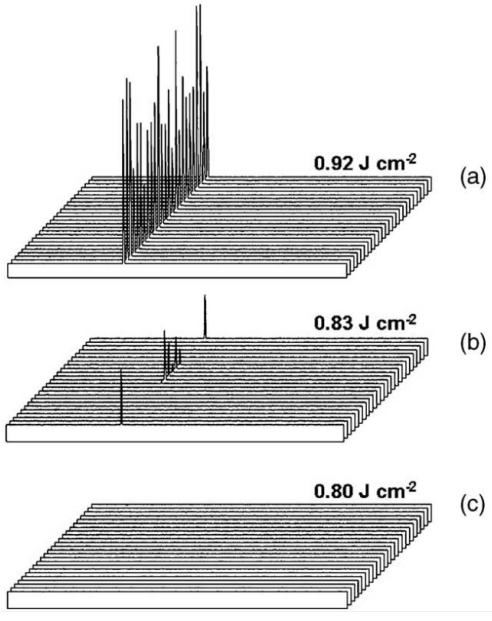

Figure 4.2: Behavior of single shot LIMS data within series at different fluences around the Al ion formation threshold. (a) $0.92 Jcm^{-2}$; (b) $0.83 Jcm^{-2}$; (c) $0.80 Jcm^{-2}$. The three plots are at the same intensity scale (0 to $0.15 mV$).

ence region around the ionization threshold in order to evidence the dramatic effect of slight changes in the energy deposited on the sample. It is important to note that the averaging of the 25 individual events of Figure 4.2b yields a spectrum with a prominent Al signal that could indicate that the fluence conditions were still higher that the ionization fluence threshold. However, the observation of the individual spectra collected evidences that only 70% of the laser shots did not generate any measurable ion (the minimum detectable peak in Figure 4.2b has an intensity of $0.0026\ mV$). For photon monitoring the same behavior was observed: several fluence values with no detectable photons, a region where several events generated low (but detectable) emission, and fluence values from where atomic emission at every event was detectable. As expected,

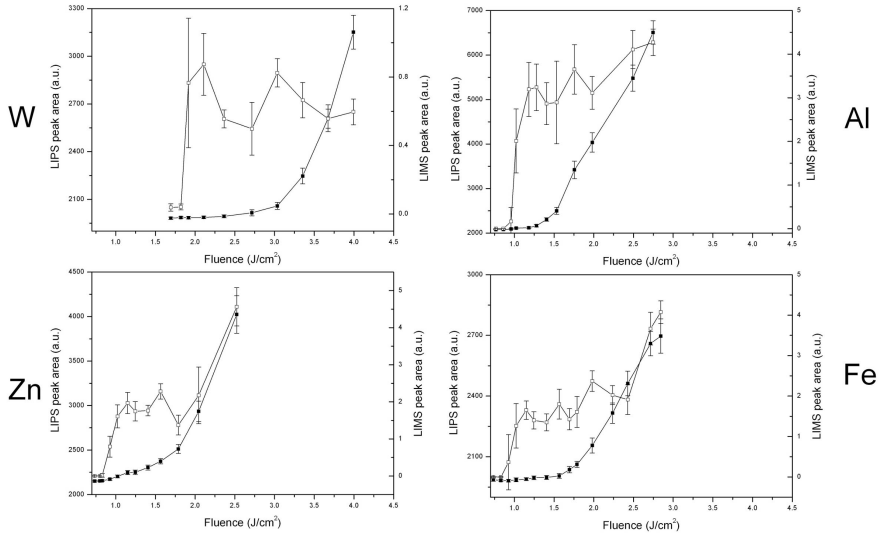

Figure 4.3: Variation of the LIPS (solid squares, left axis) and LIMS (open squares, right axis) intensities for Al, Fe, Wand Zn as a function of fluence. Each point in the graphs represents the average of 25 individual events recorded individually. The error bars represent the standard deviation. The same fluence range has been represented for proper comparison.

for every element studied, there was a shift in the fluences needed to ignite a plasma when compared to the fluence needed to ionize the sample surface.

Figure 4.3 shows the dependence of LIMS (open squares, right axis) and LIPS (solid squares, left axis) peak areas for different elements (Al, Fe, W and Zn) as a function of the laser fluence. The error bars represent the standard deviation for the 25 laser events accumulated in every point. The comparison of the four graphs reveals interesting facts. The overall trend for the four elements is very similar: while in LIPS the signal experiences an exponential growth with increased laser fluence in the range studied, in LIMS the signal drops suddenly to reach a plateau.

Element	Ion formation	Plasma formation
Zn	0.86	1.07 (0.91)
Al	0.99	1.09 (1.30)
Cu	1.18	1.49 (1.61)
Ni	1.28	1.67 (2.07)
Fe	1.20	1.63 (1.56)
Mo	1.50	2.63 (3.12)
W	1.85	2.86 (4.28)

Table 4.1: Ion and plasma formation fluences ($J\ cm^{-2}$) determined in this work. The figures in parenthesis indicate values from the literature[22] for plasma formation in air at atmospheric pressure with the same laser source.

Depending on the element, after this plateau a third region where the ion signal drops again (as in Fe and Zn) can be noticed. Secondly, there is a shift in two of the studied elements (W and Mo) with respect to the fluence axis. As shown for W, at fluences below $1.6\ Jcm^{-2}$ no signals could be detected. This fact is related to their physical properties, as commented upon below. Finally, as expected, the minimum fluence (threshold) for ion detection is always lower than the one threshold for plasma formation. As indicated before, we took as criteria for fluence threshold the minimum energy capable to generate measurable signal at any single laser shot, and not a criteria based on SNR from data interpolation. Table 4.1 summarizes the fluence thresholds for ion formation and plasma formation for the seven elements studied. The values from a previous work[22] obtained for the plasma formation threshold in air at atmospheric pressure for the same elements are also included in the table. As observed, under vacuum conditions the thresholds are slightly lower. This fact is in agreement with the favorable conditions for the ejections of the melted material at low vacuum.

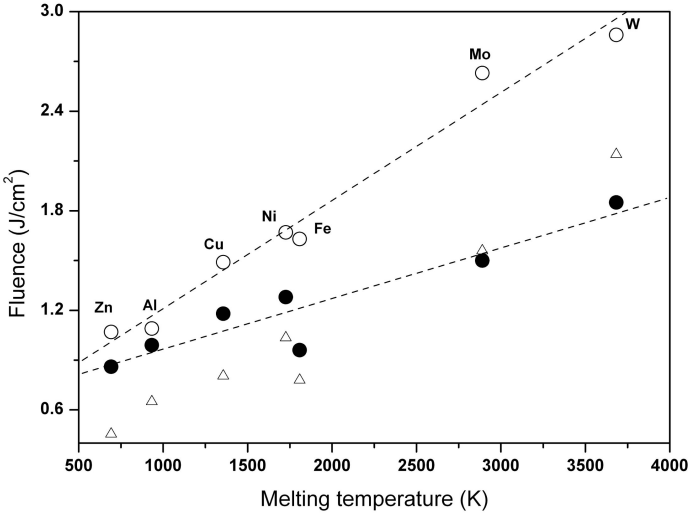

Figure 4.4: Correlation between melting temperature and the calculated values for plasma formation (open circles) and ion formation (solid circles) threshold fluences for the studied elements. The data obtained in air at atmospheric pressure from a previous work[22] have been included (open triangles) divided by 2 to help in the comparison.

Figure 4.4 represents the variation of the determined fluence values for ion formation (solid circles) and plasma formation (open circles) with melting point of the samples. As shown, it exists an excellent correlation in both situations. Plasma formation is known to be highly dependent on thermal properties of the sample.[22] However, it was expected a dependence of ion formation with parameters related to quantum (photoelectric) mechanisms as the ionization potential or the work functions of the metals studied. As can be seen in Figure 4.5, there is no dependence between the cited parameters and the ion formation threshold under the experimental conditions of our experiment. Additional studies with UV wavelengths and studies on the time correlation of the laser pulse width with the ion output pulses must provide a final answer, as the photo-

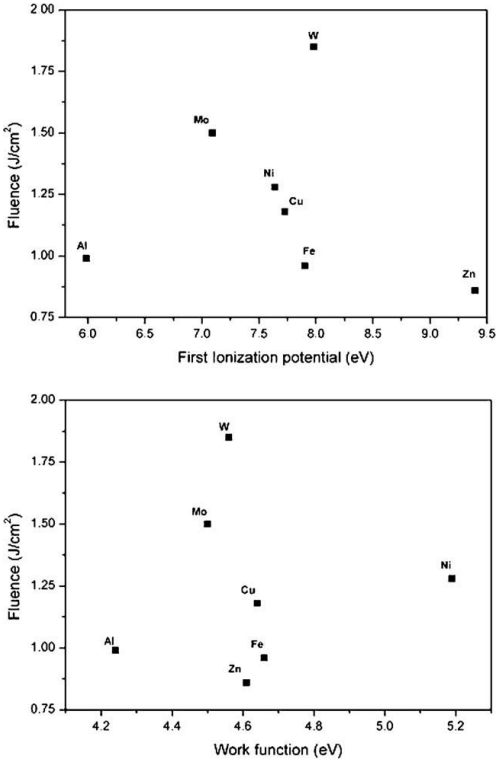

Figure 4.5: Correlation between first ionization potential and work function with the calculated values for ion formation threshold fluence for the studied elements.

electric emission would be simultaneous with the laser pulse.[25] On the other hand, ionization of the bare metal surface is energetically not possible for two 532 nm ($2.34eV$) photons based on the ionization potentials of the metals. The possibility of increasing the photon energy expecting to see evidences of non-thermal effects in ion formation although not tested is obviously open. However, it seems unclear if the experimental approach will help much. It must be taken into account that efficient 2-photon ionization requires a resonant intermediate state with a significant lifetime, so the incidence of two photons at the same time will not

increase the cross sections. Also, even if a resonant intermediate state is accessible, electronic excitations in the conduction bands of metals are very short-lived, so this case is nearly the same as if no intermediate state is available.[26] However, a recent paper[27] has described the non-thermal emission of high-energy ions generated – as postulated by the authors - by the strong electric field created by the electron photoemission process. This Coulomb explosion mechanism has been detected by TOF measurements using a fluence range between $0.01 - 1\ Jcm^{-2}$ using an ArF laser ($h\nu = 6.4eV$). The authors describe ion formation in Si at a fluence value of $0.2\ Jcm^{-2}$, well below the melting threshold, and a clear modification of the kinetic energy of the Si ions as a function of the laser fluence. These results seems to indicate that surface ionization can be much more complex than single photon energy absorption and additional experiments must be done in order to fully understood the complex process involved and how it relates with further plasma ignition.

4.3 Matrix Effects Associated to the Onset of Ion Generation

The experimental setup for this experiment has been described above (see Section 3.3.2 and a graphic scheme can be observed in Figure 3.2. As a reminder, LIMS experiment used a frequency-doubled Nd:YAG (*Continuum Surelite I-20*, pulsewidth: $7\ ns$). The energy output was limited to 10% of its maximum value ($25\ mJ/pulse$) by delaying the Q-switch pulse. These initial conditions provide a laser output without distortions in the original Gaussian beam spatial profile with a shot-to-shot stability better than 3% as measured for a sequence of 500 individual shots using a calibrated energy meter (*GENTEC, QE-12*). The central region of the Gaussian beam was selected by means of an adjustable iris, decreasing the

Alloy	Code	Component Abundance						
		Cr	Fe	Ni	Cu	Pb	Zn	Sn
Fe/Ni	13589J	-	BAL	49.6	-	-	-	-
Ni/Cr	Nimonic	19.69	1.15	BAL	-	-	-	-
Fe/Cr	13765G	19.9	BAL	-	-	-	-	-
Fe/Cr/Ni	Incoloy	20.17	BAL	32.7	-	-	-	-
Bronze	B32	-	-	1.49	74.80	16.10	1.17	5.92

Table 4.2: Reference Certified Binary, Ternary and Complex Alloys. All samples acquired to MBH, except for the Bronze (CTIF).

laser output value to $10\ mJ/pulse$. Fine control of the laser energy in the range 0.4-$2.2\ mJ$ while keeping the shot-to-shot stability was performed by rotating a half-lambda crystal in a 15^{o} interval and removing the non desired polarized component with an optical element placed at 45^{o} with respect to the incident beam. With this setup, we obtained control over the laser energy in $50\ \mu J$ steps without modifications in the spatial profile that could generate undesirable hot spots.

The laser beam is focussed on the sample surface by a 1-inch plane convex quartz lens with a focal length of $20\ cm$. The samples are introduced in the ionization region of the TOF mass spectrometer by a lab-made load-lock system that allows fast sample changing. The sample remained grounded, and can be accurately positioned with four degrees of freedom (x, y, z, θ). A fast photodiode viewing a reflection of the laser beam triggers a pulse/delay generator (PDG) used to pulse the extraction electrode (width: $800\ ns$; delay: $0\ ns$), and provides the starting signal for a digital oscilloscope. Further details of the setup can be found in a previous reference.[16]

The samples used were foils of *Cr*, *Ni*, *Fe*, *Cu*, *Pb*, *Sn* and *Zn* with a nominal thickness of $1\ mm$ and purity better than 95%; reference bi-

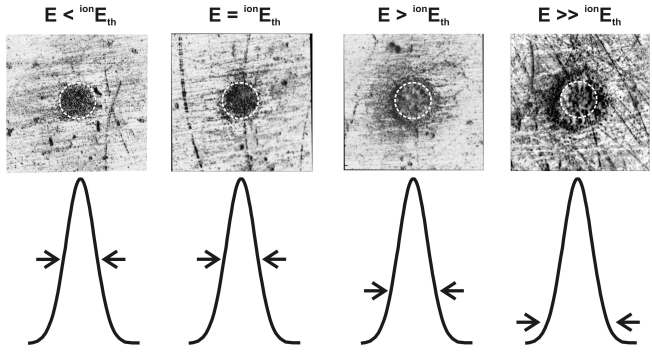

Figure 4.6: Effect of increased energies on the sample affected zone. See text for description.

nary and ternary alloys (*Fe/Ni*, *Fe/Cr/Ni*, *Fe/Cr*, *Ni/Cr*) and a reference bronze sample. The certified composition of the alloys is summarized in Table 4.2. The certified alloys were cut to 1-mm thick squared pieces of $10x10\ mm$ to fit in the sample holder. The cut was performed with a metallographic diamond cut-off wheel. The samples were rinsed with water, methanol and acetone and were left dry in air before the analysis.

4.3.1 Results and Discussion

In order to properly determine the ${}^{I}F_{th}$ of a sample, the laser spot size may be precisely measured. This is due to the nature of the laser-matter interaction process, which is influenced by the way the energy is confined in the solid. For accuracy purposes, this determination must be independent of the biasing effects due to the thermal conductivity of different samples. Our experimental procedure consisted in irradiating a piece of polished Cu foil attached to an end of the sample holder with 50 laser shots at different increasing laser energies. The Cu foil was exam-

ined with an optical microscope to measure the laser mark on the surface. Figure 4.6 shows the effects over the *Cu* foil after the irradiation at four different energy values. From left to right, the laser energy was increased from a value where no signal was recorded, to one producing significant ion signal. The energy range was less than $1.5\ mJ$. At energies below the ion generation threshold (first figure from the left), the laser affected zone (LAZ) corresponds to the area of the incoming beam with sufficient energy to heat the sample above its melting point without ionization. This area, denoted by the authors as minimum laser affected zone (MLAZ), has a diameter of $124\ \mu m$ and it is indicated in Figure 4.6 by the white dashed circle inserted in the micrographs. Additional energy is enough to induce thermoionization without significant mass transfer, generating a LAZ similar to the MLAZ (second figure from the left). Higher energies per pulse produce surface alteration LAZ larger than the MLAZ. As the energy regime is low enough so that phase explosion does not occur, the differences found between the MLAZ and the LAZ are exclusively due to the larger percentage of the incoming beam surface with enough energy to induce surface modification.

This fact is sketched in Figure 4.6 by the arrows indicating the distance from the peak centre where surface melting occurs. Considering the Gaussian distribution of the incoming beam, most of the energy in every pulse will be confined in the beam radius. Most precisely, 86% of the energy is confined within a circle of a radius determined by the FWHM of the beam,[28] corresponding morphologically with the measured MLAZ. As long as the energy per pulse increases, even at energies below the crater formation, the tails of the Gaussian distribution will have energy enough to induce sample damage, vaporization or even ionization, increasing the LAZ. The use of the LAZ instead of MLAZ in the ${}^{I}F_{th}$ calculations, introduce underestimations given by the ratios of their respective values. In the particular case of the last micrograph in Figure

2, the fluence value using HAZ would be 60% lower. For higher laser energies, where thermal conductivity factors become relevant and sample dependent, the overestimation can be significantly larger.

The energy threshold was calculated by recording 100 individual mass spectra at fixed laser energy per pulse. The background level and ion intensities were individually calculated and ratioed to determine the variation of the signal-to-background (SBR) as a function of laser fluence. The ${}^{I}F_{th}$ was taken as the laser fluence at which the onset of ion generation can be detected with a signal-to-background (SBR) higher than 1.5 in all of the individual events.

Once established a threshold criteria, the procedures to determine in what extent the differences in the laser spot size modify the ${}^{I}F_{th}$ were carried out. This fact has been previously subject of interest in MALDI for a Gaussian profile laser beam,[29] where it was observed that a reduction in spot diameter from $280\ \mu m$ to $70\ \mu m$, yielded an increase in threshold fluence by about 1 order of magnitude. Also for MALDI, experiments with flat-top profile yielded the same trends in the fluence threshold values.[30] The same tendency has been also observed in the determination of the fluence damage threshold for femtosecond laser pulses: a decrease in the threshold value by a factor of two when the beam diameter increases from $160\ \mu m$ to $560\ \mu m$.[31]

Our studies, represented in Figure 4.7, were performed in a pure Cu foil by modifying the lens-to-sample distance to generate spots at the sample surface with diameters ranging from $124\ \mu m$ to $256\ \mu m$. The ions extraction voltages were kept to avoid modifications derived from different experimental conditions. The laser energy was controllably increased for each spot size while recording 100 individual mass spectra per experimental point. In the figure the signal-to-background ratio is plotted against the fluence. As observed in the upper plot, the ion intensity is negligible until certain threshold fluence is reached. From this point, the

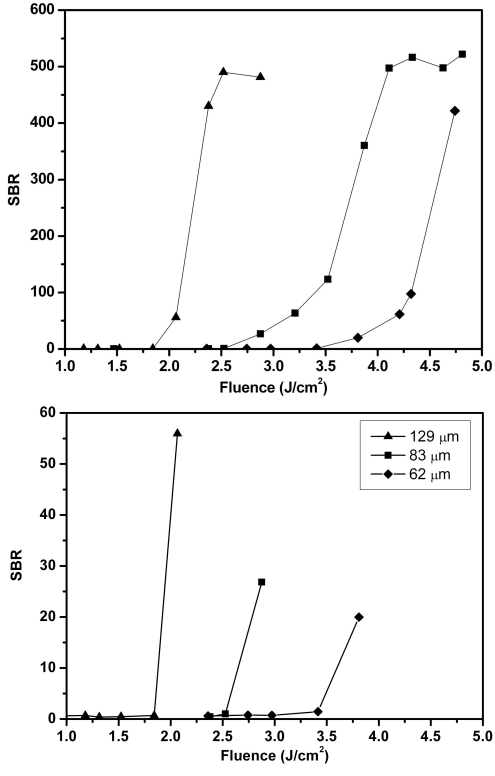

Figure 4.7: Variation of the SBR for *Cu* as a function of the beam diameter. Above, full series of data. Below, detail of the threshold region. See explanation in text.

signal increases up to a plateau that coincides with the appearance in the mass spectrum of doubly charged ions. Increased energy produces a complete loss of resolution in the spectra due to the intense plasma generated in the chamber that may produce electrical shorts between electrodes due to its electrical conductivity. The lower plot represents a zoomed view of the region where the fluence required for the transition from condensed to gas phase occurs. As observed in Figure 4.7, for progressively smaller spot diameters of $256\ \mu m$, $166\ \mu m$ and $124\ \mu m$, the ionization thresholds values are $1.80\ Jcm^{-2}$, $2.65\ Jcm^{-2}$, and $3.40\ Jcm^{-2}$,

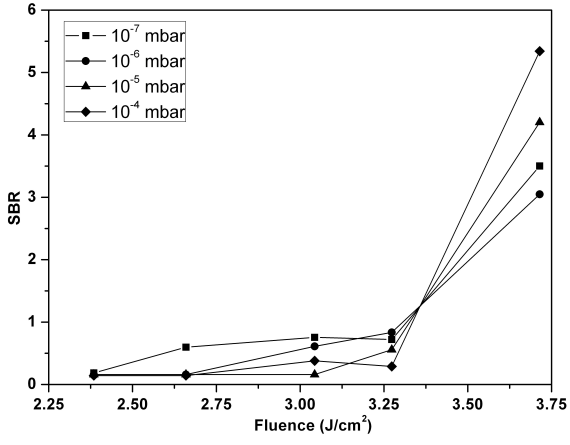

Figure 4.8: Variation of the SBR for *Cu* at different vacuum levels in the analysis chamber. See additional explanation in text.

respectively. The error in the measurements was calculated to be lower than 10% for five replicates at each energy value and focal conditions.

The thermal mechanism of ion generation during nanosecond laser excitation requires the sample to be heated up above its vaporization point at the specific pressure of the experiment. Because the irradiation occurs in vacuum, it is necessary to use the boiling point at the pressure value at which the sublimation is induced.[32] According to the Clausius-Clapeyron equation, the low density environment decreases the energy required to overcome the vapour pressure, making the vaporization points lower than at atmospheric pressure, where are commonly tabulated. Based on this simple thermodynamic model, a diminution in the pressure level during the laser ionization process may reduce the fluence threshold. Previous studies performed on Si [33] have demonstrated that this premise occurs during the studied interval from atmospheric pressure to $5x10^{-4}\ mbar$.

In order to test the effect under the ultra high vacuum conditions

required for laser ionization mass spectrometry, a Cu foil was irradiated with series of 100 laser shots of a spot size of $124\ \mu m$ at increased energies per pulse in the pressure range between 10^{-4} to 10^{-7} mbar. A plot representing the variation in the SBR with laser fluence is shown (Figure 4.8). Our results indicate that the ${}^{I}F_{th}$ value under the pressures range studied remains constant, adopting a value around $3.40\ Jcm^{-2}$, in accordance with the results obtained previously. A careful examination of the data at the fluence values below the threshold, indicates that at 10^{-4} and $10^{-5}\ mbar$, the SBR remains below 0.5 before the ionization threshold, where the inflexion point occur. At 10^{-6} and $10^{-7}\ mbar$, the SBR is significantly higher at low fluences than at higher pressures, although the inflexion points for a $SBR > 1.5$ occurs at the same value regardless the background pressure level. This fact could be an indication of the early instabilities in the surface due to the melting process (surface damage), favoured by the low pressure as expected by the theory. This explanation is in agreement with the work carried out by several authors [34, 35] where the fluence threshold values for surface modification are lower than those required for sample melting or vaporization. Enhanced sensitivity in our detection system might help to determine by mass spectrometry the early ions coming from the initial surface heating. It is remarkable the larger SBR exhibited by the samples at higher pressures once the threshold has been reached. In principle, it would be expected that the better expansion and lower ion collision at low pressures would help to increase the ion signal. However, our experimental results seem to be more compatible with an enhancement in the ion signal due to the reduction in the ion dispersion in the focal volume as the expansion occurs in a denser media.

Once established the behaviour of the experimental variables that could affect our measurements, the ${}^{I}F_{th}$ for a set of pure metals were studied. The experiment consisted on series of consecutive 100 mass spectra acquired at different laser pulses energies between $0.25--1.50mJ$,

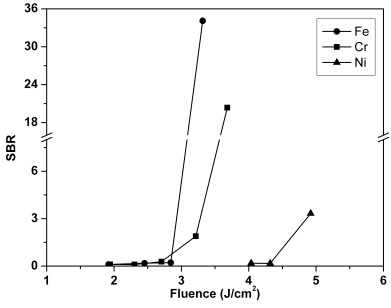

Figure 4.9: Determination of the ionization threshold for pure foils of *Cr* (square), *Fe* (circle), and *Ni* (triangle). Above, full series of data. Below, detail of the threshold region. The signal from the ^{52}Cr, ^{56}Fe and ^{58}Ni were used for the determination. The ionization threshold for the three elements is taken as the fluunece value providing a $SBR > 1.5$.

corresponding to fluences between $1 - 5\ Jcm^{-2}$ for a spot size of $124\ \mu m$. The most abundant isotopes for every element (^{52}Cr, ^{56}Fe and ^{58}Ni) were processed for every individual spectrum. Figure ?? shows the $^{I}F_{th}$ calculated for pure *Cr*, *Fe* and *Ni* foils. As in Figure 4.7, the whole range of fluences studies is shown in the upper plot, while a zoomed view of the region where the condensed to gas phase is shown in the lower plot. Following the same SBR-criteria already taken, the energy threshold condition was satisfied for *Fe* at *1.29 mJ/pulse* ($2.85\ Jcm^{-2}$); at *1.44 mJ/pulse* ($3.15\ Jcm^{-2}$) for *Cr*; and at *2.13 mJ/pulse* ($4.60\ Jcm^{-2}$) for *Ni*. The error in the measurements was calculated to be 10% as determined by five replicates at each energy value for the different elements.

A set of binary and ternary alloys with certified composition in *Cr*, *Fe* and *Ni* (detailed in Table 4.2) were studied. The calculation of the $^{I}F_{th}$ was performed following the same experimental procedure used with the pure foils. The results are graphically depicted in Figure ??a, where the SBR vs. laser fluence plots show the different behaviour of the Fe-based

Alloy	Ionization Threshold ($J\ cm^{-2}$)	SBR at threshold fluence		
		Fe	Cr	Ni
Ni/Cr (80:20)	4.07	-	10.76	4.51
Fe/Ni (50:50)	4.32	20.39	-	4.99
Fe/Cr (80:20)	2.84	5.80	17.04	-
Fe/Cr/Ni (48:32:20)	3.68	11.24	24.53	3.36

Table 4.3: Ionization Threshold for Reference Certified Binary and Ternary Alloy.

alloys. As observed in Figure 4.10, the different ions present in each sample are detected with a $SBR \geq 1.5$ at the similar fluence values, summarized in Table 4.2. As observed, considering the 10% error associated to the ${}^{I}F_{th}$ determination, it is possible to conclude that all the elements in a specific alloy do exhibit the same value. In general, the alloys with the higher concentration in *Ni*, do have the larger ionization threshold, while *Cr* has the opposite effect, decreasing the threshold as its presence is larger. However, calculated ${}^{I}F_{th}$ for the elements in the alloys differ from the values calculated as pure foils as can be seen in Figure 4.10, where the dashed lines indicate the ${}^{I}F_{th}$ values for pure *Fe*, *Cr* or *Ni*. The absolute difference in all the situations is lower than $1\ Jcm^2$ with respect to the value as pure foil, with variations as high as 50% as can be seen in Figure 4.11 where the X axis has been ratioed with respect to the ${}^{I}F_{th}$ as pure foil for *Fe*, *Cr* and *Ni*. The explanation to these variations must be found in the way that the metallographic structure does modify the thermal properties of the alloy. Unfortunately, the certification of the samples does not include information about the thermal properties of the alloys. Experiments using differential calorimetric techniques might be useful to determine the thermal properties of the alloys and correlate them with the thresholds.

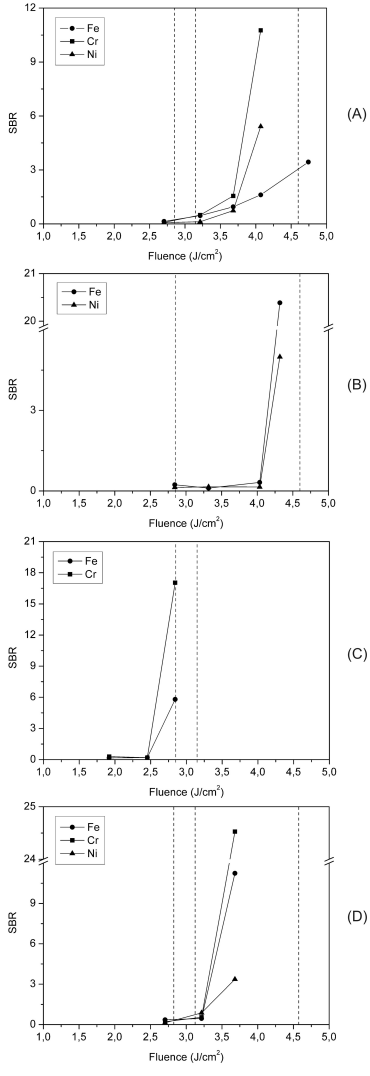

Figure 4.10: Variation of the SBR for different elements in multielemental *Fe*-based alloys with laser fluence. See text for explanation. a) MBH Nimonic, b) MBH 13589J, c) MBH 13765G, d) MBH Incoloy.

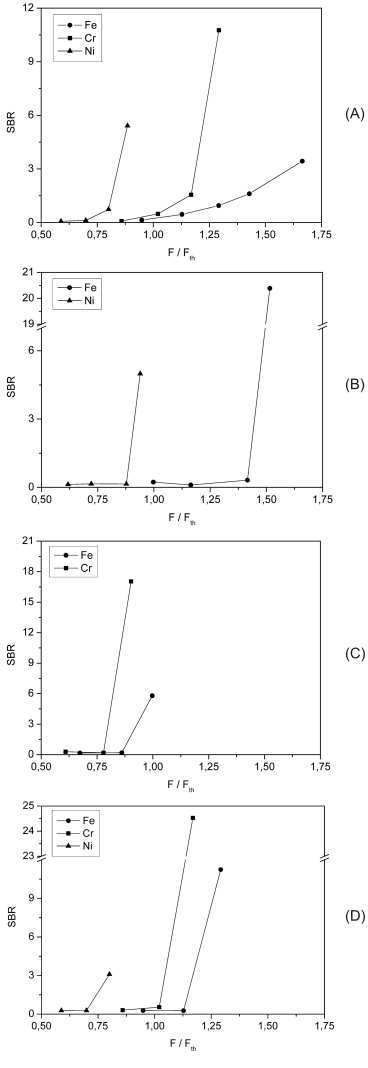

Figure 4.11: Variation of the SBR for *Cr*, *Ni* and *Fe* in the four *Fe*-based alloys studied with the normalized laser fluence (ratioed to the fluence threshold for each element). See text for explanation. a) MBH Nimonic, b) MBH 13589J, c) MBH 13765G, d) MBH Incoloy.

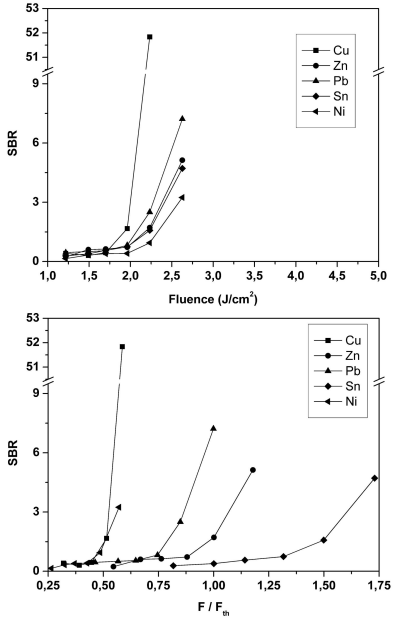

Figure 4.12: (top) Variation of the SBR for different elements in a bronze sample with laser fluence. See text for explanation. (bottom) Variation of the SBR for *Cr*, *Ni* and *Fe* in the four *Fe*-based alloys studied with the normalized laser fluence (ratioed to the fluence threshold for each element). See text for explanation.

Calculation of ionization thresholds for bronze

A bronze sample was used in order to determine if the behaviour previously observed was specific of the Fe-based alloys, where the *Cr*, *Ni* and *Fe* do not exhibit large dissimilarities in their melting and vaporization points. As in the previous examples, the ionization thresholds of the elements constituting the sample (see Table 4.2) were determined for the ^{64}Zn, $^{120}Sn4$ and ^{208}Pb isotopes with the following values: $1.49\ Jcm^{-2}$ for *Sn*; $2.23\ Jcm^{-2}$ for *Zn* and $2.63\ Jcm^{-2}$ for *Pb*. The *Cu* and *Ni* thresholds ($3.40\ Jcm^{-2}$ and $4.60\ Jcm^{-2}$, respectively) were previously determined. Figure 4.12a represents the SBR as a function of laser fluence for the

bronze sample. All the elements present in the alloy do start the ionization at close fluence values (in the range between 1.9 and $2.2\ Jcm^{-2}$) following the $SBR\,1.5$ criteria. When the data are ratioed to the ionization threshold as pure foils (Figure 4.12b), it is remarkable the differences between elements with respect to their values as pure foils (more than 50% for *Cu*, *Ni* and *Sn*). Again, the information provided by differential thermal analysis could be of key interest to correlate our results.

4.4 Conclusions

Through this chapter, the analysis of solid, inorganic targets have been performed. Two different approaches have been taken: first, coincidence analysis was done so that the possibility of an ionization regime in absence of plasma could be ruled out; second, influence of some parameters like the matrix surrounding the analyte have been considered.

As a result for the simultaneous LIPS/LIMS experiment, the fluence transitions between the vaporization-only and plasma formation regions for seven metallic targets (*Zn*, *Al*, *Cu*, *Ni*, *Fe*, *Mo* and *W*) using nanosecond laser pulses have been monitored. The fluence thresholds for ion emission and plasma formation have been calculated. In every case, the threshold value for ion formation was always lower than for plasma formation and exhibits dependence with melting point of the metal. This fact evidences a thermal process in both plasma formation and ion generation under the experimental conditions.

A comparison between the ionization-threshold fluence exhibited by a set of pure metal foils (*Cr*, *Ni*, *Fe*, *Cu*, *Pb*, *Sn*, *Zn*) and certified alloyed samples have been performed. A selection of experimental conditions involving the laser beam energy/geometry and the working pressure has been checked to determine their influence on the ionization threshold determination. The criteria to determine the value of the threshold was

based on the fluence value providing a SBR higher than 1.5 in all the events within the data series. For all the alloys studied, it has been checked the existence of a common ionization threshold for all the elements present in the samples. This ionization threshold differed from the one of the different elements present when determined as pure foils, with deviations as large as 75% in some cases. The origin of these deviations must be found in the way that the metallographic structure of the alloys modifies their thermal properties. Further experiments may be carried out to find out similarities and differences when a radiation with different wavelength (mainly, UV light) is used to excite the solids, as different mechanisms like thermal and photo-ionization may compete.

Chapter 5

Analyis of Metals using Two Subthreshold Laser Pulses

5.1 Introduction

Laser ablation of metals implies the interaction of a pulsed laser with the sample surface, a sudden rising in the target temperature, the generation of a plasma, and the subsequent mass transfer.[1, 2] Due to its experimental simplicity and sampling flexibility, optical emission spectroscopy of laser-induced plasmas (commonly known as LIPS, Laser-induced Plasma Spectroscopy) has established as a mature technique within the modern analytical spectrometry.[3, 4] The large number and diversity of the different analytical scenarios where the technique has been successfully applied support the usefulness and undoubt interest of the technique.[5, 6]

Laser ablation is a complex process, consisting collectively of many nonlinear mechanisms covering several orders of magnitude in timescale, from femtoseconds to seconds. A whole picture of the process starting from the initial reaching of the laser to the sample implies the releasing of electrons from the surface (in the femtosecond to picosecond timescale) due to both photoelectric and thermoionic emission.[7–9] During this

process, there is a transfer of energy to the lattice that undergoes several thermal phenomena in the nanosecond timescale, including rapid heating of the surface, non-equilibrium phase change, superheating of the sample underneath, and rapid nucleation of material in the superheated liquid.[2] It is possible to invoke the classical picture of thermal vaporization from a heated metal surface through transition to the liquid phase to describe material removal at time scales that allow establishment of local thermal equilibrium. That would be the case for our experiments, since relaxation times in metals are in the sub-picosecond regime and will not account due to the nanosecond duration of our excitation.[10] Under this situation the sample target experiments almost instantaneously but sequentially, melting, vaporization, and plasma formation.[11] Depending on the sample, the energy demand of each of the independent processes described may be different.

Not only atomic optical emission, but also mass spectrometry can used to obtain information about the sample nature after irradiation with a pulsed laser as long as the generated ions can be properly collected and analyzed. One of the key interests in the laser ionization of metals relies in its lower energetic demand in comparison to the plasma formation/photon emission process. For any metals studied with a large difference in physical, thermal and electric properties, the ionization process may take place without the need of plasma formation.[12] In this sense, applications demanding gentle laser-matter interaction as desorption of large molecules or analysis of thin layers benefit from the softer excitation conditions. The lower the energy density, the lower the sample damage due to thermal effect and, thus, laser ionization of solids with nanosecond lasers may still be a realistic and affordable option for direct solid analysis without the need of ultra short lasers when reduced heat affected zone is acceptable. Unluckily, working at such low fluence values implies a concomitant lost of analytical signal.

The different phenomena occurring during laser ablation at different time scales and fluence regimes have been an active field of research in the last years. Due to the relevance of the applications, studies in the low fluence regime where laser desorption of organics takes place have been of principal interest.[13] A deep understanding of the behaviour of a laser beam when impinges the surface of a solid metal has also gain attention due to the applications of the method in growing thin films or in direct chemical analysis.[14]

Time-resolved studies based on photon emission of the expanding plume have been extensively used in the literature to monitor laser plasma-based processes.[1, 6] As long as a laser plasma is required, a minimum energy threshold is needed. As plasma formation implies the target phase explosion, the phenomena occurring at much lower energy, when the target experiments normal vaporization gets masked under the energetic conditions. This fact has been evidenced by using shadowgraphs of the laser-matter interaction at different fluences,[15] allowing a clear visualization of the transition from normal vaporization to phase explosion regime. Above the threshold, the superheated surface explodes into a mixture of droplets and vapour, in coincidence with the reaching of the laser pulse. At subthreshold fluences, the vaporization process continues far beyond the laser pulse duration without producing phase explosion in the target.

Some experiments have shown that ionization of metals can occur at very low fluences, even below the perceived melting threshold. Solis et al.[16] demonstrated the possibility of non-thermal ejection of ions from laser-ablated Ge surfaces using an $308 - nm$ ablation laser at fluences in the interval between 0.05 - 0.8 Jcm^{-2}. The melting fluence threshold for Ge was estimated to be 0.3 Jcm^{-2}, while ion signals were detectable at fluences as low as 0.08 Jcm^{-2}. Visible plasma formation was only detectable at a threshold value of 0.6 Jcm^{-2} with escape velocities of the

ejected species of $0.3\ nm/ns$. Similar results with Si and Ge were obtained by Chen et al.[17] In both studies, UV lasers were used, that could help in the reduction of thermal effects and in the difference between the ionization and the melting processes. Experiments in ion-photon coincidence with 532-nm photons revealed that ionization thresholds occur at fluences below the plasma formation threshold[12] and thus, ion monitoring provides direct and useful evidence of the laser-matter interaction at the low fluence regime under photothermal ablation.

This chapter summarizes a series of experiments performed with the aim of uncovering the processes initiated by a sequence of two laser pulses, and to explore and understand the subthreshold processes involved in laser ionization of metallic targets. The excitation initially induced with only one sub-threshold beam is not enough to exceed the threshold for the ablation process so that no ion yield is detected solely with the pump pulse (nor the probe pulse) alone. The excitation produced by the second (probe) pulse adds to the remaining excitation from the first pulse, and may thus exceed the ablation threshold. In the latter case an ion signal is detected. This ion signal is recorded as a function of the delay time between the pump and probe pulses and contains information on the laser energy deposition dynamics. The variation of the ion yield, flight time and spectral resolution as a function of the laser interpulse delay has been checked in the interval between 0 and $100\ ns$ for different metallic targets. A clear enhancement of the ion yield corresponding to specific delays (different to zero) has been found in all cases. Although different works in time-resolved studies exhibit excellent agreement with our results and some hypothesis rose to explain this behaviour, no certainty for these hypotheses has been achieved so far.

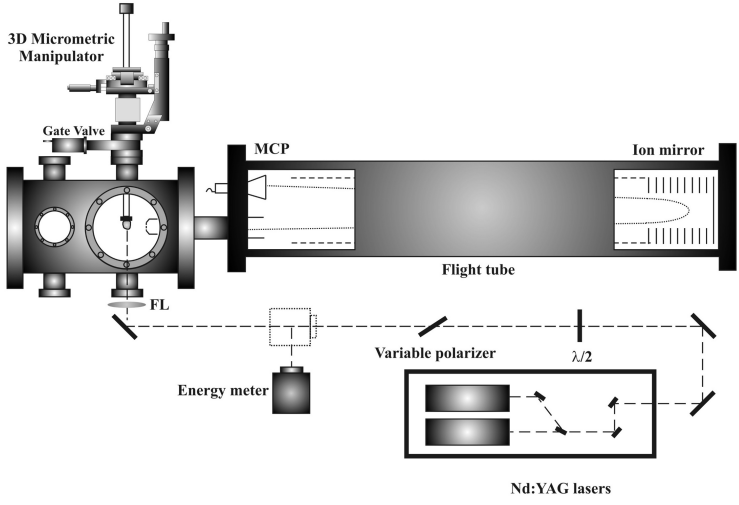

Figure 5.1: Experimental setup for this experiment. This setup corresponds with the Configuration N3, already described in Chapter 3.

5.2 Experimental

Figure 5.1 shows a schematic of the experimental setup. The detail for this experimental can be found in Chapter 3 (Configuration N3). Two identical frequency-doubled Nd:YAG lasers ($5\,ns$ FWHM pulsewidth) were focused to a sample placed inside the ionization chamber of a reflectron-based time-of-flight mass spectrometer with orthogonal extraction geometry. The ions were extracted to the flight tube and detected by a triple microchannel plate (MCP). The signal was sent to a $500\ MHz$ digital phosphor oscilloscope (DPO) to record the mass spectrum.

Despite the fact that our dual laser experimental setup (Figure 5.1, Configuration N3 in Chapter 3) has been previously described, a short briefing will be given as a reminder. Two collinear Nd:YAG lasers ($FWHM = 5ns$) were used for ionization. Our experiment demands fine control over

the laser energy of each laser and excitation timing. Each laser was externally controlled by means of independent pulse and delay generators, so that the energy per pulse of both lasers is assured to range from $30\ mJ$ to $60\ mJ$. One of the lasers (Laser 1 or master) launches the timing sequence of the experiment that can be seen in Figure 5.2. A first pulse generator (PDG-1) generates 20-Hz pulses to run the flashlamps of laser 1 (Flaslamp sync IN). At this frequency, the flashlamps are operating at their optimum frequency, avoiding thermal lensing effects in the Nd:YAG rod. After a given delay (ΔD_1 in Figure 5.2), a second TTL signal is fed into the laser 1 (Q-switch sync IN) to trigger the opening of the Pockels Cell. The energy per pulse of laser 1 is changed by modifying the values of ΔD_1. The same procedure is followed for the second laser (laser 2 or slave) using a second pulse generator (PDG-2). Similarly, the energy per pulse is controlled by modifying the ΔD_2 value. In order to assure perfect timing between both lasers, PDG-1 and PDG-2 are mutually synchronized. Under these conditions, it was possible to introduce a given delay in PDG-2 with respect to PDG-1 (Δd in Figure 5.2) to allow fine and controllable time separation between both lasers. The Δd value must be introduced in both the flashlamp and Q-switch timing sequences to keep unaffected the energies per pulse.

A fast photodiode collecting reflections from both lasers was used to check for the accuracy in the interpulse delay. A neutral density filter (optical density = 3) was placed in front of the photodiode to avoid excessive saturation that could broadened the recorded signal. The $50\ \Omega$ output of the photodiode was fed into one of the input channels of the DPO to provide direct readings of the temporal evolution of the laser beams. The result is shown in Figure 5.3 for three measurement performed at $\Delta d = 0\ ns$, $\Delta d = 10\ ns$ and $\Delta d = 20\ ns$. As shown, for $\Delta d = 0\ ns$, a single signal shows up, with a full width al half maximum of $8\ ns$, and a base-to-base width of $17\ ns$. For $\Delta d = 10\ ns$, two peaks are clearly identified, with

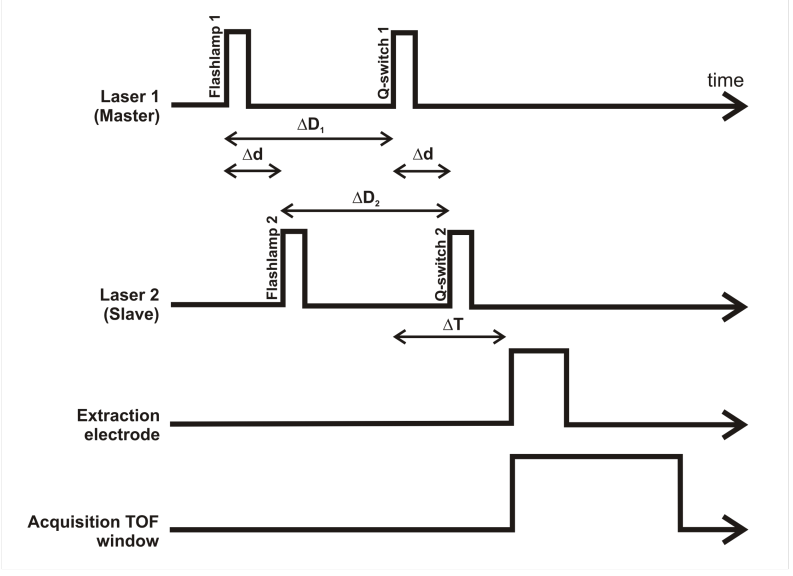

Figure 5.2: Synchronization scheme used in the pump-probe laser experiment (not to scale). Detailed explanation can be found in the text.

a time difference between maximum of $9.6\ ns$. For $\Delta d = 20\ ns$, the peaks are baseline-resolved, exhibiting FWHM of $8\ ns$, and time differences between maximum of $18.5\ ns$. The matching between the photodiode traces and the programmed values in the PDG was checked for different ΔD values up to $1\ \mu s$ although values below $100\ ns$ were used in this work. In all the situations, the synchronization did provide the right interpulse delay with complete and independent control of the energy of each laser.

Once time matching was achieved, care was taken to attain spatial overlapping of the two lasers. In our experiment, the master and slave lasers are intended to impinge the sample in the same location with 100% overlapping. As none of the lasers was expanded or filtered and they cover the same area after focussing, full overlap is difficult to achieve. After careful alignment of the optical setup, an overlapping of 75% was

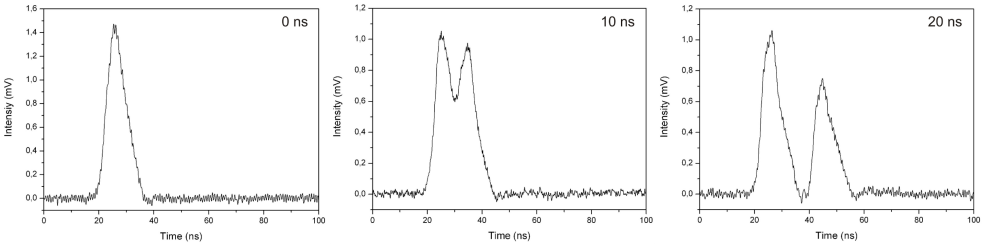

Figure 5.3: Monitoring of the interpulse delay between the pump and probe laser beams by means of a fast photodiode. The figure shows the photodiode traces for $\Delta d = 0\ ns$ (left); $\Delta d = 10\ ns$(center), and $\Delta d = 20\ ns$ (right).

attained as can be seen in Figure 5.4, where the traces obtained after 1000 double-pulse events (2000 laser pulses) in the intersected zone are clearly observed. The outer diameters for both beams are indicated in the figure with dashed lines to help the reader. Both beams were at energies below the ionization threshold. As observed in the figure, the native roughness of the sample remains in the area intersected by both beams, evidencing the soft excitation conditions with negligible mass transfer.

When temporal and spatial overlapping of the beams was achieved, the experiment was setup to allow the acquisition of mass spectra. In order to assure identical control, as large values in the ΔD may affect the spatial distribution of the incoming beams, optical attenuation of both beams was obtained by inserting non-linear optics into the beam path (details of the polarizer may be found in Chapter 3). Finally, a planoconvex ($f = 20\ cm$) lens located outside the vacuum chamber focalizes the laser beam over the sample surface. In order to allow low fluence values, the samples were located 20 mm away the focal point. Under these focal conditions, the craters profiles on the sample exhibited an average diameter of $400\ \mu m$.

A third PDG (triggered by the Q-switch signal of the master laser) was

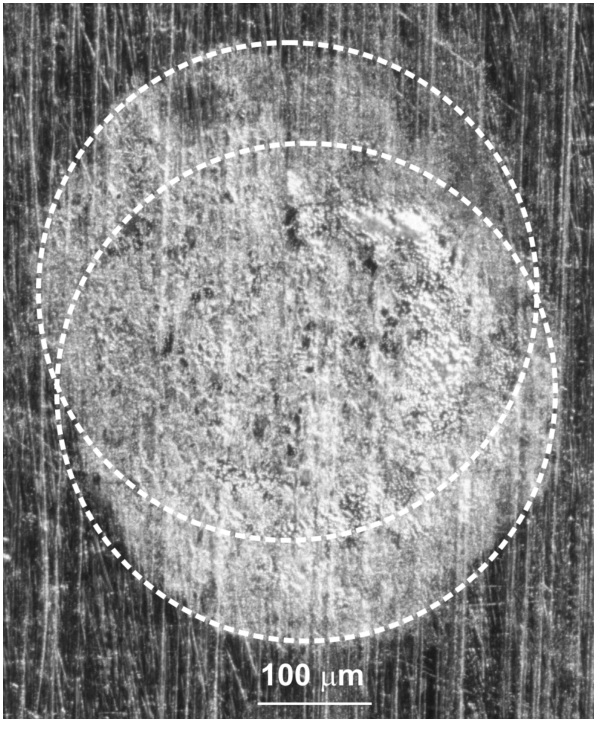

Figure 5.4: Optical micrography of the Cu sample after 1000 pump and probe laser shots (2000 laser pulses). Overlapping above 75% is attained.

in charge of providing the TTL signal to the high voltage switch connected to the repelling electrode. The repeller pulls the ions out to the flight tube by means of an electrical pulse with an amplitude of $450\ V$, a width of $1.2\mu s$, and zero delay with respect with the incoming of the master laser. The repeller pulls the ions out to the flight tube by means of an electrical pulse. After optimizing the extraction conditions, an electrical pulse with an amplitude of $450\ V$, a width of $1.2\mu s$, and zero delay with respect with the incoming of the master laser was used.

After extracting, focussing and acceleration, a triple microchannel plate detected the ions. Mass spectra were acquired for $100\mu s$ windows, al-

lowing the visualization of m/z features corresponding to all the metallic samples analyzed. The signal was sent to a DPO to record the mass spectrum.

5.2.1 Samples

Different high-purity (99.99%) foils of Cu, Ti, Si, Al, Fe, and stainless steel (AISI 314) were used. The samples were attached to the holder and introduced in the mass spectrometer. The sample to extraction lens distance was kept fixed to avoid differences in the electrical field that could affect the flight times. Typically, 50 laser shots were fired to each sample in order to remove oxides from the surface and condition the sample before analysis.

5.3 Results and Discussion

Due to the precise temporal control and spatial overlapping needed in the experiment, the experimental work was performed during three consecutive days to assure the robustness of the data provided.

5.3.1 Single Pulse Control

The single pulse ionization threshold for Cu was calculated by irradiating the samples at different laser energies. In the energy interval chosen ($0.07 - 2.00\ mJ/pulse$, equivalent to $80 - -320\ MWcm^{-2}$ or $0.40 - 1.60\ Jcm^{-2}$) there was no difference in the beam diameter that could affect the fluence determination. Series of 50 individual full time-of-flight mass spectra were recorded, and the ion signal corresponding to the $^{63}Cu^{+}$ isotope was plotted as a function of laser fluence. Data has been normalized with respect to the minimum fluence value. The plot is observed in Figure 5.5. As shown, up to a fluence of about $1.25\ Jcm^{-2}$ there is no ion

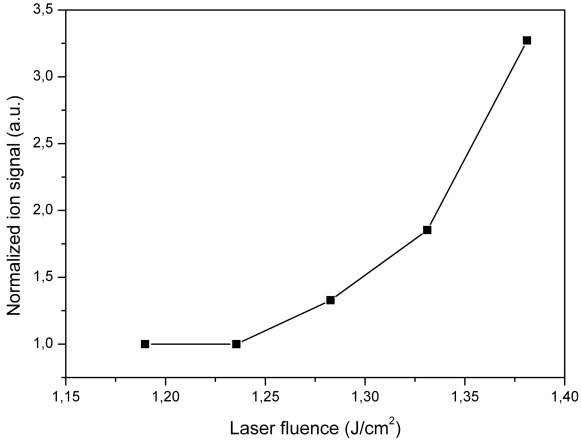

Figure 5.5: Change in the ion signal with laser fluence. Intensities have been normalized to the subthreshold values. The ionization threshold was calculated for a fluence value providing a normalized signal > 2. Each data point corresponds to a kinetic series of 50 laser pulses.

signal. After plotting the ion signal corresponding to the $^{63}Cu^{+}$ isotope as a function of laser fluence, a threshold value of $1.8\ mJ$ ($1.35\ Jcm^{-2}$) was determined.

The threshold value was taken for the fluence value providing a normalized intensity larger than 2. This criteria has been adapted from previous works in laser desorption and similar experiments.[17,18] and was also followed by authors in a previous reference.[12] For our experiment, the threshold value was $1.35\ Jcm^{-2}$. This value could be slightly lower taking a less restrictive criteria and considering the experimental restrictions of our set up that could affect the ion detection.

5.3.2 Interpulse Delay

A sounder knowledge about the mechanism leading material removal from laser-irradiated surfaces can be derived from pump-probe exper-

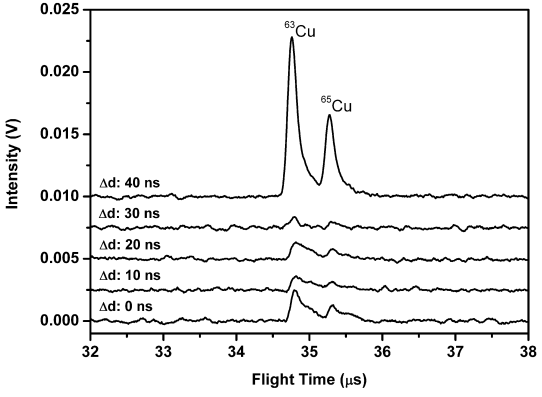

Figure 5.6: Mass spectra obtained at different interpulse delay values. Each spectra corresponds to the accumulation of 50 individual shots performed in three different sample positions. The graphs are at the same scale, with an offset introduced to help in the comparison.

iments. Such studies may allow getting detailed information on the time scale relevant for energy coupling into the target and the redistribution channels.

Once determined the ionization threshold experiment for Cu, two different collinear laser beams did irradiate the sample. Each beam was set to provide half of the energy required to reach the ionization fluence threshold (approximately $0.9mJ$, $0.7\ Jcm^{-2}$), according to the threshold fluence calculated based on Figure 5.5. Both lasers were delayed from 0 to $100\ ns$ while recording full mass spectrum. A detailed view of the mass spectra corresponding to the Cu isotopes for some of the interpulse delays from 0 to $40\ ns$ is represented in a stacked diagram in Figure 5.6. As observed, the intensity values for the $^{63}Cu^{+}$ and $^{65}Cu^{+}$ isotopes is lower than $0.002\ V$ before reaching an interpulse delay of $30\ ns$. However, at $40\ ns$, the signal reaches a value of $0.012\ V$, a 6x enhancement factor. In Fig. 5.6, the five spectra are to scale, with an offset introduced to help

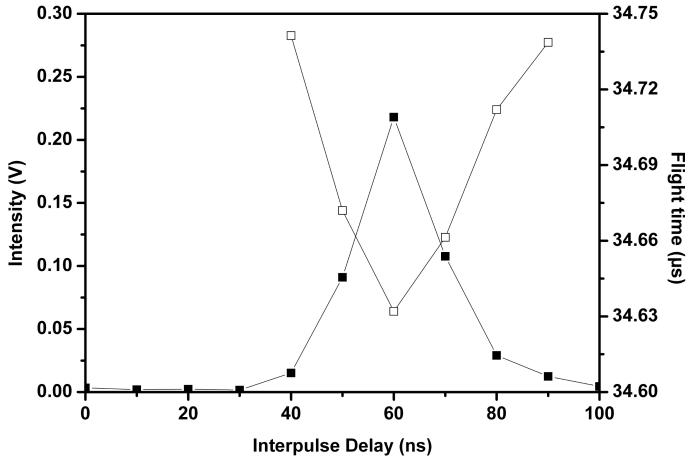

Figure 5.7: Variation of the $^{63}Cu^{+}$ ion yield (solid squares) and flight time (open squares) with the interpulse delay. See explanations in the text. Both the pump and probe lasers were set at $0.7\ mJ/pulse$.

in the visualization. Steps of $10\ ns$ were selected to avoid overlapping due to the $5\ ns$ pulse widths (FWHM) of the lasers used. The ion intensity of the $^{63}Cu^{+}$ isotope (solid squares) is plotted in Figure 5.7 for the $0-100\ ns$ interpulse delay interval. As shown, the ion yield finds its maximum ($0.220\ V$) at an interpulse delay of $60\ ns$, corresponding to a 110x enhancement factor. From this point, the ion yield decreases as the interpulse delay increases. For values larger than $100\ ns$, the ion signal dropped to zero.

For each interpulse delay, 50 double pulses were recorded, and 3 replicated measurements were performed on different fresh sample positions (Figure 5.8), to assure representativeness of the data. The interpulse delays were experimentally checked with the use of a fast photodiode with a rise time better than $1\ ns$. The spatial overlap was assured by checking the traces of both beams with burn paper at far field and by optical microscopy of the affected zone after the analysis performed.

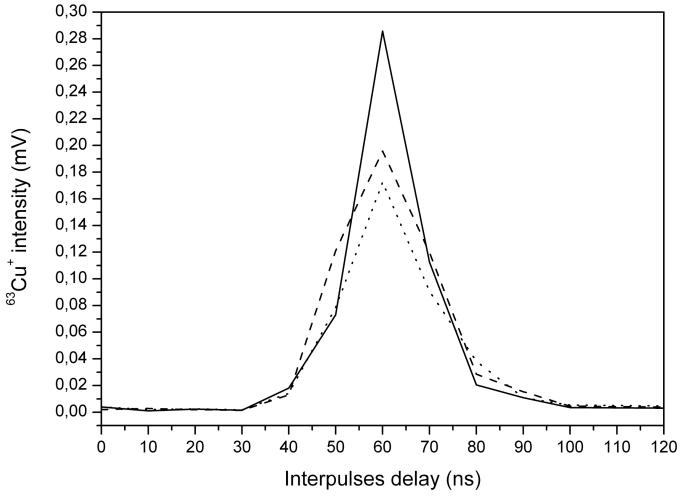

Figure 5.8: Variation of the ion signal for the $^{63}Cu^{+}$ isotope in pure metallic copper for two-laser delayed ionization. The interpulse delay is varied from 0 to $100ns$ at $10ns$ steps. Both reference and delayed beams are set at a fixed subthreshold fluence of $0.7\ Jcm^{-2}$. Each data point corresponds to the averaging of 50 measurements. The three different traces corresponding to the repetition of the measurements in differents sample locations.

The representation of the $^{63}Cu^{+}$ ion intensity as a function of the interpulse delay from 0 to 100 ns is represented in Figure 5.8 for three replicate measurements at different sample positions. The signal remains at low intensity values at interpulse delays shorter than $30\ ns$ despite of the over threshold total fluence deposited in the sample. At a delay of $40\ ns$ the ion signal quickly raises up, reaching a maximum at $60\ ns$, decaying from this point to zero at about $90\ ns$. In previous references,[18] the authors postulate an effect due to ionization of the expanding neutrals plume generated by the first laser pulse as both beams intersects. This fact may be taken into account as well. However, the $2.2\ eV$ photon energy associated to the laser beam is too low in principle, to consider

a pure multiphoton absorption process as the responsible of the phenomena observed. Recent studies in the ultrashort ablation of metals at low-medium fluence regimes[8] have demonstrated a clear increase in plasma luminiscence at $60\ ns$ after plasma firing. A first less intense maximum at $20\ ns$ also accurs. The authors assume that this delayed event is the evidence of the sequential thermal ablation process, where nucleation and following ejection of vapour and droplets occurs. The stronger plasma emission at $60\ ns$ after the ablation pulse supports the assumption of a higher temperature stage of the ablation that could explain our ionization enhancement.

Figure 5.9 shows the dramatic effect that the interpulse delay has over the mass spectra. Four mass spectra corresponding to the different ionization situations have been plotted: laser 1 only (Fig. 5.9A); laser 2 only (Fig. 5.9B); lasers 1 and 2 fired simultaneously (Fig. 5.9C); and lasers 1 and 2 fired with a interpulse delay of $60\ ns$ (Fig. 5.9D). In all the situations, the laser beams were set to provide a subthreshold fluence of $0.7\ Jcm^{-2}$. As expected, each independent laser does not provide any measurable signal. Surprisingly, when both lasers were fired simultaneously (an identical situation to the one generated by a single laser operating at $1.40\ Jcm^{-2}$) the signal was small. This situation remains up to an interpulse delay of $30\ ns$ where the signal starts to increase dramatically, reaching a maximum at an interpulse delay of $60\ ns$. As observed in the plot, a 50x enhancement in the $^{63}Cu^{+}$ is attained. Similar results have been described for time-delayed two-lasers desorption/ionization (MALDI) of molecules, [18,19] where a maximum in the ion intensity occurs in the range of a few nanoseconds. The explanation for this specific temporal event is not clear as the literature on time-resolved ionization is mainly focussed on MALDI or ionization of organics.

The results demonstrating the existence of a maximum at specific delay time shows evident similarities with experiments in laser desorption

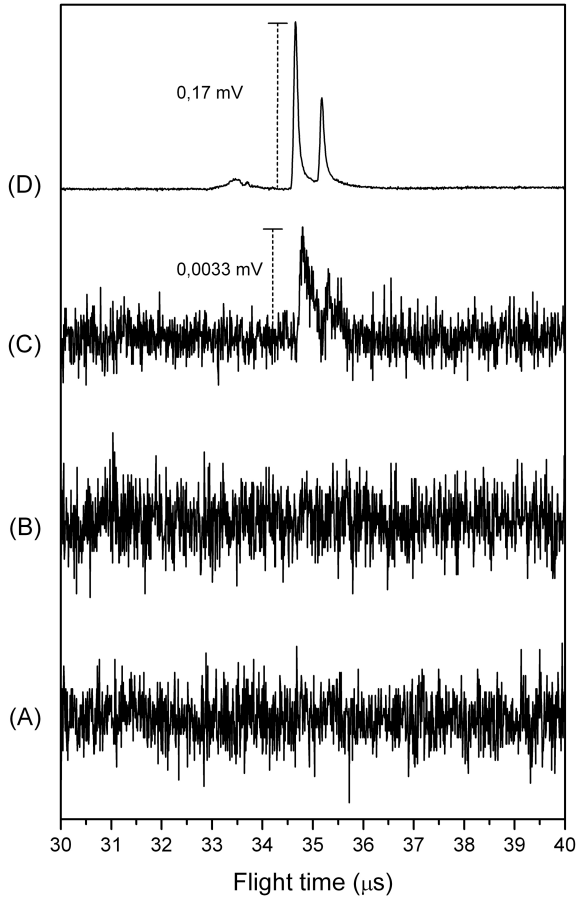

Figure 5.9: Two-pulse mass spectra using the reference (A) and delayed (B) pulses alone and both pulses together with no interpulse delay (C) and an interpulse delay of 60 ns (D). The laser beams were set to provide a subthreshold fluence of $0.7\ Jcm^{-2}$. The flight time selected allows the observation of the $^{63}Cu^{+}$ and $^{65}Cu^{+}$ isotopes. The four plots are at their maximum scale.

of organic matrices using pump-probe experiments.[18–20] There are some differences in the timescale where the maximum ion yield takes place, that could be explained considering the differences in desorption mechanism and ionization threshold for organic matrices. Furthermore, there is a good body of knowledge from many researchers interested in the dynamic of heat flow and plasma explosion mechanism[8, 15, 21] that agree with our results. Experiments performing measurements of the laser light transmission through the laser-affected area on Ni foils demonstrated that below $5.2\ Jcm^{-2}$, it took $20\ ns$ after laser firing to start sample vaporization.[21] For greater fluence values, the vaporization started earlier as a consequence of the transformation of the ablation process into phase explosion with the subsequence ejection of droplets that scattered the laser light. These studies are in good agreement with studies focussed on the heat flow and plasma explosion mechanism derived from the laser-matter interaction studied by time-resolved shadowgraphy.[15]

These authors have provided visual evidence for time scale by which nanosecond laser-induced phase explosion proceeds in aluminium. At plasma formation subthreshold fluences ($< 5Jcm^{-2}$), the images show the formation of the shock wave, starting $40\ ns$ after the arrival of a 3-ns laser pulse. As observed, the temporal scales of the commented experiments are in good agreement with our results when performed on metals despite of the slightly higher fluence values used in comparison with our work. The explanation for the timescale of our ionization feature could be in accordance with the residence time of the melted surface layer under the fluence conditions of our experiments. Time-resolved reflectivity experiments[22] might help to determine the temporal length of the melted layer and correlate it with the timescale of the ionization process.

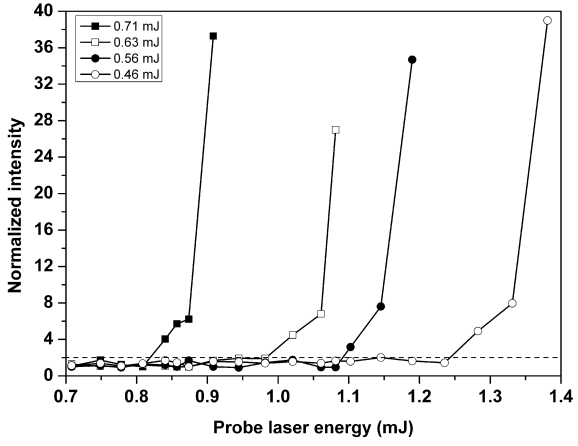

Figure 5.10: Determination of the ionization thresholds for the $^{63}Cu^{+}$ at different pump and probe laser energies. Pump laser was fixed at four different energies: 0.71 mJ (solid squares); 0.63 mJ (open squares); 0.56 mJ (solid circles); 0.46 mJ (open circles). The ion signals have been normalized for better comparison.

5.3.3 First Pulse Influence

In order to understand if (and how) the material remembers that it has been previously treated by the pump pulse, an experiment was performed at different subthreshold energies in the pump laser (from 0.46 to $0.71 mJ/pulse$). This experiment checked the relative effect of each individual laser beam in the time-delayed ionization. A delay of $60\ ns$ is chosen to get the maximum ion enhancement. At each laser energy value, the probe laser energy was gradually increased in the range between 0.7 and 1.4 mJ/pulse at an interpulse delay of $60\ ns$. The results, represented in Figure 5.10 show the variation in the ion yield for the $^{63}Cu^{+}$. The data sets are presented normalized to the signal at the lower energy for better comparison. Taking as criteria that ionization occurs at a laser energy corresponding to a normalized intensity of 2, the probe laser energy values where ionization starts are: $0.83\ mJ$, $0.98\ mJ$, $1.1\ mJ$ and $1.25\ mJ$,

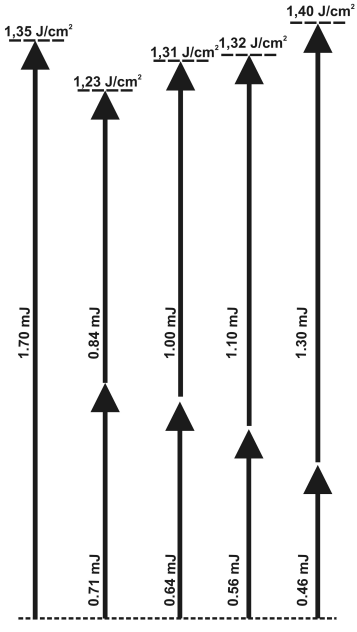

Figure 5.11: Effect of the relative energy of the reference and delayed beams in the two pulse laser ionization experiments. The diagram shows (at scale) the pulse energies in the four experiments performed. The value on top of each serie is the determined ionization threshold using the sum of the energies of both beams.

respectively. The total amount of energy required for the sample ionization in the four data sets is $1.54\,mJ$, $1.61\,mJ$, $1.66\,mJ$ and $1.73\,mJ$, slightly lower than the $1.8\,mJ$ required in the case of single laser ionization. The results are summarized in Figure 5.11. For comparative purposes, the fluence value for the single-laser experiment has been added.

Several conclusions may be extracted from the results. Firstly, the ionization fluence threshold is higher as the energy in the first laser decreases. If the first laser is under subthreshold ionization conditions, it may induce heating or melting in the sample as long as it reaches the corresponding enthalpies. Following a thermal model for the ionization

process, the role of the second laser is the generation of ions, as the solid-to-melted transition energy demands have been fulfilled by the first laser. As long as the first laser reduces its energy, the sample may not be efficiently melted and so, the second laser will have to use a fraction of its energy in performing this task. Knochenmuss and Vertes[19] have already stated for MALDI that ion formation is most efficient when a previous laser beam energizes the sample (by absorption in this case) and the second laser impinges a dense but not solid material and, thus, these results seems to be in accordance with a thermal ionization model where a minimum amount of energy is required to fulfil the enthalpies involved in the ionization process. In our experiments, the pump laser energy is enough to heat the sample, but not to ionize it. The subsequent probe laser provides the lattice with the excess of energy required for ionization. As long as the pump laser reduces its energy, the sample may not be efficiently heated and so, the second laser will have to use a fraction of its energy in performing this task. The leading pulse generates a molten layer of thickness comparable to the penetration depth of the laser light, so that the second pulse is absorbed under favourable conditions. This statement is in agreement with the key importance that other authors[8] gives to the melt layer that propagates into the material during the laser pulse in the ablation process.

5.3.4 Influence on TOF and FWHM

The results in Figure 5.7 evidence another interesting experimental fact: the enhanced intensity brings a concomitant decrease in the flight times of Cu isotopes. As observed (open squares in Figure 5.7), a minimum in the flight time occurs exactly at $\Delta d = 60\ ns$ while at lower and upper interpulse delay values the flight time shifts to larger values. The shifting interval in the flight time (around $100\ ns$) is one order of magni-

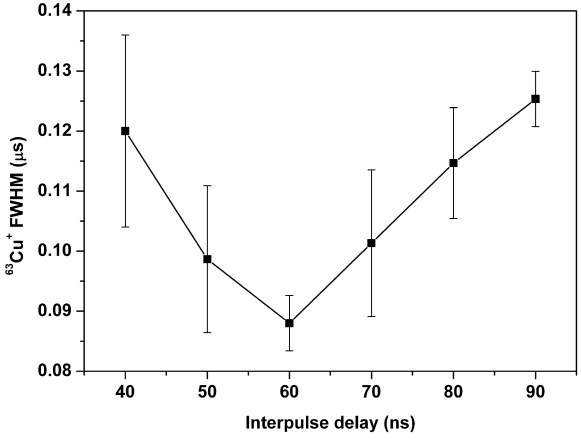

Figure 5.12: Determination of the ionization thresholds for the 63Cu+ at different pump and probe laser energies. Pump laser was fixed at four different energies: 0.71 mJ (solid squares); 0.63 mJ (open squares); 0.56 mJ (solid circles); 0.46 mJ (open circles). The ion signals have been normalized for better comparison.

tude larger than the shot-to-shot variations in the flight time, ruling out the possibility of an instrumental artefact. As the conditions in the mass spectrometer were fixed in all the experiments performed, variations in the flight time can neither be explained due to variations in the extracting field. The flight time corresponding to the $^{63}Cu^{+}$ signal in the single-pulse ionization mode corresponds to the value obtained at $\Delta d = 60\,ns$ in the delayed two-pulse experiment. Variation of the time-of-flight when ablating layered samples[23] have been explained based on modifications in the ablation rate due to the dissimilarities between materials and its influence on the effective extraction field for the generated ions. However, in our experiment there is no modification in the laser energy, sample type or extraction conditions. So, the flight time variation should be attributed to different escape velocities or kinetic energy distribution of the ions from the sample surface. Additionally, the full width at half

maximum (FWHM) of the $^{63}Cu^{+}$ peak was also studied as a function of the interpulse delay to determine the possibility of space-charge or kinetic energy effects derived from the interaction between both beams (Figure 5.12). For each point, the error bar represents the standard deviation for five replicated measurements at different sample locations. As observed in the figure, the $^{63}Cu^{+}$ peak gets its lower FWHM at an interpulse value of $60\ ns$, increasing symmetrically from this minimum point. In TOF-MS, the peak widths are limited by several factors including the spatial distribution of the ionization region in the direction of the flight tube; the initial kinetic energy distribution of the ions in this same direction; the temporal profile of the ionization source, that is, the laser pulse duration; and the bandwidth of the signal processing electronics. After fixing the laser source and the electronics, and taking into account the collinear geometry of the lasers, the most plausible explanation relies again on a modification in the kinetic energy of the ions produced. However, previous studies performed on Au ionization under near-threshold conditions indicate that there is no sharp discontinuity in the translational energy of the plume as the fluence is increased to the point of a strong plasma regime.[24]

5.3.5 Tests on different solid materials

The experiments were also performed using different targets (Si, Al, Ti, Fe and AISI 314 stainless steel) in order to check for the universality of the process and the possible variations due to sample properties.

The results for the $^{27}Al^{+}$, $^{28}Si^{+}$, $^{48}Ti^{+}$ as a function of the interpulse delay in the $0-100\ ns$ scale are shown in Figure 5.13. In all the situations, the effect of the interpulse delay was observed with small differences in the value where the maximum was located (typically between 40 and $60\ ns$) and some differences in the shape of the curve. As in Cu, the maxi-

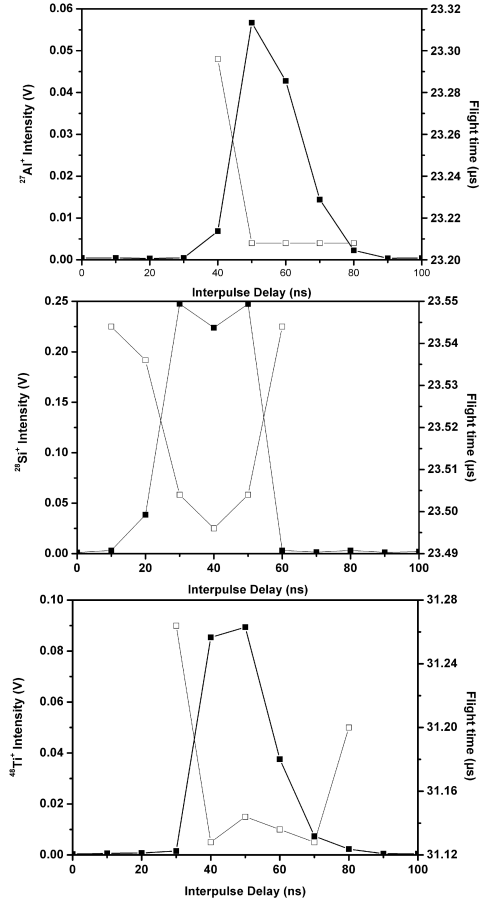

Figure 5.13: Variation of the ion yield (solid squares) and flight time (open squares) with the interpulse delay for ^{27}Al (top), ^{28}Si (middle), and ^{48}Ti (bottom). Both the pump and probe lasers were set at 0.7 mJ/pulse.

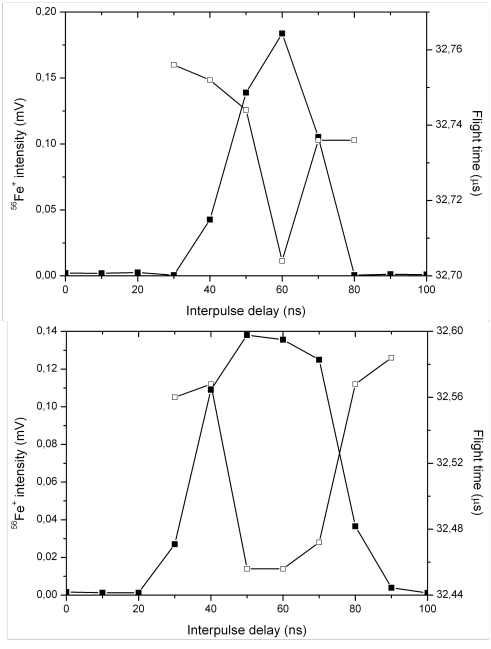

Figure 5.14: Variation of the ion yield (solid squares) and flight time (open squares) with the interpulse delay for ^{56}Fe in a 99.99% pure foil (top) or in AISI 314 stainless steel (bottom). Both the pump and probe lasers were set at $0.7\ mJ/pulse$.

mum in the ion yield coincides with the minimum flight time for the monitored ion in each case. The samples used cover a broad range of melting temperatures ($933--1941\ K$); boiling temperatures ($2792--3560\ K$) and thermal conductivities ($22\ --\ -400\ Wcm^{-1}K^{-1}$) without any clear trend that could relate thermal properties with the observed behaviour. Figure 5.14 shows the effect for $^{56}Fe^{+}$ as pure foil and in the stainless steel sample. As observed, the temporal feature seems to be affected by the matrix, although the extension of this fact to different ions and matrices has not been yet performed.

5.4 Conclusions

Time-delayed two-pulse laser ionization results are reported for a series of solid targets (Al, Cu, Fe, Si, Ti, and an AISI 314 stainless steel). A pump-probe experiment using two frequency-doubled Nd:YAG lasers collinearly aligned operating under ionization threshold fluences has demonstrated the existence of an optimum interpulse delay where a maximum ion yield occurs. This maximum occurs when an interpulse delay of $60\ ns$ is used. Concomitantly, it exist a decrease in the flight times for the monitored ions that reaches a minimum in coincidence with the maximum in the matches the ion yield (this effect also reported for the whole series of samples).

The data shows that ion signals comparable to those in single ionization can be performed by decoupling the total ionization energy in two independent delayed laser beams. Both independent lasers operate at fluences below the ionization threshold. This temporal evolution seems to be in accordance with the sequence of events that takes place during laser-matter interaction. We guess that the effect may be related to sample changes (roughness, temperature, among others), as a consequence of the the first laser pulse reaching the sample. These changes may modify the way the energy of the second laser pulse is absorbed and may also modify how the second laser pulse may get coupled with this excited solid. The duration of this modification may vary from one material to another and that fact may help us to understand the differences observed in optimum delay among the materials. The results are promising and provide some insight about how the energy provided by the laser photons is used in the solid. However, additional experiments, particularly those involving excitation with different photon energies, need to be carried out to demonstrate this hypothesis from experimental data.

Chapter 6

Modulated Extraction Conditions for LIMS analysis of DNT

6.1 Introduction

Direct laser ionization mass spectrometry represents a happy marriage where any ion generated as a consequence of the interaction of the laser beam with the solid sample will be detected.[1,2] The capability of MALDI to perform fragment-free desorption and ionization of molecules has represented a well-known scientific revolution.[3] However, the direct (matrix-free) laser-based desorption techniques are also of interest due to their universality and analytical power. Regardless the type of technique used, the common factor is the need of transforming the sample in condensed phase into detectable ions in gas phase making it a dauntingly complex phenomenon that suffer from interdisciplinary niche status (neither mainstream chemistry nor physics) and demands to be fully understood by diverse approaches different that the simple generation of mass spectra under a variety of experimental conditions.[4,5]

The analysis of energetic compounds has been always an important task due to the interesting chemistry associated to their high internal energy.[6] Thermal decomposition chemistry is fundamentally important in the explosives field, and the determination of the kinetics and mechanism of the thermal decomposition remains a fundamental aspect of their characterization. Laser ionization of many explosives and explosive-related compounds (ERCs) has been studied using nanosecond laser pulses in both vapour and solid state.[7] This method allows the rapid screening of many samples without the need of complicated preparation techniques.[8] An example is the fragmentation pathways of nitrobenzene and nitrotoluene isomers that have recently been discussed by nanosecond UV laser studies.[9, 10]

The detection of nitro-containing compounds presents serious difficulties because of the very high vapour pressures and instability of these compounds. Laser-based mass spectrometry have probed itself to be rather versatile in the characterization of these families of compounds.[11] Moreover, the use of mass spectrometry in studies of the products of decomposition and detonation of explosives has been of considerable importance for forensic chemistry, as it helped to understand the chemical fragmentation pathways which lead to the dissociation of the parent molecules.[7, 9] In this way, several underlying phenomena in the energetics of ignition and combustion of energetic materials are susceptible to a focused and coordinate research assault based on mass spectrometry.

2,6 DNT (or o-DNT) is precursor for trinitrotoluene (TNT), one of the most powerful energetic materials. There are no natural sources of DNT, which is manufactured by nitration of toluene, producing a mixture of 2,4-DNT ($\tilde{8}0\%$), 2,6-DNT and small quantities of the other four DNT isomers. Small quantities of the DNT isomers are also produced as by-products in the manufacturing of 2,4,6-TNT.[12] 2,6-DNT is less powerful than TNT, and dos not produce as much NO as TNT does, what has limited the num-

ber of analytically-oriented work using it. However, its chemical structure (due to the orto geometry of its NO_2 groups) is quite similar to TNT, turning it an excellent model to study its direct laser desorption and the energetic channels involved in its decomposition. As it happens in TNT, the NO_2 groups in positions 2 and 6 in 2,6-DNT are twisted out of the plane due to the inductive, resonance and steric effects between them, assuming a non-planar position with respect to the phenyl ring. This fact decreases the conjugation to the phenyl ring and its stability with respect to the almost coplanar 2,4-DNT.[13] In the present work, LI-ToFMS is used to investigate the fragmentation induced by a 5-ns pulse width Nd:YAG laser at 266 nm on pellets of 2,6-DNT. The recording of full range mass spectra at increased controlled fluences allows the establishment of the ionization threshold for the different desorbed ions of the molecule and a deeper understanding about the energetic channels taking place and possible fragmentation pathways. In principle, thermal effects are expected to play a major role in molecular-ion formation, as the possibility of photochemical effects derived from non-resonant two-photon absorption is limited as the ionization potential of the 2,6-DNT ($9.8\ eV$) [14] can not be reached by absorption of two 266-nm photons ($9.30\ eV$).

In the experiments described in this chapter, laser-ionization time-of-flight mass spectrometry in reflectron mode is used to investigate the fragmentation induced by a 5-nanosecond laser at $266\ nm$ on a nitroderivate of toluene (2,6-dinitrotoluene). Experiments show that using a fine control on the pulsed extraction conditions (including delay and electrical pulse width) it is possible to tailor the atomic or molecular information required. This control may be done in real time, making it possible to get atomic and molecular information, for a given sample, within seconds. This feature is not offered by similar techniques already mentioned, as the energy dose required by those techniques is either too

small to get atomic information or too high to get the molecular fragments. This puts LIMS in a preferred situation for the rapid analysis of low molecular weight organic compounds, specially when we need to perform both atomic and molecular analysis.

6.2 Experimental

Details on the instrument can be found elsewhere.[5,15] System uses a configuration that we have described as System Configuration N4, previously detailed in Section 3.3.4. Figure 3.22 sketches the most relevant elements of the instrument. Briefly, a pulsed Nd:YAG ($5ns$, $266nm$) laser is used as ionization source. The flashlamp voltage and delay in the Pockels cell were set to their optimum value, providing maximum shot-to-shot stability. Laser pulse energy was controlled using a variable attenuator that allows continuous variation of the energy per pulse without modifications in the beam spatial profile. The energy per pulse was continuously varied between $0.3\ mJ$ and $8\ mJ$.Care was taken to avoid excess of energy that could induce beam shielding.[16] The target is placed inside an ionization chamber connected to the flight-tube. Laser is focused on the sample at normal incidence, and the generated ions are orthogonally extracted into the flight-tube. The detector output fed a 500-MHz Digital Phosphor Oscilloscope, controlled externally by home designed software. Kinetic series of 200 mass spectra (associated to 200 laser events) were acquired for every data point. Care was taken to record all the spectra under identical laser excitation and focusing conditions.

6.2.1 Samples

The sample (purchased from *Sigma-Aldrich* in the form of a yellowish powder with a purity of 98% was grinded in an agate mortar to reduce

the grain size and facilitate subsequent pelleting. Non especial drying is required before grinding, as long as the sample is kept in a relatively dry and fresh environment. Pellets of $2\ mm$ thickness and $10\ mm$ in diameter were done by weighting $0.4\ g$ of 2,6-DNT and pressing it at $2\ atm$ for 15 minutes. Due to the high vapour pressure of the 2,6 DNT, the pressure in the ionization chamber could not be lower than $2.5\ x\ 10^{-4}\ mbar$, and the pellet had a lifetime of about 30 minutes before complete vaporization. The analysis was performed thanks to the differential pumping that kept the detector below $10^{-6}\ mbar$ during data acquisition.

6.3 Results

Initial experiments were performed to establish a set of experimental conditions yielding suitable resolution and signal intensity. Several laser wavelengths from the *Nd:YAG* laser (1064, 532 and 266 nm) were checked in a wide range of energies per pulse. The thermal effects associated to the IR output did impair the recording of mass spectra with molecular information due to extensive fragmentation. The 532-nm output generated spectra with richer information, although still affected by extensive fragmentation. Thus, the UV output was finally selected.

The onset of ion generation for 2,6 DNT (ionization threshold) was determined by increasing the energy per pulse reaching the sample while monitoring full-range mass spectra. The procedure has been previously described in detail.[4, 17] Due to the use of an optical attenuator, the spatial profile of the laser beam was not modified regardless the energy output. The experiment was performed starting from energy per pulse providing no ion signal in our TOFMS system ($0.2\ mJ/pulse$). The energy was raised progressively to a maximum of $8\ mJ/pulse$. For each new energy setting, the entrance of the laser beam was blocked, and 100 consecutive shots were monitored to determine the average energy per

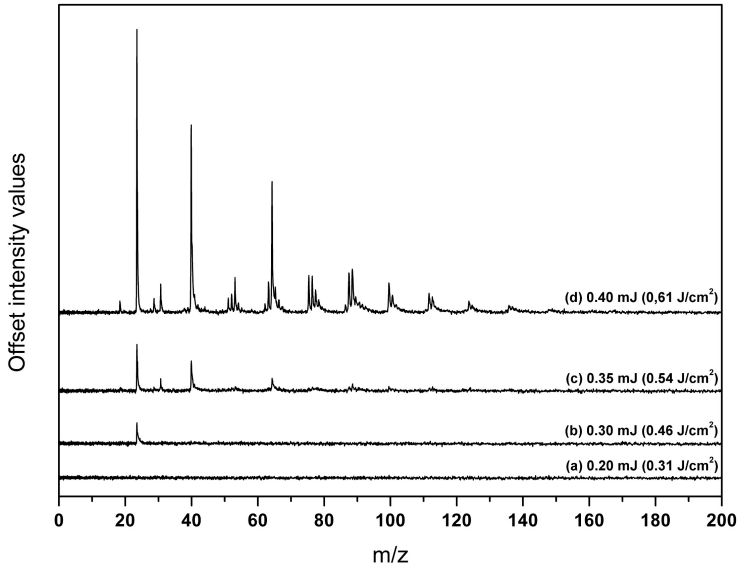

Figure 6.1: Mass spectra ($0 - 200\ amu$ range) of 2,6-DNT obtained at different laser energies in the threshold range. The extraction pulse width was set to $800ns$ in these experiments. Each data set is represented at its maximum intensity, with an offset introduced to help in the comparison.

pulse and the relative standard deviation (RSD) of the data. In the studied range, RSD values lower than 1% were obtained. The laser diameter at the sample surface was determined by irradiating a *Cu* planchette and measuring the affected area with an optical microscope. Due to the low energy per pulse, overestimation of the laser spot due to heating effects was discharged. The resultant beam diameter was $280\ \mu m$, corresponding to an area of $6.15x10^{-4}\ cm^2$.

Figure 6.1 shows the changes in the recorded mass spectrum when the energy per pulse is sufficient to provide measurable ion signal. As observed in the figure, early ion signal (corresponding to the surface desorption of $^{23}Na+$) demands a minimum energy per pulse of $0.30\ mJ$ ($0.49\ Jcm^{-2}$). From $0.35mJ/pulse$ ($0.57\ Jcm^{-2}$), apart from the ubiquitous

$^{23}Na+$ signal, incipient ion signals corresponding to molecular fragments as $^{30}NO+$, and signals at $m/z = 39, 63, 77$ corresponding to $[C_nH_m]^+$ hydrocarbon radicals are observed.[18–20] The low-mass ions series for aromatic compounds are not restricted to specific m/z values, but they are nonetheless consistent enough to be useful for identification of aromatic compounds.[21] The origin of these fragments can be both fragments from the 2,6-DNT or any aromatic residue in the compound. Increasing the energy to $0.40\ mJ/pulse$ ($0.65\ Jcm^{-2}$), a well-resolved mass spectrum is observable with information in the high mass range. As in related references [6, 8, 9, 11, 22], our spectra does not show signals associated to $^{46}NO_2$. This fact it is due to the short lifetime of the intermediate states involved in the generation of NO_2^+ (a few hundred femtoseconds), that leads a to rapid dissociation to generate the most stable NO^+ ion.[22]

Additional energy per pulse is required to generate the molecular peak, as it may be observed in Figure 6.2 for the different mass spectrum recorded at selected energies per pulse covering values up to $7\ mJ/pulse$ It is quite obvious the richer mass information obtained with increasing the energy per pulse. However, a higher fragmentation, visible as contributions at $m/z < 20$, it is also occurring. Due to the balance between sensitivity, full mass-range information and fragmentation, a value of $1.3\ mJ/pulse$ was taken for further experiments.

Figure 6.3 shows the threshold for specific evolution of specific *m/z* with increasing energy per pulse for $^{12}C^+$, $^{30}NO^+$, $^{63}C_5H_5^+$ and $^{148}[M - 2OH]^+$. It is quite clear the presence of $^{30}NO^+$, $^{63}C_5H_3^+$ and $^{148}(M - 2OH)^+$ at low energies per pulse, experimenting the four peaks a sudden intensity increase at about $0.75mJ/pulse$. From this point, different behaviour is observed. The $^{148}[M - 2OH]^+$ fragment exhibits a maximum around $1.3\ mJ/pulse$, decreasing quite sharply its intensity, reaching zero at about $3\ mJ/pulse$ The same behaviour was found for the $^{165}[M - OH]^+$

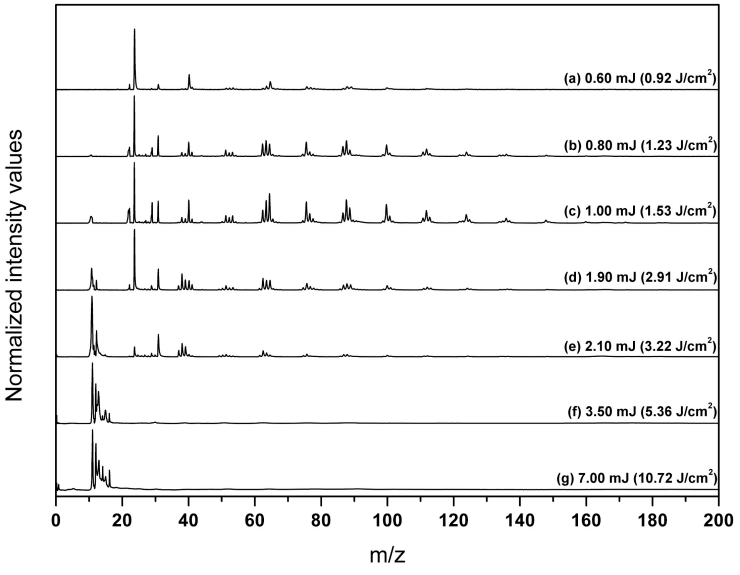

Figure 6.2: Mass spectra ($0 - 200\ amu$ range) of 2,6-DNT obtained at different laser energies from $0.5mJ$ to $8mJ$. The extraction pulse width was set to $800ns$ in these experiments. Each data set is represented at its maximum intensity, with an offset introduced to help in the comparison.

fragment. The $^{30}NO^{+}$ signal increases up to $2.20\ mJ/pulse$, dropping afterwards.

The complexity of ionization from condensed phase in comparison with gas-phase is evidenced when the ionization order was determined. A characterization of the ionization behaviour may be easily done by plotting the ion signal versus the laser energy per pulse. In this way, it is possible to determine the ionization order, *n*, defined by:

$$I_m^+ = \alpha(P)^n \tag{6.1}$$

where I_m^+ denotes the intensity of the ion signal of mass m, and P denotes the power density (or energy) of the laser pulse. The value of n is determined based on the slope of the $lg(I_m^+)$ vs. $lg(P)$. In the absence of

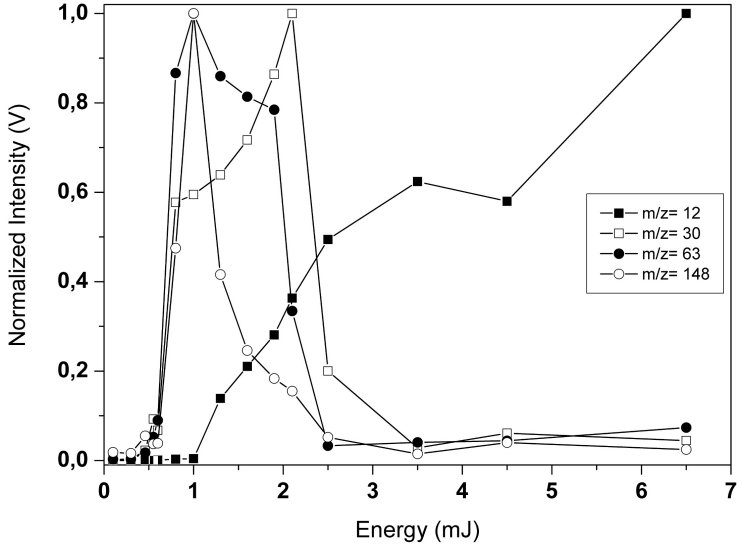

Figure 6.3: Mass spectra (Dependence of the ion signal with laser energy per pulse for $^{12}C^{+}$, $^{30}NO^{+}$, $^{63}C_5H_5^{+}$ and $^{148}[M-2OH]^{+}$ ion fragments.

saturation effects the slope represents the number of photons required for the ionization process. The calculations performed for the different mass fragments in Figure 6.3 yielded values of between 4 and 6, evidencing an ionization channel other than photon absorption. The possibility of a $1+1$ photon absorption through a very high excited state after the absorption of the first photon is ruled out, as the gas phase photoionization of the sample did not yield any signal. It is interesting to note in Figure 6.3 that all the plots modify their trends at about $1\ mJ/pulse$. Depending on the monitored ion, this cut-off value corresponds to a change in the slope (as in $m/z = 63$), the onset of ion generation ($m/z = 12$) or the starting of the ion extinction ($m/z = 163$). The fact that the ^{12}C signal (evidencing full fragmentation of chain fragments) starts at this cut-off value supports the idea of a change in the ablation mechanism corresponding to Coulomb explosion.

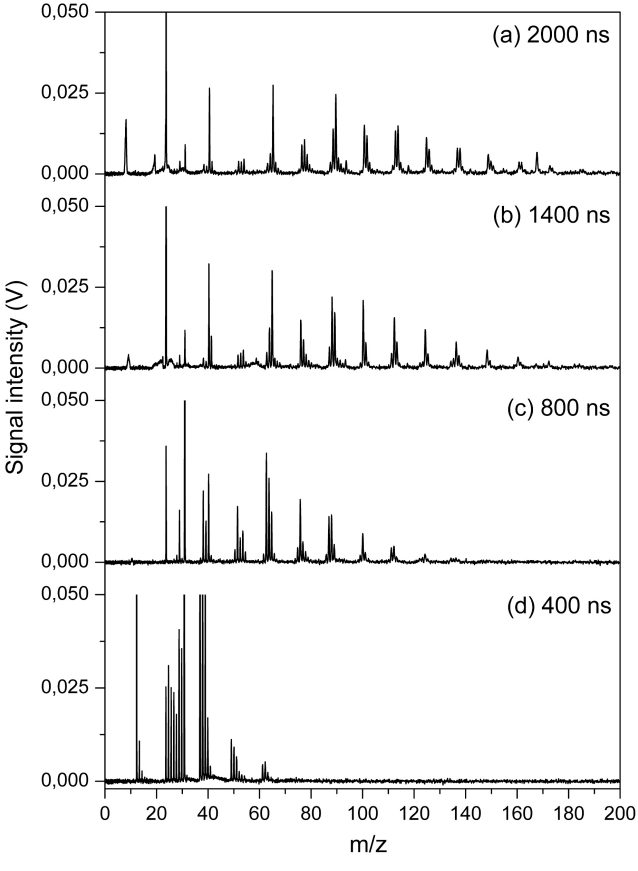

Figure 6.4: Mass spectra of 2,6-DNT at an energy per pulse of $1.3\ mJ/pulse$ under different extraction widths conditions. The extraction delay was set at $0\ ns$.

The orthogonal extraction geometry used in our experiment allows a decupling of the initial kinetic energy of the ions due to their escape velocities from the solid and the one provided by the extracting field. Even under near threshold conditions, the kinetic energy and spread of the ions is large once Coulomb explosion occurs. Thus, the pulse amplitude, length and delay with respect to the laser incidence are important parameters to account in orthogonal extraction that can modify quite dramatically the signal intensity of the detected ions. In our experiments, it was observed that the ion yield decreased significantly as soon as delays larger than $100\ ns$ were introduced. No attempts were done to modify the geometry of the extraction lens with respect to the sample. Thus, the zero delay condition was kept for all the experiments. The amplitude of the extraction voltage was very sensitive up to a given voltage where the signal reached a plateau that was selected as optimum extraction amplitude. The most significant effect was observed in the pulse width. Figure 6.4 shows the full mass spectrum at increasing pulse widths from $400\ ns$ to $2000\ ns$. At the lower pulse width, the spectrum reveals exclusively atomic information, while progressive richer information at the high mass range is obtained as the extraction width is larger. This fact opens the possibility to obtain modulated atomic/molecular spectra. The explanation has not yet been found, although experiments performed with different compounds have demonstrated that the phenomena described is quite general.

Figure 6.5 shows a comparison of the spectra taken at $2000\ ns$ with the 2,6-DNT electron impact spectra from the NIST data base. As shown, the matching in the information is rather satisfactory. The direct link between the chemistry in the gas phase and the reactions taking place in the condensed phase is complex. In principle, the final mass spectrum is a convolution of the early chemistry at the time scale of the laser-mater interaction and a variety of secondary reactions that further de-

grade the parent molecule. The laser-driven ignition process and the time scale where our measurements is taking place, are a chance for secondary mechanisms to occur that will enrich the final spectrum with additional features closely related to those occurring under detonation conditions. In this sense, it is our believe that direct ionization on condensed phase coupled to time-of-flight mass spectrometry represents a remarkable tool in the sound understanding of the chemistry of high energetic materials.

6.4 Conclusions

Nanosecond time-of-flight mass spectra of 2,6-DNT have been acquired using the $5\ ns$ fourth-harmonic output from a *Nd-YAG* laser for one-step desorption/ionization. The work has demonstrated the ability of the technique to generate analyte molecular and structure-specific ions of the nitro compound (as compared with the electron impact data). The onset of the ion generation for different fragments takes place at the same laser energy ($\tilde{0}.35mJ$, $0.53Jcm^{-2}$). The opening of the aromatic ring seems to occur at higher values ($\tilde{1}.5mJ$, $2J/cm2$) where a change in the ablation regime (Coulomb explosions) occurs, as indicated by the increasing in the $^{12}C^{+}$ signal.

The mass spectra undergo important qualitative changes when extraction width pulse was varied. At short extraction widths (400 ns), it exist a cut-off for high masses, and the mass spectrum reveals atomic-only information. For longer width pulses ($> 800\ ns$), higher mass fragments are detected, while low mass ion peaks reduce their intensity and resolution. These results allow a sort of modulation based on a simple modification in the extraction settings, not in the excitation conditions, opening the possibility of acquiring quasi-simultaneous atomic/molecular modulated mass spectra.

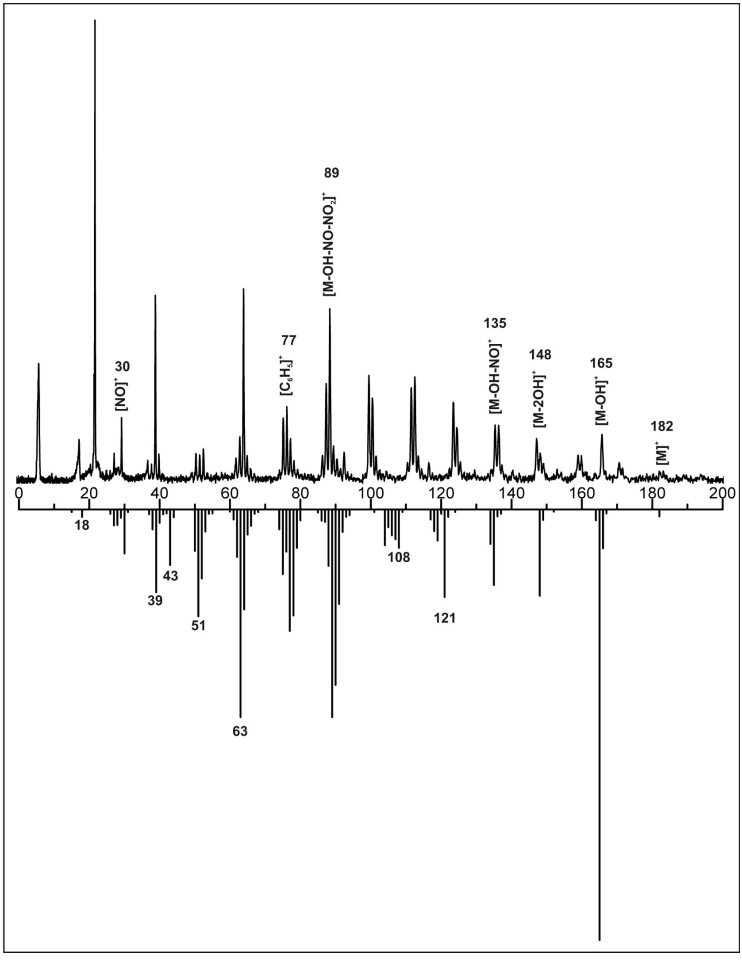

Figure 6.5: Comparative of the nanosecond TOF mass spectrum of laser desorption/ionization (top) and $70\ eV$ electron impact NIST mass spectrum (down) of 2,6-DNT. Selected spectral features have been indicated.

Chapter 7

Near-field Laser-ablation

7.1 Introduction

The Near-field effect was first applied by Ash and Nicholls to increase the resolution of optical microscopy in 1972.[1] Hence, marking the advent of a microscope capable to reach submicrometer resolution without the vacuum needed to operate both Scanning Electron Microscopy (SEM) and Transmission Electron Microscopy (TEM).

Sensitive analysis at concentrations in the ultra-trace level can be easily performed by mass spectrometry.[2] Also, localized analysis of solids by mass spectrometry can be performed if a microprobe is used for sampling. Many different probes can be used, more importantly ion probe[2, 3] or laser probe.[2, 4] The advent of femtosecond lasers increased the lateral resolution achieved with nanosecond pulses, but this resolution may still be improved if a near-field probe is used.

In this context, the development of a femtosecond laser microprobe-based technique capable of performing rapid analysis of solids with all the advantages of mass spectrometry and the added features of high lateral resolution and atmospheric pressure sampling, obtained from the near-field interface, would represent a serious advance of major inter-

est for all the industry requiring fast analysis with fine control of newly developed structured materials. The coupling of a Near-field (NF) stage with an already existing LA-ICP-MS instrument would match all the requirements.

Near-field Optics is the study of non-propagating inhomogeneous fields (evanescent fields) and their interaction with matter. Near-field-based techniques rely on the enhancement of the electric and magnetic field that occurs when a piezoelectric device is tuned at its resonance frequency near the surface of a solid. Near-field measurements are usually employed due to its ability to override the far-field limit of diffraction. This fundamental diffraction limit of resolution, also known as the Rayleigh criterion, is essentially given by the wavelength of the employed radiation λ and the numerical aperture ($nsin\theta$), as expressed in the Equation 7.1:

$$\Delta x > \frac{0.61\lambda}{nsin\theta} \tag{7.1}$$

During the last century optical microscopy has improved to the limit of the theoretical limit which was derived by Abbe in his work on diffraction and microscopic imaging.[5] Yet in the decade of 1920, Synge proposed a model to extend the optical resolution beyond the microscopic level.[6] Even though, it was back in 1932 when application of piezoelectrics to microscopy was first proposed by Synge[7] (as cited by Novotny[8]), thus sitting the basic idea for the near-field microscopy.

The idea of properly controlling the distance between the probe and the target using piezoelectrics was set by Binning et al., that was the origin of the building of the first Scanning Tunneling Microscopy (STM) in 1982.[9] First modern reports of optical near-field measurements appeared in 1984 and were performed by Dieter W. Pohl and co-workers at the IBM Research Laboratory in Rüschlikon (Zürich), Switzerland.[10] In the classic approach, such as the one developed by Pohl, SNOM uses

a waveguide with a small aperture to guide the light unto the target's surface. This aperture is designed to have a diameter smaller than the wavelength going through it.

Figure 7.1 shows the two main setups for Near-field laser-ablation. The first one (*a*) shows a laser beam being guided onto the sample's surface by a fiber optic, while the rest of the beam (not being guided by the fiber) is blocked using a metal plate. The laser being guided by the fiber may be attenuated to avoid ablation of the fiber itself (this is more likely to occur near the tip, where radiation gets confined, and even in the tip, where change of medium occurs). As a consequence, laser will be at a fluence low enough to assure that any ablation taking place is a consequence of tip enhancement. The second one (*b*) shows a sub-threshold laser beam being directly focused on the target. As this is a sub-threshold pulse, it's unable of getting laser-ablation all alone, and it's only ablating material due to the enhancement provided by the presence of the tip, and only in the area surrounding the tip. In both cases, the ablation effects gets confined into an area smaller than the one predicted by the diffraction limit.

These setups try to overcome a problem regarding any near-field ablation experiment: the assurance that laser-ablation is due to tip enhancement. To be sure that material is ablated only by means of the Near-filed probe, laser must be either shotted at a sub-threshold fluence or physically blocked so that only the laser guided by the NF-probe reaches the target. This two setups may be observed in Figure 7.1. A third setup will be similar to Fig.7.1b, but in this case the tip is placed on the other side of a thin solid. This configuration is very used in Tip-enhanced Raman Spectroscopy (TERS).[11]

Ever since the development of the Scanning Near-field Optical Microscopy (SNOM), significant efforts have been made to adapt the interesting features of this microscopy to the chemical analysis of solids,[12–

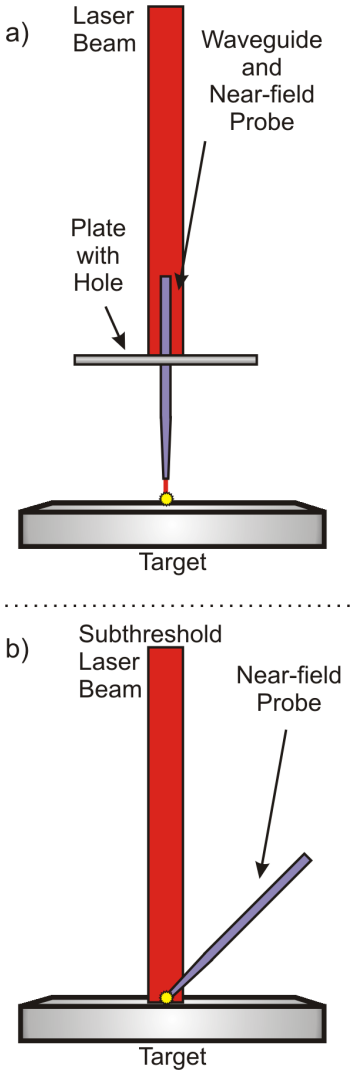

Figure 7.1: **a)** The laser beam is guided to the surface by a fiber optic. The fiber optic goes through a plate that acts as a barrier for the rest of the laser beam. **b)** A sub-threshold laser pulse is guided to the sample surface and irradiates the tip. The enhancement of the field due to the presence of the tip will provide laser ablation only in the area surrounding the tip.

14] leading its contribution one step forward than the mere characterization of a surface from an structural or microscopical point of view.

The combination of both recent advances (femtosecond lasers and Near-field probes) into one single instrument that also includes a reliable technique as ICP-MS has been tried by some authors in recent years,[12–14] as it promises to combine the less pronounced thermal effects of the femtosecond pulse (see Chapter 2) with the overriding of traditional diffraction limits for the far field due to the use of the Near-field setup. Even though advances exist,[13] full integration of the instrument and the ability to perform analysis is yet to be achieved and remains a task.

The present chapter describes experiments performed with the marked goal of pushing the capabilities of Mass Spectrometry. Firstly, analysis by Near-field ablation of solid samples performed in the laboratory as a preliminary step to perform chemical analysis of solids with extremely good lateral resolution will be treated. This work was carried out at the Institut for Analythical Sciences (ISAS, formerly known as *Institut für Spektrochemie und Angewandte Spektroskopie*) in Dortmund[15] during the summer of year 2007. The goal of this experiment is to give an answer on whether it is possible or not to perform chemical analysis (using ICP-MS analysis, in this case) of NF-ablated material by a femtosecond laser guided through an SNOM system. Superficial and localizad analysis of solids by Near-field assisted laser microprobes is a promising new area under development in the area of laser chemistry.

7.2 Experimental Setup

The full equipment required to perform this experiment comprises a femtosecond laser, a near-field scanning system, the electronics associated to the near-field probe, and the ICP-MS instrument. An schematic view

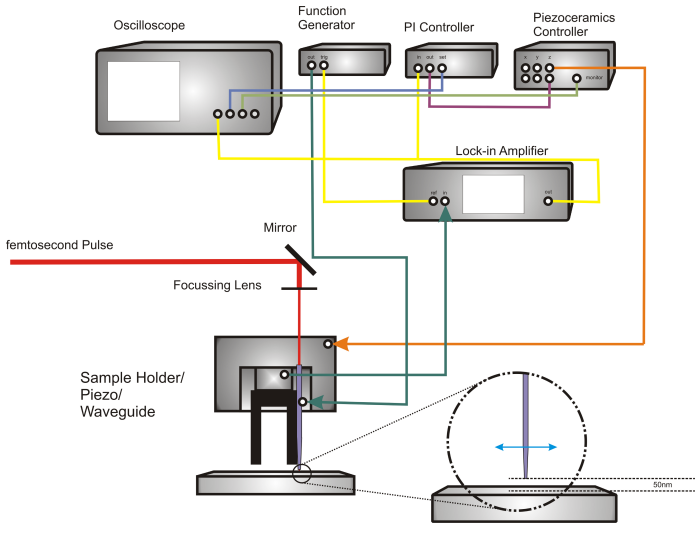

Figure 7.2: Schema control electronics needed to control the near-field stage.

of the setup can be seen in Figure 7.2. The complete set of optics to guide the laser beam to the tip and the tubings to transfer the particles to the ICP-MS are not shown for clarity.

7.2.1 Femtosecond Laser

The femtosecond laser system was a commercial system by *Spectra-Physics* (Model Hurricane). This system has the following components (see Figure 7.3):

- Ti:Sapphire. Seed laser. Model Mai Tai. Capable of giving $> 700mW$, $sub-100\ fs$ pulses at $80\ MHz$ repetition rate.
- Nd:YLF. Model Evolution. Diode-pumped Pump laser as a source for the Ti:Sapphire regenerative amplifier.
- Ti:Sapphire. Regenerative amplifier.

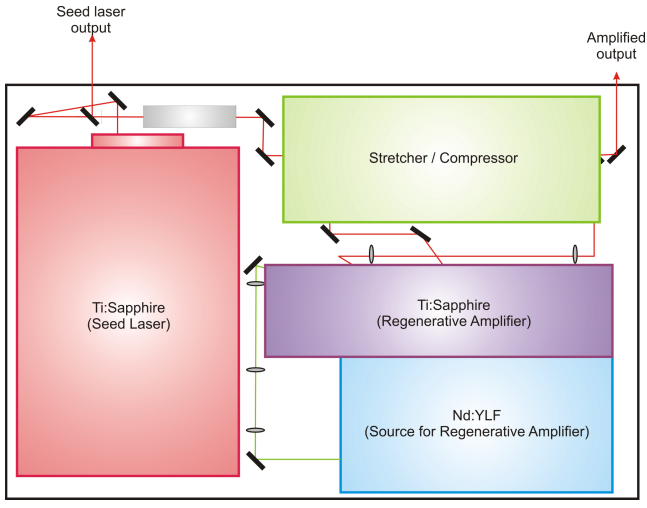

Figure 7.3: Representation of the components of the whole Hurricane femtosecond laser by Spectra-Physics, as seen from above.

- Pulse Stretcher / Compressor.

This femtosecond laser has a maximum energy greater than $0.75\ mJ$, with pulses shorter than $130\ fs$ at $1\ kHz$ of repetition rate.

7.2.2 Near-field Stage

Along with the laser (and optics) and the ICP-MS to perform chemical detection, the main part of the system is the near-field stage itself, where the laser beam and the target interact with our sample by means of a probe with a limited aperture in the nanometer range ($\theta \approx 100\ nm$) and a piezoelectric in charge of enhancing the electric and magnetic fields of the laser beam in a really localized region of the target. The distance between the sample and the tip is controlled by measuring the tunnel effect current between them. The whole list of components needed to build the system is rather similar to the ones used in SNOM, and includes:

- Oscilloscope
- Function Generator
- Proportional-Integral Controller (PI Controller)
- Piezoceramic
- Lock-in Amplifier
- Near-field probe
- Active Isolating System to prevent tip crashes

A detailed description of the operating principles of a SNOM system may be found in literature.[16] We will concentrate on the tip action and the tip manufacturing step, as part of the experimental work developed.

The oscilloscope (Tektronix^{TM}, Model *TDS 714L*) is used to monitor the near-field enhancement. In the oscilloscope the actual value and the control signal coming from the PI controller can be controlled and matched, as well as the feedback stability of the tip-crash prevention system. The function generator (Hameg^{TM}, Model *HM8130*) is used to excite the piezoceramic to its resonance frequency. The PI (Proportional-Integral) controller (developed at ISAS) uses the detector to measure the distance to the surface. This signal is monitored in real-time in the oscilloscope. Under operation, it also controls the feedback loop to regulate the NanoCube^{TM}(Physik Instrumente^{TM}, Model *611.3S*): a piezo stage with XYZ nanopositioning capabilities and a resolution as good as $1\ nm$. The lock-in amplifier (Stanford Research^{TM}, Model *SR830 DSP*) operates essentially as a tunable band pass filter whose pass band is centered at the resonance frequency of the quartz tuning fork. The near-field head, where the piezoceramic with the waveguide is placed, is made of non-conductive material, usually acrilyc polymers or Teflon. This piece was

also built at ISAS. Figure 7.4, taken from a previous work from Siegel[14] shows a photography of the near-field head, along with other elements. This head has a hole drilled so that one extreme of the fiber containing the aperture on the opposite side can go through the hole to appear on the upperside of the aluminium plate we used to stop the beam, thus, allowing for the laser light to get to the target only by means of the fiber optic. Below the near-field head, the sample holder is placed. Then, the quartz tuning fork has the fiber glued to it. The distance between the tip and the sample surface is controlled via the PI controller, so a constant oscillation time is needed and that's why the fiber with the tip is attached to a quartz piezoceramic. The fiber must be parallel to one of the tuning fork tines respect. Quartz tuning forks with a resonance frequency of 77 kHz by Comtech Crystals Ltd. are used. The near-field probe is particularly sensitive to the external interferences coming from the building. The system uses an active vibration isolation system (Halcyonics™, Model *Micro 40/60 Series*) to prevent vibration from crashing the tip on the surface or interfering the near-field enhancement behaviour.

7.2.3 Tips and Tips Etching

Figure 7.5 shows the typical laser irradiation of a target when a tip-ended fiber-optic waveguide is used to generate Near-field enhancement of the radiation effects on the target. As the aperture size of the tip will determine the size of the irradiated zone, the improvement of this aperture will be of great importance. It has been experimentally probed that the light aperture at a tip improves (smaller diameter) when the tip has a sharpened end, as this reduced aperture confines the effects of the radiation in a smaller area.[17]

Tips are etched at the end of a waveguide made from commercial fiber optic ($\phi = 25\ \mu m$) coated with acrilate, following a previous proce-

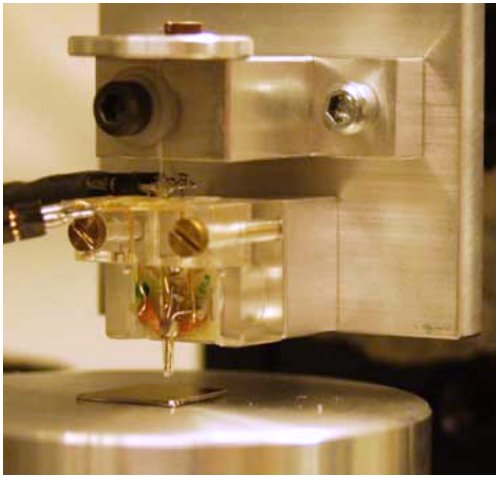

Figure 7.4: Photograph of the near-field head. The laser pulse comes from the top. The aluminium plate, the glass fiber, the acrylic near-field head, the piezoceramic and finally the probe can be observed in a top-bottom sense.

dure.[18] Preparing the fiber optic to act as a waveguide for the NSOM system requires the fiber to be etched so that it gets a sharp end. The etching of the fiber is made using a solution of fluorhidric acid (HF) in isooctane. Figure 7.6 describes this step. HF acid succesfully degrades the fiber optic, while leaving unaltered the polymer coating. It is due to this unaltered coat that the flow of the liquid gets the fiber more attacked on the edges than in the center, thus, providing a sharpened termination for the tip. This termination will act both as tip for the NSOM system and aperture to get the light out of the fiber and over the target's surface.

The fibers are left inmersed into the HF/Isooctane solution for two hours, to get the tip as sharpened as possible. While the etching step is taking place, the system needs to be absolutely isolated from vibrations, so that a proper sharpening of the fibers occurs. Without these careful considerations the near-field enhancement does not occur as the effect is not properly confined. Once the etching step has finished, the acrilate

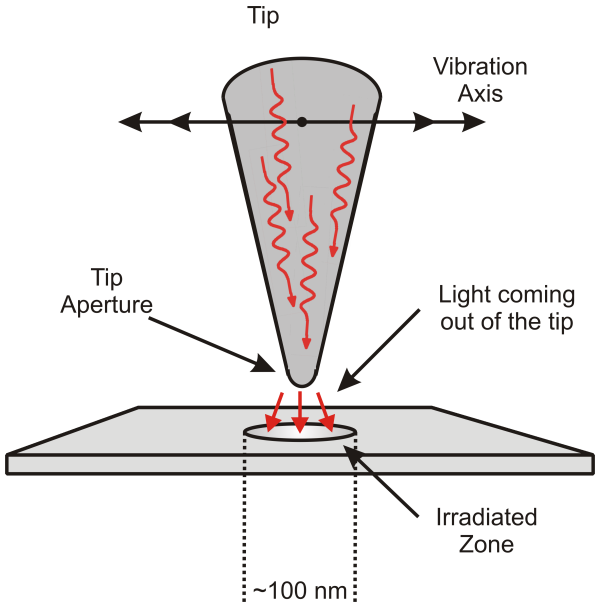

Figure 7.5: Schematic representation of the light propagation inside the tip and through the tip aperture.

coating is removed with sulphuric acid (H_2SO_4). The sulphuric acid will be heated, at least, up to $300\ C$. The fibers will be partially inmersed in the sulphuric acid for 30 minutes. Every recipient used during this process must be made of Teflon^{TM}, in order to resist the chemical attack of both fluorhidric and sulphuric acid.

7.2.4 ICP-MS Detection

To perform mass spectrometry analysis of the near-field ablated material, an ICP-MS instrument (Hewlett-Packard HP 4500, Agilent Technology) was used. A photograph of the instrument may be seen in Figure 7.7. The instrument uses a quadrupole as ion analyzer and a channeltron to detect ions. A fully detailed description of LA-ICP-MS, though without

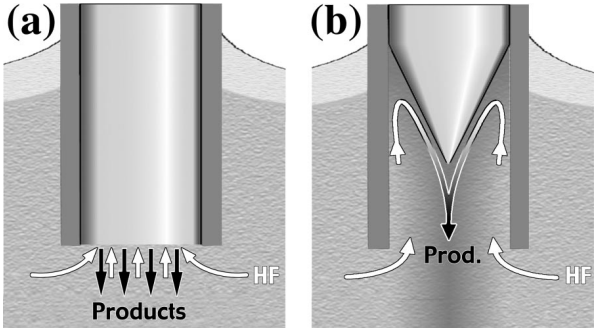

Figure 7.6: Image represents the waveguide being etched by fluorhidric acid (HF). The convection-controlled flow of the acid inside the coating capsule can be observed and how the plain ended fiber is sharply etched. Also, the acrilate coating, which resists the acid attack, is shown. Taken from [18].

the near-field stage, was given in Section 1.4.2.

7.2.5 Samples

Most of the experiments were performed on a glass coated with gold layer deposited with a conventional sputtering metallizer used for electron microscopy. Other targets like a GaAs wafer and a Ni foil with a thin layer of electrodeposited Chromium have been also used.

7.3 Results

Our experiment consisted in near-field ablation, already accomplished by other authors, but tried to combine its ultrahigh lateral resolution and negligible sample damage with the high sensitivity of an ICP-MS instrument.

The normal ablation chamber used for LA-ICP-MS was not valid for our experimental design, as it did not allow the tip (that needs to be

Figure 7.7: Photograph shows the ICP-MS instrument (Hewlett-Packard HP 4500, Agilent Technology).

nanometrically stabilized and positioned using the stage described in the previous section) to be placed near the target. The new camera was open to allow the tip to be placed over the sample's surface. It consisted on a tube with two apertures, one smaller ($\phi = 2\ mm$) in the upper side and a bigger one (rectangular, $4\ mm$ length) on the backside for sample fixation. Sample was fixed to the tubular chamber using adhesive tape so that the backside aperture is sealed. The upper side couldn't be sealed and it will probe to be a major problem, in the end. Figure 7.8 shows the scheme for the ablation chamber. As carrier gas, both He and Ar were tested, to evaluate possible influences in the transport.

As mentioned, the tips to be used in the measurements were etched at ISAS. Figure 7.9 shows two scanning electron micrographies corresponding to a typical etched tips used in our experiments. It can be seen that very sharp tips with aperture diameter well below $500\ nm$ are obtained.

As mentioned above, the targets prepared for the near-field ablation experiment consisted on a glass coated with gold layer deposited using a normal metallizer for electron microscopy. Figure 7.10 show the effects

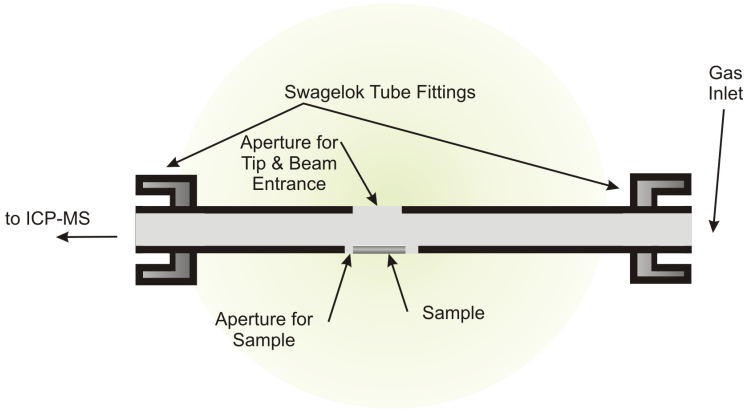

Figure 7.8: Schematic representation of the tubular chamber for NF-LA.

induced on this gold layer of a 800-nm femtosecond pulse. Craters have been micrographied by SEM. Observation of the surface modifications induced by the near-field probe reveal a rather circular shape. The diameter of these craters range from $\phi = 300 - 475\ nm$, which is below the diameter of a typical crater obtained when ablation is done by a completely focussed femtosecond laser beam (around $1\ \mu m$, for the best cases). If we compare the spot with a crater obtained using the same laser beam, but without any of the near-field components (Figure 7.11), the differences in crater-size are easily noticeables.

The attempt to measure signals for the Au on the outer layer put under the influence of the near-field probe was not succesful. Signal of gold could be obtained when the target was placed inside a commercial ablation chamber. The removal of the near-field stage to perform conventional femtosecond laser-ablation of the solid on our tubular chamber did also yield ion signal in the ICP-MS. Thus, the absence of ions may be unequivocally attributed to the near-field ablation step, considering the inefficient transport of the particles from the not-sealed ablation chamber to the ICP.

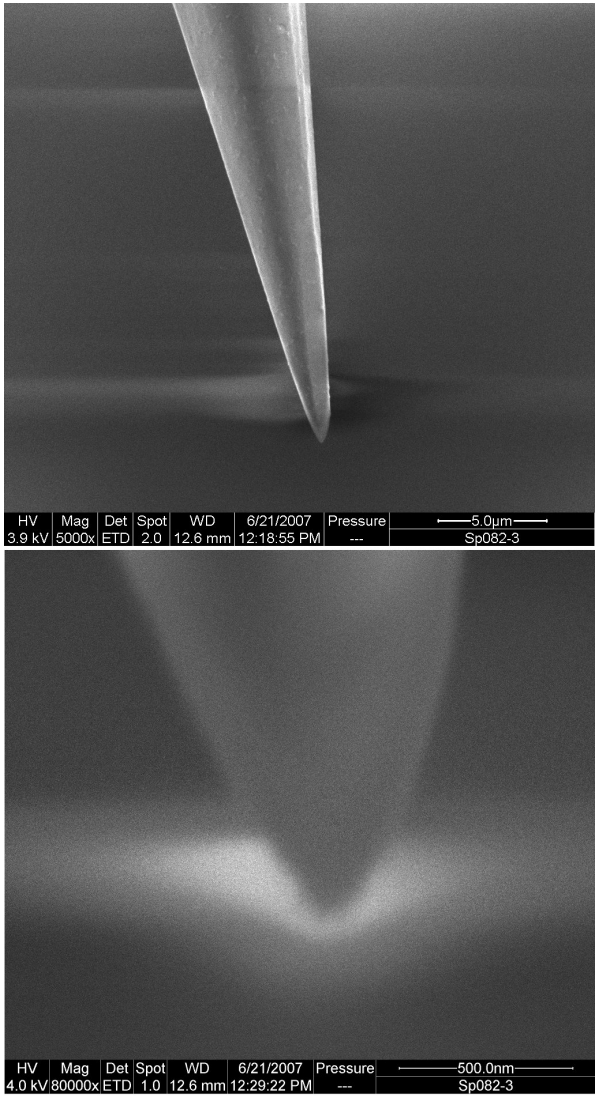

Figure 7.9: SEM micrography of a typical etched tip used for our measurements. Above, a $5\ \mu m$ zoom. Below, a $500\ nm$ zoom may be observed.

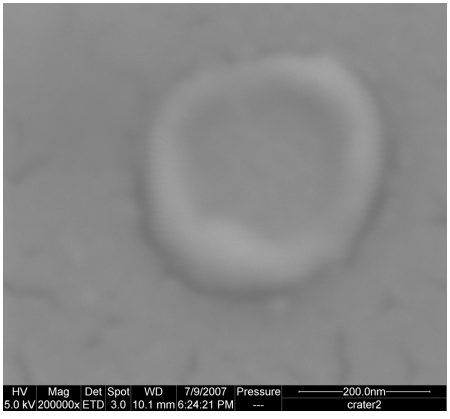

Figure 7.10: SEM micrography of a NF-LA crater with a diameter around $\phi = 300\ nm$.

In order to assess the possibility of getting any ion signal using our near-field ablation system, an experiment comparing crater size and counts measured at the detector in normal Laser-ablation configuration was made. For this purpose, a *GaAs* wafer have been analyzed. Energy per pulse was fixed at $685\ \mu J$ for a maximized signal, even though the laser was not completeley focused. Table 7.1 resumes the obtained data in terms of crater dimensions and ion signal for this *GaAs* wafer and for a given near-field crater with a diameter of $600\ nm$ in diameter. Also, as a crater depth for the near-field experiment, the same depth than the one for normal laser-ablation was taken. Depth was measured using a white light interferometer by Zygo^{TM}. Using the ratio between crater volumes (values extracted from Table 7.1):

$$Ratio_{crater\ volume} = \frac{NFLA\ crater\ volume}{LA\ crater\ volume} = 7.35x10^{-5} \qquad (7.2)$$

In near-field ablation, most ejected matter tends to quickly move away from the tiny initial volume and experiences collisions with the background gas. Comparing the laser spot size beyond the aperture with

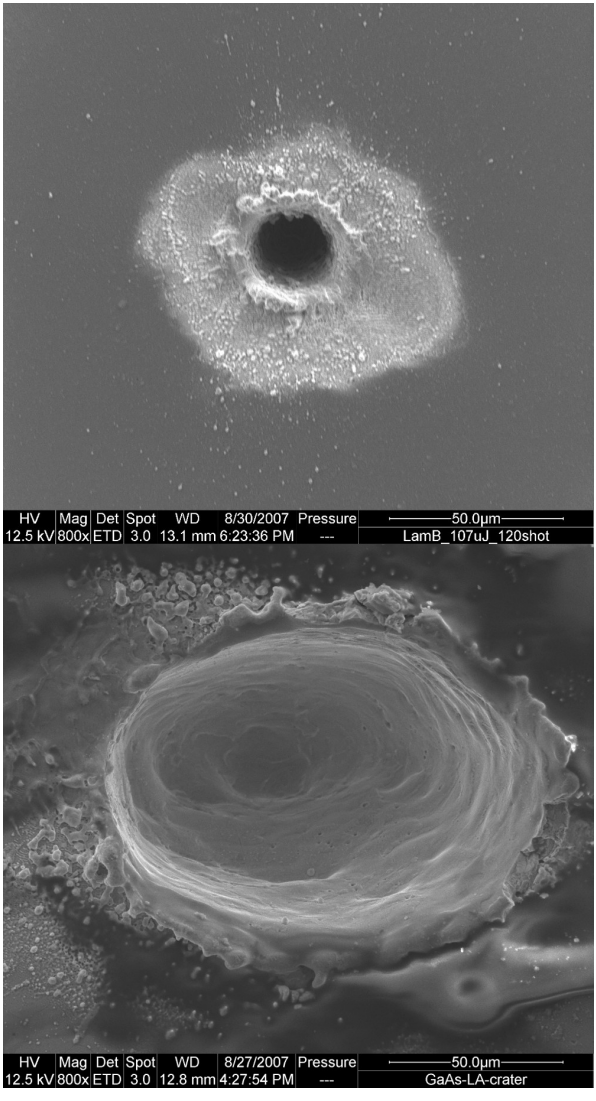

Figure 7.11: SEM micrographies of two fs-LA craters. Above, the crater made on a chromium sample is shown (Energy per pulse = $107\ \mu J$; Number of shots = $120\ shots$). Below, the crater made on a GaAs sample is shown (Energy per pulse = $142\ \mu J$; Number of shots = $8\ shots$).

Parameter	LA	NF-LA
Crater Diameter	$70\ \mu m$	$600\ nm$
Area	$3.85x10^{-9}\ m^2$	$2.83x10^{-13}\ m^2$
Depth	$6.0\ \mu m$	$6.0\ \mu m$
Volume	$2.31x10^{4}\ \mu m^3$	$1.70\ \mu m^3$
CPS	$2.05x10^{5}$	-
Estimated CPS	-	15

Table 7.1: Crater parameters. Target is a $GaAs$ wafer. Energy for both experiments was of $685\ \mu J$. Target was not on the focal point. $8\ shots$ have been averaged.

the relatively greater volume where particles expand, the laser coupling into the ablated plume and the subsequent reheating are reduced in near-field configuration.[19] This may lead to colder plume with a lower atomization degree whose transport to the ICP may be less efficient. On the other hand, strongly preferential direction of ejection may be useful if analysis is planned by techniques requiring no transport of the particles, such as LIBS. Even though emission spectroscopy tend to be less sensible than MS.[20]

Assuming, as a first aproximation, that in both cases the removed material has similar properties (in temperature, ion population, particle sizes, ...), the averaged $2.05x10^5$ counts per pulse for Ga are estimated to be around 15 counts per pulse in the case of our near-field setup. For As, signals have even lower intensity. Even in the case of an improved ion formation efficiency in the case of near-field ablation, signals will remain low. If this improvement were of one order of magnitud, *Ga* counts still would be expected to be as low as 150.

Given the shown results, integration of the near-field system with the ICP-MS was not possible with the current design. A different approach,

taken by Becker et al., was used on gels. It would use a sealed chamber in which the probe is introduced through a window sealed with an elastic piece.[12] This approach was already being developed when these experiments were done, though the Becker group didn't report more results until 2008 and 2009.[?, ?, 13] In these experiments, authors use a sealed, gasketed ablation chamber with small inner volume to place the sample. This sample is ablated using a near-field stage equipped with a *Ag* tip and a nanosecond laser pulse from a *Nd:YAG*. However, these authors use an approach different to the one used in our experiment (see Figure 7.1, as in this case a sub-threshold pulse is guided to the target and the tip, so that ablation is obtained only in the region around the tip. This first reported experiments probes that it is feasible to remove material from the solid with negligible, smaller damage and higher lateral resolution, while still performing chemical analysis.

7.4 Conclusions

Through this chapter, a novel approach to the improvement of lateral resolution for Laser-ablation Mass Spectrometry direct analysis of solid targets have been described. The results show that getting a laser to interact with a solid target in a spot size that's smaller than the usual diffraction-limited spot is feasible, even though no proper mass-spectrum signals has been detected in our experiment.

For this purpose, both apertureless and apertured tips may have a role to play. With the proper redesign, the analysis of solid targets by nf-LA-ICP-MS using femtosecond lasers and apertured tips will be possible, given recent improvements found in literature, in which an apertureless tip and a nanosecond laser are used to perform near-field mass spectrometry analysis. Also, apertured tips have been employed to perform atomic emission analysis of near-field ablated material, avoiding

the need of particle transport.

Advances that may be achieved if a new ablation chamber is designed that allow the tip to be placed near the surface while still being sealed will also help to get the chemical analysis with nanometer ranged lateral resolution to a broader public, as the technique will get more robust and easy to operate. Given recent advanced using various near-field approaches, it is not risky to say that the next years will see the arrival of near-field chemical analysis into the mainstream of analytical techniques.

Conclusions

In good agreement with the Scope exposed at the beginning of this Memory and the conclusions extracted from each single chapter, a few general conclusions may be resumed here, as follows:

1. The fluence thresholds for ion emission and plasma formation in a series of metallic samples (Zn, Al, Cu, Ni, Fe, Mo, W) have been calculated. In every case, the threshold value for ion formation was always lower than for plasma formation and exhibits dependence with the melting point of the metal.

2. The thermal-to-plasma transition has been studied by a LIPS/LIMS coincidence experiment. Although both ion formation process and plasma formation processes have been found to be different and to occur at different fluences, evidence for a thermal nature of both processes have been reported.

3. A comparison between the ionization-threshold fluence exhibited by a set of pure metal foils (Cr, Ni, Fe, Cu, Pb, Sn, Zn) and some of their reference certified alloys (Ni/Cr, Fe/Ni, Fe/Cr/Ni, Fe/Cr, and a Bronze) have been performed. The important role of the matrix

surrounding the atoms on the threshold value for ion formation has been showed.

4. Results suggest that as long as there exist proper mixing in the sample, selective ionization of elements within a complex matrix may not be possible. Additionally, influence of the spot size has been evaluated. Experimental results show that the smaller the spot size, the higher the threshold fluence for ion formation.

5. Time-delayed two-pulse laser ionization results are reported for a series of solid targets (Al, Cu, Fe, Si, Ti, and an AISI 314 stainless steel). A pump-probe experiment using two frequency-doubled Nd:YAG lasers collinearly aligned operating under ionization threshold fluences has demonstrated the existence of an optimum interpulse delay where a maximum ion yield occurs. This maximum occurs when an interpulse delay of $60\ ns$ is used. Other effects have been found to occur simultaneously with the maximum ion yield, as a shifting to lower flight times, which is minimum at an interpulse delay matching exactly the one for maximum ion yield.

6. When two sub-threshold laser pulses are applied to a metallic target, the response obtained for different delays seems to be in accordance with the sequence of events that takes place during laser-matter interaction. An hypothesis for this behaviour may be related to sample changes (roughness, temperature, among others), as a consequence of the the first laser pulse reaching the sample. The duration of this modification may vary from one material to another and that fact may help us to understand the differences observed in optimum delay among the materials.

7. The fragmentation patterns of 2,6-DNT have been studied with different wavelengths. Among the tested wavelengths, the 266-nm

is found to be the one that provides the best quality of analysis. The effect of the extraction-pulse width and delay have been investigated and the possibility of a modulated analysis where both atomic and molecular information can be obtained has been proven.

8. Experiments of laser-ablation with excellent lateral resolution have been performed using a SNOM interface to confine the laser beam in a region with a diameter smaller than the one predicted by the diffraction limit. This is a novel approach for the improvement of lateral resolution for laser-ablation mass spectrometry direct analysis of solid targets. The results show that getting a laser to interact with a solid target in a spot size that is smaller than the usual diffraction-limited spot is feasible, even though no proper mass-spectrum signals has been detected. Results show that our approach is not optimal and proper ion detection is hard under these experimental conditions. However, advances may be achieved if a new ablation chamber is designed that allow the tip to be placed near the surface while still being sealed.

Conclusiones

Con un buen ajuste a los Objetivos expuestos al principio de esta memoria y las conclusiones extraídas en cada capítulo, se resumen aquí algunas conclusiones generales:

1. Los umbrales de fluencia para la formación de iones y para la formación de plasma han sido calculados para una serie de muestras metálicas (Zn, Al, Cu, Ni, Fe, Mo, W). Para cada metal, el valor umbral determinado para la formación de iones fue menor que el valor umbral determinado para la formación de plasmas. Así mismo, existe correlación entre los valores umbral para estos fenómenos y los puntos de fusión del metal.

2. La transición del régimen término a un régimen con formación de plasma ha sido estudiada mediante experimentos de coincidencias LIMS/LIPS. Aunque se ha encontrado que ambos procesos son diferentes, de ahí los diferentes valores umbral para su aparición, se ha encontrado evidencia experimental de la naturaleza térmica tanto de la formación de iones como de la formación de plasma.

3. Una comparación entre la fluencia umbral de ionización exhibida por un grupo de muestras metálicas puras y algunas de sus aleaciones

(Ni/Cr, Fe/Ni, Fe/Cr/Ni, Fe/Cr, y bronce) ha sido realizada. El importante papel desempeñado por la matriz que rodea a los átomos en el metal y su influencia en el valor umbral para la formación de iones ha sido demostrado.

4. Los resultados sugieren que mientras exista una mezcla apropiada de los componentes en la mezcla, la ionización selectiva de elementos concretos dentro de una matriz compleja no resulta factible. Adicionalmente, la influencia del tamaño de la huella láser ha sido evaluada. Los resultados experimentales muestran que al disminuir el tamaño de la huella láser, el valor de fluencia umbral para la formación de iones aumenta.

5. Se han realizado experimentos de ionización de muestras metálicas y semimetálicas (Al, Cu, Fe, Si, Ti, y acero inoxidable AISI 314) utilizando dos pulsos láser, con un retraso controlado entre ambos. Los experimentos sonda-prueba realizados con dos pulsos láser ($532nm$) colineales con fluencia subumbral demuestran la existencia de un retraso entre pulsos óptimo para el cual se alcanza un máximo en la señal de iones. Este máximo se encuentra cuando se utiliza un retraso entre pulsos de $60\ ns$. Además, se observó la presencia de otros efectos concomitantes a la aparición de ese máximo de señal, como el movimiento de las señales LIMS a menores tiempos de vuelo, que resultó ser mínimo para el retraso entre pulsos que ofrecía el máximo de señal.

6. Cuando dos pulsos láser con fluencia subumbral son enfocados sobre una muestra metálica, la respuesta obtenida para diferentes retrasos parece concordar con la secuencia de eventos que tienen lugar durante la interacción laser materia. Una hipótesis para este comportamiento podría estar relacionado con cambios en la mues-

tra (rugosidad, temperatura, entre otros), como consecuencia de la acción del primer pulso láser. La duración de estas modificaciones podría variar de un material a otro y ese hecho podría ayudarnos a comprender las pequeñas diferencias observadas en el retraso óptimo para cada material.

7. Los patrones de fragmentación del 2,6-DNT han sido estudiados con diferentes longitudes de onda. De entre las longitudes de onda utilizadas, los análisis de mayor calidad fueron obtenidos usando un haz láser de 266nm. El efecto de la anchura y el retraso del pulso de extracción han sido investigados y la posibilidad de realizar análisis con modulación de la señal obtenida en los cuales hay presente tanto información atómica como molecular ha sido demostrada.

8. Se realizaron experimentos de ablación láser con excelente resolución lateral utilizando un sistema SNOM para confinar el haz láser en una región de tamaño inferior al límite de difración. Ésta es una aproximación novedosa para la mejora de la resolución lateral en el análisis directo de sólidos mediante espectrometría de masas con ablación láser, capaz de realizar análisis de sólidos con una huella láser que sea menor que el límite de difracción es posible. Aunque los experimentos realizados no consiguieron obtener espectros de masas, los resultados muestran que nuestra aproximación no es óptima y que la detección de iones sería posible, siempre que el sistema sea optimizado.

References

Bibliography for Chapter 1

[1] Joseph John Thomson. *Rays of Positive Electricity and Their Application to Chemical Analyses*. Longmans, Green and Co., 1913.

[2] Albert Einstein. Zur quantentheorie der strahlung. *Physikalische Zeitschrift*, 18: 121–128, 1917.

[3] D. Günther and B. Hattendorf. Solid sample analysis using laser-ablation- inductively coupled plasma mass spectometry. *Trends in Analytical Chemistry*, 24: 255–265, 2005.

[4] Alan Chodos. This month in physics history: April 1946: First concept of time-of-flight mass spectrometer. http://www.aps.org/publications/apsnews/200104/history.cfm, April 2001. APS Website, last accesed 18th June 2009.

[5] Theodore H. Maiman. Stimulated optical radiation in ruby. *Nature*, 187:493–494, 1960.

[6] C. H. Townes, J. P. Gordon, and H. J. Zeiger. The maser¯new type of microwave amplifier, frequency standard, and spectrometer. *Phys. Rev.*, 99(4):1264–1274, Aug 1955.

[7] A. L. Schawlow and C. H. Townes. Infrared and optical masers. *Phys. Rev.*, 112 (6):1940–1949, Dec 1958.

[8] R. E. Hönig and J. R. Woolston. Laser-induced emission of electrons, ions, and neutral atoms from solid surfaces. *Applied Physics Letters*, 2(7):138–139, 1963.

[9] F. P. Lossing, K. U. Ingold, and I. H. S. Henderson. Free radicals by mass spectrometry. vi. the bond dissociation energies of some methyl, allyl, and benzyl compounds by electron impact. *The Journal of chemical physics*, 22(9):1489–1492, 1954.

[10] M. S. B. Munson and F. H. Field. Chemical ionization mass spectrometry. i. general introduction. *Journal of the American Chemical Society*, 88(12):2621–2630, 1966.

[11] H.W. Werner. Instrumental aspects of secondary ion mass spectrometry and secondary ion imaging mass spectrometry. *Vacuum*, 22(11):613 – 617, 1972.

[12] M. Yamashita and J. B. Fenn. Electrospray ion source. another variation on the free-jet theme. *Journal of Physical Chemistry*, 88(20):4451–4459, 1984.

[13] P. Feigl, B. Schueler, and F. Hillenkamp. Lamma 1000, a new instrument for bulk microprobe mass analysis by pulsed laser irradiation. *International Journal or Mass Spectrometry and Ion Physics*, 47:15–18, 1983.

[14] Michael Karas, Doris Bachmann, and Franz Hillenkamp. Influence of the wavelength in high-irradiance ultraviolet laser desorption mass spectrometry of organic molecules. *Analytical Chemistry*, 57(14):2935–2939, 1985.

[15] Stefan Berkenkamp, Finn Kirpekar, and Franz Hillenkamp. Infrared maldi mass spectrometry of large nucleic acids. *Science*, 281(5374):260–262, 1998.

[16] M. Takayama. N=c bond cleavage of the peptide backbone via hydrogen abstraction. *Journal of the American Society for Mass Spectrometry*, 12(9):1044–1049, 2001.

[17] Salvatore Siano. *Handbook on the Use of Lasers in Conservation and Conservation Science. COST G7 (2007)*, chapter Principles of Laser Cleaning in Conservation. 2007.

[18] J.M. Vadillo and J.J. Laserna. Laser-induced breakdown spectrometry: truly a surface analytical tool. *Spectrochimica Acta Part B*, 59:147–161, 2004.

[19] G. Siuzdak. The emergence of mass spectrometry in biochemical research. *Proceedings of the National Academy of Sciences of the United States of America*, 91 (24):11290–11297, 1994.

[20] Michael Karas and Franz Hillenkamp. Laser desorption ionization of proteins with molecular masses exceeding 10,000 daltons. *Analytical Chemistry*, 60(20):2299–2301, 1988.

[21] K. Tanaka, H. Waki, Y. Ido, S. Akita, Y. Yoshida, and T. Yoshida. Protein and polymer analyses of up to m/z 100,000 by laser ionization time-of-flight mass spectrometry. *Rapid Communications in Mass Spectrometry*, 2(8):151–153, 1988.

[22] G. P. Jonsson, A. B. Hedin, P. L. Hakansson, B. U. R. Sundqvist, B. G. S. Säve, P. F. Nielsen, P. Roepstorff, K. . Johansson, I. Kamensky, and M. S. L. Lindberg. Plasma desorption mass spectrometry of peptides and proteins adsorbed on nitrocellulose. *Analytical Chemistry*, 58(6):1084–1087, 1986.

[23] S. Bouchonnet, J. . Denhez, Y. Hoppilliard, and C. Mauriac. Is plasma desorption mass spectrometry useful for small-molecule analysis? fragmentations of the natural -amino acids. *Analytical Chemistry*, 64(7):743–754, 1992.

[24] Kathrin Breuker, Mi Jin, Xuemei Han, Honghai Jiang, and Fred W. McLafferty. Top-down identification and characterization of biomolecules by mass spectrometry. *Journal of the American Society for Mass Spectrometry*, 19(8):1045 – 1053, 2008.

[25] Kevin Demeure, Loic Quinton, Valerie Gabelica, and Edwin De Pauw. Rational selection of the optimum maldi matrix for top-down proteomics by in-source decay. *Analytical Chemistry*, 79(22):8678–8685, 2007.

[26] J. S. Becker, M. Zoriy, J. S. Becker, C. Pickhardt, E. Damoc, G. Juhacz, M. Palkovits, and M. Przybylski. Determination of phosphorus-, copper-, and zinc-containing human brain proteins by la-icpms and maldi-fticr-ms. *Analytical Chemistry*, 77 (18):5851–5860, 2005.

[27] Michael V. Ugarov, T. Egan, Dmitry V. Khabashesku, J. Albert Schultz, Haiqing Peng, Valery N. Khabashesku, Hiroshi Furutani, Kimberley S. Prather, H-W. J. Wang, S. N. Jackson, and Amina S. Woods. Maldi matrices for biomolecular analysis based on functionalized carbon nanomaterials. *Analytical Chemistry*, 76(22): 6734–6742, 2004.

[28] Yu-Fen Huang and Huan-Tsung Chang. Analysis of adenosine triphosphate and glutathione through gold nanoparticles assisted laser desorption/ionization mass spectrometry. *Analytical Chemistry*, 79(13):4852–4859, 2007.

[29] Michael Karas and Ralf Krüger. Ion formation in maldi: the cluster ionization mechanism. *Chemical Reviews*, 103(2):427–440, 2003.

[30] Renato Zenobi and Richard Knochenmuss. Ion formation in maldi mass spectrometry. *Mass Spectrometry Reviews*, 17:337–366, 1999.

[31] B. Spengler. Post-source decay analysis in matrix-assisted laser desorption/ionization mass spectrometry of biomolecules. *Journal of Mass Spectrometry*, 32(10):1019–1036, 1997.

[32] M. Ohkubo, Y. Shigeri, T. Kinumi, N. Saito, M. Ukibe, Y.E. Chen, A. Kushino, A. Kurokawa, H. Sato, and S. Ichimura. Fragmentation analysis by superconduct-

ing ion detectors in matrix-assisted laser desorption/ionization (maldi). *Nuclear Instruments and Methods in Physics Research Section A: Accelerators, Spectrometers, Detectors and Associated Equipment*, 559(2):779 – 781, 2006. Proceedings of the 11th International Workshop on Low Temperature Detectors - LTD-11.

[33] E. Dudley, R. Tuytten, A. Bond, F. Lemière, A. G. Brenton, E. L. Esmans, and R. P. Newton. Study of the mass spectrometric fragmentation of pseudouridine: Comparison of fragmentation data obtained by matrix-assisted laser desorption/ionisation post-source decay, electrospray ion trap multistage mass spectrometry, and by a method utilising electrospray quadrupole time-of-flight tandem mass spectrometry and in-source fragmentation. *Rapid Communications in Mass Spectrometry*, 19(21):3075–3085, 2005.

[34] R. Knochenmuss. A quantitative model of ultraviolet matrix-assisted laser desorption/ionization. *Journal of Mass Spectrometry*, 37(8):867–877, 2002.

[35] F. Brech and L. Cross. Optical microemission stimulated by a ruby maser. *Applied Spectroscopy*, 16:59–63, 1962.

[36] David A. Cremers and A. K. Knight. *Laser-induced breakdown spectroscopy, In Encyclopedia of Analytical Chemistry Vol. 11*. Wiley, 2000.

[37] Andrzej W. Miziolek, Vincenzo Palleschi, and Israel Schechter. *Laser Induced Breakdown Spectroscopy*. Cambridge University Press, 2006.

[38] X.L. Mao, A.C. Ciocan, O.V. Borisov, and R.E. Russo. Laser ablation processes investigated using icp-aes. *Applied Surface Science*, 127-129:262–268, 1998.

[39] W. . Lee, J. Wu, Y. . Lee, and J. Sneddon. Recent applications of laser-induced breakdown spectrometry: A review of material approaches. *Applied Spectroscopy Reviews*, 39(1):27–97, 2004.

[40] F. J. Fortes, J. Cuñat, L. M. Cabalín, and J. J. Laserna. In situ analytical assessment and chemical imaging of historical buildings using a man-portable laser system. *Applied Spectroscopy*, 61(5):558–564, 2007.

[41] L.J. Radziemski and D.A. Cremers. *Laser-induced Plasmas and Applications*. Marcel Dekker, 1989.

[42] F.J. Fortes. *Técnicas láser para el análisis y diagnóstico de bienes de interés patrimonial: estudio de materiales de la catedral de Málaga y de colecciones del museo arqueológico provincial*. PhD thesis, Universidad de Málaga, 2007.

[43] C.M. Davies, H.H. Telle, D.J. Montgomery, and R.E. Corbett. Quantitative analysis using remote laser-induced breakdown spectroscopy (libs). *Spectrochimica Acta Part B: Atomic Spectroscopy*, 50(9):1059 – 1075, 1995.

[44] S. Amoruso. Modeling of uv pulsed-laser ablation of metallic targets. *Applied Physics A: Materials Science & Processing*, 63(3):323–332, 1999.

[45] A. Bogaerts, Z.Y. Chen, R. Gijbels, and A. Vertes. Laser ablation for analytical sampling: what can we learn from modeling? *Spectrochimica Acta Part B*, 58(11): 1867–1893, 2003.

[46] P.S. Dalyander, I.B. Gornushkin, and D.W. Hahn. Numerical simulation of laser-induced breakdown spectroscopy: Modeling of aerosol analysis with finite diffusion and vaporization effects. *Spectrochimica Acta Part B: Atomic Spectroscopy*, 63(2): 293 – 304, 2008. Honoring Issue A Collection of Papers on Atomic, Molecular and Laser Spectroscopy Dedicated to James D. Winefordner.

[47] K. Meissner, T. Lippert, A. Wokaun, and D. Günther. Analysis of trace metals in comparison of laser-induced breakdown spectroscopy with la-icp-ms. *Thin Solid Films*, 453-454:316–322, 2004.

[48] S. F. Durrant and N. I. Ward. Recent biological and environmental applications of laser ablation inductively coupled plasma mass spectrometry (la-icp-ms). *Journal of Analytical Atomic Spectrometry*, 20(9):821–829, 2005.

[49] R.ˊLobiński, D. Schaumlöffel, and J. Szpunar. Mass spectrometry in bioinorganic analytical chemistry. *Mass spectrometry reviews*, 25(2):255–289, 2006.

[50] J. Sabine Becker and Hans-Joachim Dietze. State-of-the-art in inorganic mass spectrometry for analysis of high-purity materials. *International Journal of Mass Spectrometry*, 228(2-3):127 – 150, 2003. Special Issue: In honour of Helmut Schwarz.

[51] Douglas A. Skoog and James J. Leary. *Análisis Instrumental (4ª ed.)*. Saunders College Publishing, 1996.

[52] Ales Hrdlicka, Vítezslav Otruba, Karel Novotný, Detlef Günther, and Viktor Kanický. Feasibility of depth profiling of zn-based coatings by laser ablation inductively coupled plasma optical emission and mass spectrometry using infrared nd:yag and arf* lasers. *Spectrochimica Acta Part B: Atomic Spectroscopy*, 60(3):307 – 318, 2005. 6th European Furnace Symposium and 11th Solid Sampling Colloquium with Atomic Spectrometry.

[53] J. Pisonero, J. Koch, M. Wälle, W. Hartung, N. D. Spencer, and D. Günther. Capabilities of femtosecond laser ablation inductively coupled plasma mass spectrometry for depth profiling of thin metal coatings. *Analytical Chemistry*, 79(6):2325–2333, 2007.

[54] C.C. García, H. Lindner, A. von Bohlen, C. Vadla, and K. Niemax. Elemental fractionation and stoichiometric sampling in femtosecond laser ablation. *Journal of Analytical Atomic Spectrometry*, 23:470–478, 2008.

[55] Alexander A. Sysoev and Alexey A. Sysoev. Can laser-ionisation time-of-flight mass spectrometry be a promising alternative to laser ablation/inductively-coupled plasma mass spectrometry and glow discharge mass spectrometry for the elemental analysis of solids? *European Journal of Mass Spectrometry*, 8(3):213–232, 2002.

[56] Jian He, Wenwan Zhong, Cynthia Mahan, and Wei Hang. Laser ablation and ionization time-of-flight mass spectrometer with orthogonal sample introduction and axial field rf-only quadrupole cooling. *Spectrochimica Acta Part B: Atomic Spectroscopy*, 61(2):220 – 224, 2006.

[57] Q. Tong, Q. Yu, X. Jin, J. He, W. Hang, and B. Huang. Semi-quantitative analysis of geological samples using laser plasma time-of-flight mass spectrometry. *Journal of Analytical Atomic Spectrometry*, 24(2):228–231, 2009.

[58] Jose M. Vadillo, Carmen C. García, Jose F. Alcántara, and J. Javier Laserna. Thermal-to-plasma transitions and energy thresholds in laser ablated metals monitored by atomic emission/mass spectrometry coincidence analysis. *Spectrochimica Acta Part B*, 60:948–954, 2005.

[59] H. Téllez, J. M. Vadillo, R. J. Chater, J. J. Laserna, and D. S. McPhail. Focused ion beam imaging of laser ablation sub-surface effects on layered materials. *Applied Surface Science*, 255:2265–2269, 2008.

[60] C. López-Moreno, S. Palanco, J. J. Laserna, F. DeLucia Jr., A. W. Miziolek, J. Rose, R. A. Walters, and A. I. Whitehouse. Test of a stand-off laser-induced breakdown spectroscopy sensor for the detection of explosive residues on solid surfaces. *Journal of Analytical Atomic Spectrometry*, 21(1):55–60, 2006.

[61] F. C. De Lucia Jr., J. L. Gottfried, C. A. Munson, and A. W. Miziolek. Double pulse laser-induced breakdown spectroscopy of explosives: Initial study towards improved discrimination. *Spectrochimica Acta - Part B Atomic Spectroscopy*, 62 (12):1399–1404, 2007.

[62] R.E. Russo, X.L. Mao, O.V. Borisov, and H. Liu. Influence of wavelength on fractionation in laser ablation icp-ms. *Journal of Analytical Atomic Spectrometry*, 15: 1115–1120, 2000.

[63] W.B. Brinckerhoff. On the possible in situ elemental analysis of small bodies with laser ablation tof-ms. *Planetary and Space Science*, 53:817–838, 2005.

[64] W. C. Wiley and I. H. McLaren. Time-of-flight mass spectrometer with improved resolution. *Review of Scientific Instruments*, 26(12):1150–1157, 1955.

[65] Boris A. Mamyrin, VI Karataev, and DV Shmikk. Mass-reflectron, a new nonmagnetic time-of-flight high-resolution mass-spectrometer. *Zhurnal Eksperimentalnoi i Teoreticheskoi Fiziki*, 64:82–89, 1973.

[66] Matthias Frank. Mass spectrometry with cryogenic detectors. *Nuclear Instruments and Methods in Physics Research A*, 444:375–384, 2000.

[67] R. J. Wenzel, U. Matter, L. Schultheis, and R. Zenobi. Analysis of megadalton ions using cryodetection maldi time-of-flight mass spectrometry. *Analytical Chemistry*, 77(14):4329–4337, 2005.

[68] L Schulz. Sputter-ion pumps. (OPEN-2000-264), 1999.

Bibliography for Chapter 2

[1] R. W. Dreyfus. *Laser Ablation of Electronic Materials: Basic Mechanisms and Applications,*. Elsevier Publishers, 1992.

[2] S. H. Jeong, R. Greif, and R. E. Russo. Numerical modeling of pulsed laser evaporation of aluminum targets. *Applied Surface Science*, 127-129:177–183, 1998.

[3] A. Vertes, R.W. Dreyfus, and D.E. Platt. Modeling the thermal-to-plasma transitions for cu photoablation. *IBM Journal of Research and Development*, 38:3–10, 1994.

[4] A. Bogaerts, Z.Y. Chen, R. Gijbels, and A. Vertes. Laser ablation for analytical sampling: what can we learn from modeling? *Spectrochimica Acta Part B*, 58(11): 1867–1893, 2003.

[5] Akos Vertes. *Laser Ablation: Mechanisms and Applications II*, chapter Energy coupling and dissipation mechanisms in laser-solid interaction, pages 275–284. AIP Press, 1994.

[6] S. Amoruso. Modeling of uv pulsed-laser ablation of metallic targets. *Applied Physics A: Materials Science & Processing*, 63(3):323–332, 1999.

[7] S. Georgiou and A. Koubenakis. Laser-induced material ejection from model molecular solids and liquids: Mechanisms, implications, and applications. *Chemical Reviews*, 103:343–393, 2003.

[8] P.S. Dalyander, I.B. Gornushkin, and D.W. Hahn. Numerical simulation of laser-induced breakdown spectroscopy: Modeling of aerosol analysis with finite diffusion and vaporization effects. *Spectrochimica Acta Part B: Atomic Spectroscopy*, 63(2): 293 – 304, 2008. Honoring Issue A Collection of Papers on Atomic, Molecular and Laser Spectroscopy Dedicated to James D. Winefordner.

[9] Martin von Allmen and Andreas Blatter. *Laser-Beam Interactions with Materials: Physical Principles and Applications*. Springer, 2002.

[10] D.S. Ivanov and B. Rethfeld. The effect of pulse duration on the interplay of electron heat conduction and electron-phonon interaction: photo-mechanical vs. photo-thermal damage of metal targets. *Applied Surface Science*, 2009.

[11] S.S. Wellershoff, J. Hohlfeld, J. Güdde, and E. Matthias. The role of electron–phonon coupling in femtosecond laser damage of metals. *Applied Physics A*, 69:S99–S107, 1999.

[12] S. Yalçin, Y.Y. Tsui, and R. Fedosejevs. Images of femtosecond laser plasma plume expansion into background air. *IEEE Transactions on plasma science*, 33:482–483, 2005.

[13] K.R. Chen, J.N. Leboeuf, R.F. Wood, D.B. Geohegan, J.M. Donato, C.L. Liu, and A.A. Puretzky. Laser–solid interaction and dynamics of laser-ablated materials. *Applied Surface Science*, 96-98:45–49, 1996.

[14] R.F. Wood, J.N. Leboeuf, K.R. Chen, D.B. Geohegan, and A.A. Puretzky. Dynamics of plume propagation, splitting and nanoparticle formation during pulsed-laser ablation. *Applied Surface Science*, 127-129:151–158, 1998.

[15] A.G. Gnedovets, A.V. Gusarov, and I. Smurov. Submicron particles synthesis by laser evaporation at low power density: a numerical analysis. *Applied Surface Science*, 154-155:508–513, 2000.

[16] A.P.K. Leung, W.T. Chan, X.L. Mao, and R.E. Russo. Influence of gas environment on picosecond laser ablation sampling efficiency and icp conditions. *Analytical Chemistry*, 70:4709–4716, 1998.

[17] A. Bogaerts and Z.Y. Chen. Effect of laser parameters on laser ablation and laser-induced plasma formation: A numerical modeling investigation. *Spectrochimica Acta Part B*, 60(9-10):1280–1307, 2005.

[18] H.C. Liu, X.L. Mao, J.H. Yoo, and R.E. Russo. Early phase laser-induced plasma diagnostics and mass removal during single-pulse laser ablation of silicon. *Spectrochimica Acta Part B*, 54:1607–1624, 1999.

[19] D. Günther, B. Hattendorf, and C. Latkoczy. La-icp-ms – it's particle size that really matters. *Analytical Chemistry*, 75:341A–347A, 2003.

[20] G. Callies, H. Schittenhelm, P. Berger, and H. Hügel. Modeling of the expansion of laser-evaporated matter in argon, helium and nitrogen and the condensation of clusters. *Applied Surface Science*, 127–129:134–141, 1998.

[21] L. V. Zhigilei. Dynamics of the plume formation and parameters of the ejected clusters in short-pulse laser ablation. *Appl. Phys. A*, 76:339–350, 2003.

[22] X. Zhang, S.S. Chu, J.R. Ho, and C.P. Grigoropoulos. Excimer laser ablation of thin gold films on a quartz crystal microbalance at various argon background pressures. *Appl. Phys. A*, 64:545–552, 1997.

[23] Q. Lu, S.S. Mao, X. Mao, and R.E. Russo. Delayed phase explosion during high-power nanosecond laser ablation of silicon. *Appl. Phys. Lett.*, 80:3072–3074, 2002.

[24] Q. Bian, C.C. Garcia, J. Koch, and K. Niemax. Non-matrix matched calibration of major and minor concentrations of zn and cu in brass, aluminium and silicate glass using nir femtosecond laser ablation inductively coupled plasma mass spectrometry. *Journal of Analytical Atomic Spectrometry*, 21:187–191, 2006.

[25] J. Koch, M. Wälle, J. Pisonero, and D. Günther. Performance characteristics of ultra-violet femtosecond laser ablation inductively coupled plasma mass spectrometry at 265 and 200 nm. *Journal of Analytical Atomic Spectrometry*, 21:932–940, 2006.

[26] C. C. Garcia, Helmut Lindner, and Kay Niemax. Laser ablation inductively coupled plasma mass spectrometry—current shortcomings, practical suggestions for improving performance, and experiments to guide future development. *Journal of Analytical Atomic Spectrometry*, 24:14–26, 2009.

[27] S.M. Eggins, L.P.J. Kinsley, and J.M.G. Shelley. Deposition and element fractionation processes during atmospheric pressure laser sampling for analysis by icp-ms. *Applied Surface Science*, 127–129:278–286, 1998.

[28] C.C. García, H. Lindner, A. von Bohlen, C. Vadla, and K. Niemax. Elemental fractionation and stoichiometric sampling in femtosecond laser ablation. *Journal of Analytical Atomic Spectrometry*, 23:470–478, 2008.

[29] J. Koch, A. von Bohlen, R. Hergenröder, and K. Niemax. Particle size distributions and compositions of aerosols produced by near-ir femto-and nanosecond laser ablation of brass. *Journal of Analytical Atomic Spectrometry*, 19:267–272, 2004.

[30] D. Bleiner and A. Bogaerts. Multiplicity and contiguity of ablation mechanisms in laser-assisted analytical micro-sampling. *Spectrochimica Acta - Part B Atomic Spectroscopy*, 61(4):421–432, 2006.

[31] Nathan J. Saetveit, Stanley J. Bajic, David P. Baldwin, and R. S. Houk. Influence of particle size on fractionation with nanosecond and femtosecond laser ablation in brass by online differential mobility analysis and inductively coupled plasma mass spectrometry. *Journal of Analytical Atomic Spectrometry*, 23:54–61, 2008.

[32] M. Guillong, H.-R. Kuhn, and D. Günther. Application of a particle separation device to reduce inductively coupled plasma-enhanced elemental fractionation in laser ablation inductively coupled plasma mass spectrometry. *Spectrochimica Acta Part B*, 58:211–220, 2003.

[33] Gabriele Cristoforetti, Stefano Legnaioli, Vincenzo Palleschi, Elisabetta Tognoni, and Pier Alberto Benedetti. Observation of different mass removal regimes during the laser ablation of an aluminium target in air. *Journal of Analytical Atomic Spectrometry*, 23:1518–1528, 2008.

[34] Z. Chen and A. Bogaerts. Laser ablation of cu and plume expansion into 1 atm ambient gas. *Journal of Applied Physics*, 97:063305, 2005.

[35] J.R. Ho, C.P. Grigoropoulos, and J.A.C. Humphrey. Computational study of heat transfer and gas dynamics in the pulsed laser evaporation of metals. *Journal of Applied Physics*, 78:4696–4709, 1995.

[36] T.D. Bennett, C.P. Grigoropoulos, and D.J. Krajnovic. Near-threshold laser sputtering of gold. *Journal of Applied Physics*, 77:849–864, 1995.

[37] R. Haglund. Microscopic and mesoscopic aspects of laser-induced desorption and ablation. *Applied Surface Science*, 96-98:1–13, 1996.

[38] P.W. Atkins. *Physical Chemistry, 6ª ed*. 1999.

[39] Roger Kelly and Antonio Miotello. Contribution of vaporization and boiling to thermal-spike sputtering by ions or laser pulses. *Phys. Rev. E*, 60:2616–2625, 1999.

[40] R. P. Tong, W.P. Schiffers, S.J. Shaw, J.R. Blake, and D.C. Emmony. The role of in the collapse of a laser-generated cavity near a rigid boundary. *Journal of Fluid Mechanics*, 380(-1):339–361, 1999.

[41] Davide Bleiner, Zhaoyang Chen, David Autrique, and Annemie Bogaerts. Role of laser-induced melting and vaporization of metals during icp-ms and libs analysis, investigated with computer simulations and experiments. *Journal of Analytical Atomic Spectrometry*, 21:910–921, 2006.

[42] R. Hergenröder. A model of non-congruent laser ablation as a source of fractionation effects in la-icp-ms. *Journal of Analytical Atomic Spectrometry*, 21:505–516, 2006.

[43] Yasuyuki Tsuboi, Koji Hatanaka, Hiroshi Fukumura, and Hiroshi Masuhara. The 248 nm excimer laser ablation of liquid benzene derivatives: A relation between ablation threshold and molecular photochemical reactivity. *The Journal of Physical Chemistry*, 98(44):11237–11241, 1994.

[44] K. Domen and T. J. Chuang. Laser induced photodissociation and desorption. i. ch_2i_2 adsorbed on al_2o_3. *Journal of Chemical Physics*, 90:3318–3331, 1989.

[45] Renato Zenobi and Richard Knochenmuss. Ion formation in maldi mass spectrometry. *Mass Spectrometry Reviews*, 17:337–366, 1999.

[46] R. Knochenmuss and L.V. Zhigilei. Molecular dynamics model of ultraviolet matrix-assisted laser desorption/ionization including ionization processes. *Journal of Physical Chemistry B*, 109:22947–22957, 2005.

[47] V. P. Carey, G. Chen, C. Grigoropoulos, M. Kaviany, and A. Majumdar. A review of heat transfer physics. *Nanoscale and Microscale Thermophysical Engineering*, 12:1–60, 2008.

[48] Frédéric Aubriet and Jean-François Muller. Laser ablation mass spectrometry of inorganic transition metal compounds. additional knowledge for the understanding of ion formation. *Journal of The American Society for Mass Spectrometry*, 19:488–501, 2008.

[49] Savas Georgiou and Franz Hillenkamp. Introduction: Laser ablation of molecular substrates. *Chemical Reviews*, 103:317–320, 2003.

[50] A. Koubenakis, J. Labrakis, and S. Georgiou. Pulse dependence of ejection efficiencies in the uv ablation of bi-component van der waals solids. *Chemical Physical Letters*, 346:54–30, 2001.

[51] S. Amoruso, R. Bruzzese, N. Spinelli, and R. Velotta. Characterization of laser-ablation plasmas. *Journal of Physics B*, 32:R131–R172, 1999.

[52] L. Balazs, R. Gijbels, and A. Vertes. Expansion of laser-generated plumes near the plasma ignition threshold. *Analytical Chemistry*, 63:314–320, 1991.

[53] E.M. Monge, C. Aragón, and J.A. Aguilera. Space- and time-resolved measurements of temperatures and electron densities of plasmas formed during laser ablation of metallic samples. *Appl. Phys. A*, 69:S691–S694, 1999.

[54] Borja Sierra. *Estudio de procesos de ionización sobre clorofluorometanos por impacto electrónico y por ablación láser en cobre y aluminio*. PhD thesis, Universidad del País Vasco, 2006.

[55] Jon I. Apiñaniz, Borja Sierra, Roberto Martínez, Asier Longarte, Carolina Redondo, and Fernando Castaño. Ion kinetic energy distributions and mechanisms of pulsed laser ablation on al. *The Journal of Physical Chemistry C*, 112(42):16556–16560, 2008.

[56] Roger Kelly and R.W. Dreyfus. Reconsidering the mechanisms of laser sputtering with knudsen-layer formation taken into account. *Nuclear Instruments and Methods in Physics Research B*, 32:341–348, 1988.

[57] C. Porneala and D.A. Willis. Observation of nanosecond laser-induced phase explosion in aluminum. *Applied Physics Letters*, 89:211121, 2006.

[58] L.J. Radziemski and D.A. Cremers. *Laser-induced Plasmas and Applications*. Marcel Dekker, 1989.

[59] A. Bogaerts, Z. Chen, and D. Bleiner. Laser ablation of copper in different background gases: Comparative study by numerical modeling and experiments. *Journal of Analytical Atomic Spectrometry*, 21(4):384–395, 2006.

[60] X. Mao and R.E. Russo. Observation of plasma shielding by measuring transmitted and reflected laser pulse temporal profiles. *Applied Physics A*, 64:1–6, 1997.

[61] Jose M. Vadillo, Carmen C. García, Jose F. Alcántara, and J. Javier Laserna. Thermal-to-plasma transitions and energy thresholds in laser ablated metals monitored by atomic emission/mass spectrometry coincidence analysis. *Spectrochimica Acta Part B*, 60:948–954, 2005.

[62] X.L. Mao, A.C. Ciocan, O.V. Borisov, and R.E. Russo. Laser ablation processes investigated using icp-aes. *Applied Surface Science*, 127-129:262–268, 1998.

[63] P. T. Mannion, J. Magee, E. Coyne, G. M. O'Connor, and T. J. Glynn. The effect of damage accumulation behaviour on ablation thresholds and damage morphology in ultrafast laser micro-machining of common metals in air. *Applied Surface Science*, 233:275–287, 2004.

[64] R. Le Harzic, N. Huot, E. Audouard, C. Jonin, P. Laporte, S. Valette, A. Fraczkiewicz, and R. Fortunier. Comparison of heat-affected zones due to nanosecond and femtosecond laser pulses using transmission electronic microscopy. *Applied Physics Letters*, 80(21):3886–3888, 2002.

[65] A. Semerok, B. Sallé, J.F. Wagner, and G. Petite. Femtosecond, picosecond, and nanosecond laser microablation: Laser plasma and crater investigation. *Laser and Particle Beams*, 20:67–72, 2002.

[66] R.E. Russo, X.L. Mao, O.V. Borisov, and H. Liu. Influence of wavelength on fractionation in laser ablation icp-ms. *Journal of Analytical Atomic Spectrometry*, 15: 1115–1120, 2000.

[67] I. Horn, M. Guillong, and D. Günther. Wavelength dependant ablation rates for metals and silicate glasses using homogenized laser beam profiles—implications for la–icp-ms. *Applied Surface Science*, 182:91–102, 2001.

Bibliography for Chapter 3

[1] W. C. Wiley and I. H. McLaren. Time-of-flight mass spectrometer with improved resolution. *Review of Scientific Instruments*, 26(12):1150–1157, 1955.

[2] Boris A. Mamyrin, VI Karataev, and DV Shmikk. Mass-reflectron, a new nonmagnetic time-of-flight high-resolution mass-spectrometer. *Zhurnal Eksperimentalnoi i Teoreticheskoi Fiziki*, 64:82–89, 1973.

[3] Jordan inc. website, http://www.rmjordan.com/.

[4] Ryan J. Wenzel, Urs Matter, Lothar Schultheis, and Renato Zenobi. Analysis of megadalton ions using cryodetection maldi time-of-flight mass spectrometry. *Analytical Chemistry*, 77:4329–4337, 2005.

[5] C. C. García, Jose M. Vadillo, J. Ruiz, and J.J. Laserna. Nanometric in-depth characterization of p diffusion and tio_2 antireflective coatings in solar cells by laser ionization time-of-flight mass spectrometry. *Journal of Analytical Atomic Spectrometry*, 18:779–782, 2003.

[6] C.C. García, J.M. Vadillo, J. Ruiz, and J.J. Laserna. Ion extraction effects on the in-depth analysis of layered samples by time-of-flight mass spectrometry of laser-induced plasmas. *Journal of Analytical Atomic Spectrometry*, 17:929–932, 2002.

Bibliography for Chapter 4

[1] R. E. Hönig and J. R. Woolston. Laser-induced emission of electrons, ions, and neutral atoms from solid surfaces. *Applied Physics Letters*, 2(7):138–139, 1963.

[2] L. Moenke-Blankenburg. *Laser Microanalysis*. Wiley, 1989.

[3] L.J. Radziemski and D.A. Cremers. *Laser-induced Plasmas and Applications*. Marcel Dekker, 1989.

[4] C. C. García, Jose M. Vadillo, J. Ruiz, and J.J. Laserna. Nanometric in-depth characterization of p diffusion and tio_2 antireflective coatings in solar cells by laser ionization time-of-flight mass spectrometry. *Journal of Analytical Atomic Spectrometry*, 18:779–782, 2003.

[5] D. Günther and B. Hattendorf. Solid sample analysis using laser-ablation- inductively coupled plasma mass spectometry. *Trends in Analytical Chemistry*, 24: 255–265, 2005.

[6] Renato Zenobi and Richard Knochenmuss. Ion formation in maldi mass spectrometry. *Mass Spectrometry Reviews*, 17:337–366, 1999.

[7] Michael Karas and Ralf Krüger. Ion formation in maldi: the cluster ionization mechanism. *Chemical Reviews*, 103(2):427–440, 2003.

[8] L. Van Vaeck, J. Bennett, W. Lauwers, A. Vertes, and R. Gijbels. Laser microprobe mass spectrometry: possibilities and limitations. *Mikrochimica Acta III*, III:283–303, 1990.

[9] J.M. Vadillo and J.J. Laserna. Laser-induced breakdown spectrometry: truly a surface analytical tool. *Spectrochimica Acta Part B*, 59:147–161, 2004.

[10] A. Bogaerts, Z.Y. Chen, R. Gijbels, and A. Vertes. Laser ablation for analytical sampling: what can we learn from modeling? *Spectrochimica Acta Part B*, 58(11): 1867–1893, 2003.

[11] G.P. Gupta and B.M. Suri. Vapour and plasma ignition thresholds for visible pulsed-laser ablation of metallic targets. *Applied Surface Science*, 230:398–403, 2004.

[12] A. Vertes, M. De Wolf, P. Juhasz, and R. Gijbels. Threshold conditions of plasma ignition in laser ionization mass spectrometry of solids. *Analytical Chemistry*, 61: 1029–1035, 1989.

[13] A. Vertes, P. Juhasz, L. Balazs, and R. Gijbels. *Microbeam Analysis*, chapter Target heating, plasma formation and expansion processes during laser ionization, pages 273–276. San Francisco Press, 1989.

[14] J.F. Ready. *Effects of High-Power Laser Radiation*. Academic Press, 1971.

[15] L. Balazs, R. Gijbels, and A. Vertes. Expansion of laser-generated plumes near the plasma ignition threshold. *Analytical Chemistry*, 63:314–320, 1991.

[16] Jose F. Alcántara, Jose M. Vadillo, and J. Javier Laserna. Two-pulse delayed 532-nm laser ionization of metals using collinear subthreshold beams. *Rapid Communications in Mass Spectrometry*, 22:1999–2005, 2008.

[17] Jose F. Alcántara, J.M. Vadillo, and J.J. Laserna. Subthreshold two-pulse time-delayed laser ionization of cu. *Applied Physics A*, 92:963–967, 2008.

[18] R. Haglund. Microscopic and mesoscopic aspects of laser-induced desorption and ablation. *Applied Surface Science*, 96-98:1–13, 1996.

[19] Jose M. Vadillo, Carmen C. García, Jose F. Alcántara, and J. Javier Laserna. Thermal-to-plasma transitions and energy thresholds in laser ablated metals monitored by atomic emission/mass spectrometry coincidence analysis. *Spectrochimica Acta Part B*, 60:948–954, 2005.

[20] C.C. García, J.M. Vadillo, S. Palanco, J. Ruiz, and J.J. Laserna. Comparative analysis of layered materials using laser-induced plasma spectrometry (lips) and laser-ionization time-of-flight mass spectrometry (li-tofms). *Spectrochimimica Acta Part B*, 56:923–931, 2001.

[21] R.E. Russo, X.L. Mao, O.V. Borisov, and H. Liu. Influence of wavelength on fractionation in laser ablation icp-ms. *Journal of Analytical Atomic Spectrometry*, 15: 1115–1120, 2000.

[22] L.M. Cabalín and J.J. Laserna. Experimental determination of laser breakdown thresholds of metals under nanosecond q-switched laser operation. *Spectrochimica Acta Part B*, 53:723–730, 1998.

[23] M.J. Van Stipdonk, E.A. Schweikert, and M.A. Park. Coincidence measurements in mass spectrometry. *Journal of Mass Spectrometry*, 32:1151–1161, 1997.

[24] C.W. Diehnelt, R.D. English, M.J. Van Stipdonk, and E.A. Schweikert. Coincidence experiments in desorption mass spectrometry. *Nuclear Instruments and Methods B*, 193:883–890, 2002.

[25] J.K. Cobb and J.J. Murray. Laser beam-induced electron and ion emission from metal foils. *British Journal of Applied Physics*, 16:271–273, 1965.

[26] R. Knochenmuss. Photoionization pathways and free electrons in uv-maldi. *Analytical Chemistry*, 76:3179–3184, 2004.

[27] W. Marine, N.M. Bulgarova, L. Patrone, and I. Ozerov. Electronic mechanism of ion expulsion under uv nanosecond laser excitation of silicon: experiment and modeling. *Applied Physics A*, 79:771–774, 2004.

[28] B.E.A. Saleh and M.C Tech. *Fundamentals of Photonics*, chapter Chapter 3. Wiley, 2007.

[29] A. Ingendoh, M. Karas, F. Hillenkamp, and U. Giessmann. Factors affecting the resolution in maldi. *International Journal of Mass Spectrometry*, 131:345–354, 1994.

[30] K. Dreisewerd. The desorption process in maldi. *Chemical Reviews*, 103:395–425, 2003.

[31] A. Hertwig, S. Martin, J. Krüger, and W. Kautek. Interaction area dependence of the ablation threshold of ion-doped glass. *Thin Solid Films*, 453-454:527–530, 2004.

[32] L. Torrisi, A. Borrielli, and D. Margarone. Study on the ablation threshold induced by pulsed lasers at different wavelengths. *Nuclear Instruments and Methods B*, 255:373–379, 2007.

[33] K.R. Chen, J.N. Leboeuf, R.F. Wood, D.B. Geohegan, J.M. Donato, C.L. Liu, and A.A. Puretzky. Laser–solid interaction and dynamics of laser-ablated materials. *Applied Surface Science*, 96-98:45–49, 1996.

[34] E. Matthias, M. Reichling, J. Siegel, O.W. Käding, S. Petzoldt, H. Skurk, P. Bizenberger, and E. Neske. The influence of thermal diffusion on laser ablation of metal films. *Appl. Phys. A*, 58:129–136, 1994.

[35] J. Siegel, K. Ettrich, E.Welsch, and E. Matthias. Uv-laser ablation of ductile and brittle metal films. *Appl. Phys. A*, 64:213–218, 1997.

Bibliography for Chapter 5

[1] Claude Phipps. *Laser Ablation and its Applications*. Springer, 2007.

[2] Martin von Allmen and Andreas Blatter. *Laser-Beam Interactions with Materials: Physical Principles and Applications*. Springer, 2002.

[3] David A. Cremers and A. K. Knight. *Laser-induced breakdown spectroscopy, In Encyclopedia of Analytical Chemistry Vol. 11*. Wiley, 2000.

[4] Joseph Sneddon, Terry L. Thiem, and Yong-III Lee. *Lasers in Analytical Atomic Spectroscopy*. Wiley, 1997.

[5] J.M. Vadillo and J.J. Laserna. Laser-induced breakdown spectrometry: truly a surface analytical tool. *Spectrochimica Acta Part B*, 59:147–161, 2004.

[6] Andrzej W. Miziolek, Vincenzo Palleschi, and Israel Schechter. *Laser Induced Breakdown Spectroscopy*. Cambridge University Press, 2006.

[7] J. König, S. Nolte, and A. Tünnermann. Plasma evolution during metal ablation with ultrashort laser pulses. *Optic Express*, 13(26):10597–10607, 2005.

[8] R.E. Russo, X.L.Mao, H.C. Liu, J.H. Yoo, and S.S.Mao. Time-resolved plasma diagnostics and mass removal during single-pulse laser ablation. *Applied Physics A: Materials Science & Processing*, 69:S887–S894, 1999.

[9] S.S. Mao, X. Mao, R. Greif, and R. E. Russo. Initation of an early-stage plasma during picosecond laser ablation of solids. *Applied Physics Letters*, 77:2464–2466, 2000.

[10] T.D. Bennett, D.J. Krajnovich, and C.P. Grigoropoulos. Separating thermal, electronic and topographic effects in pulsed laser melting and sputtering of gold. *Physical Review Letters*, 76(10):1659–1662, 1996.

[11] A. Bogaerts and Z.Y. Chen. Effect of laser parameters on laser ablation and laser-induced plasma formation: A numerical modeling investigation. *Spectrochimica Acta Part B*, 60(9-10):1280–1307, 2005.

[12] Jose M. Vadillo, Carmen C. García, Jose F. Alcántara, and J. Javier Laserna. Thermal-to-plasma transitions and energy thresholds in laser ablated metals monitored by atomic emission/mass spectrometry coincidence analysis. *Spectrochimica Acta Part B*, 60:948–954, 2005.

[13] S. Georgiou and A. Koubenakis. Laser-induced material ejection from model molecular solids and liquids: Mechanisms, implications, and applications. *Chemical Reviews*, 103:343–393, 2003.

[14] A. Bogaerts, Z.Y. Chen, R. Gijbels, and A. Vertes. Laser ablation for analytical sampling: what can we learn from modeling? *Spectrochimica Acta Part B*, 58(11): 1867–1893, 2003.

[15] C. Porneala and D.A. Willis. Observation of nanosecond laser-induced phase explosion in aluminum. *Applied Physics Letters*, 89:211121, 2006.

[16] J. Solis, F. Vega, C.N. Afonso, E. Georgiou, D. Charalambidis, and 1993; 74(6): 4271-4273. C. Fotakis, J. Appl. Phys. Evidence of a nonthermal mechanism for ejection of ions and neutrals during excimer laser ablation of ge. *Journal of Applied Physics*, 74(6):4271–4273, 1993.

[17] J. Chen, V. Liberman, J.P. O´Neil, Z. Wu, and R.M. Osgood. Ultraviolet laser-induced ion emission from silicon. *J. Vac. Sci. Technol. A*, 6(3):1426–1427, 1988.

[18] X. Tang, M. Sadeghi, Z. Olumee, and Akos Vertes. Matrix-assisted laser desorption ionization by two collinear subthreshold laser pulses. *Rapid Communications in Mass Spectrometry*, 11:484–488, 1997.

[19] Richard Knochenmuss and Akos Vertes. Time-delayed 2-pulse studies of maldi matrix ionization mechanisms. *Journal of Physical Chemistry Part B*, 104:5406–5410, 2000.

[20] J.R. Millard, M. Yang, and J.P. Reilly. Pulse rate dependence of laser desorption and ionization of molecules on thin metal films. 1. measurements of pulse rate dependence and fraction of molecules desorbed. *Journal of Physical Chemistry*, 95:4045–4050, 1991.

[21] K.H. Song and X.F. Xu. Explosive phase transformation in excimer laser ablation. *Applied Surface Science*, 129:111–116, 1998.

[22] J. Boneberg, O. Yavas, B. Mierswa, and P. Leiderer. Optical reflectivity of si above the melting point. *Physica Status Solidi B*, 174:295–300, 1992.

[23] C.C. García, J.M. Vadillo, J. Ruiz, and J.J. Laserna. Ion extraction effects on the in-depth analysis of layered samples by time-of-flight mass spectrometry of laser-induced plasmas. *Journal of Analytical Atomic Spectrometry*, 17:929–932, 2002.

[24] T.D. Bennett, C.P. Grigoropoulos, and D.J. Krajnovic. Near-threshold laser sputtering of gold. *Journal of Applied Physics*, 77:849–864, 1995.

Bibliography for Chapter 6

[1] Akos Vertes, Renaat Gijbels, and Fred Adams. *Laser Ionization Mass Analysis*. Wiley, 1993.

[2] D.M. Lubman. *Lasers and mass spectrometry*. Oxford University Press, 1990.

[3] F. Hillenkamp and J. Peter-Katalinic. *MALDI MS: A Practical Guide to Instrumentation, Methods and Applications*. Wiley, 2007.

[4] Jose F. Alcántara, Jose M. Vadillo, and J. Javier Laserna. Two-pulse delayed 532-nm laser ionization of metals using collinear subthreshold beams. *Rapid Communications in Mass Spectrometry*, 22:1999–2005, 2008.

[5] Jose F. Alcántara, J.M. Vadillo, and J.J. Laserna. Subthreshold two-pulse time-delayed laser ionization of cu. *Applied Physics A*, 92:963–967, 2008.

[6] G. F. Adams and R. W. Shaw. Chemical reactions in energetic materials. *Annual Review of Physical Chemistry*, 43:331–340, 1992.

[7] D. F. McMillen, D. C. Erlich, C. He, C. H. Becker, and D. A. Shockey. Fracture-induced and thermal decomposition of nto using laser ionization mass spectrometry. *Combustion and Flame*, 111(3):133–160, 1997.

[8] K. Tönnies, R.P. Schmid, C. Weickhardt, J. Reif, and J. Grotemeyer. Multiphoton ionization of nitrotoluenes by means of ultrashort laser pulses. *International Journal of Mass Spectrometry*, 206:245–250, 2001.

[9] C. Kosmidis, K.W.D. Ledingham, A. Clark, A. Marshall, R. Jennings, J. Sander, and R.P. Singhal. On the dissociation pathways of nitrobenzene. *International Journal of Mass Spectrometry and Ion Processes*, 135:229–242, 1994.

[10] D. B. Galloway, J. A. Bartz, L. G. Huey, and F. F. Crim. Pathways and kinetic energy disposal in the photodissociation of nitrobencene. *Journal of Chemical Physics*, 98: 2107–2114, 1993.

[11] Christopher Mullen, Michael J. Coggiola, and Harald Oser. Femtosecond laser photoionization time-of-flight mass spectrometry of nitro-aromatic explosives and explosives related compounds. *Journal of the American Society for Mass Spectrometry*, 20(3):419–429, 2009.

[12] J. Akhavan. *The Chemistry Of Explosives (2nd Ed.)*. 2004.

[13] Jeffrey I. Steinfeld. Explosives detection: A challenge for physical chemistry. *Annual Review of Physical Chemistry*, 49:203–232, 1998.

[14] E. Schram, F. Mühlberger, S. Mitsckke, G. Reichardt, R. Schulte-Ladbeck, M. Pütz, and R. Zimmermann. Schram e, mühlberger f, mitsckke s, reichardt g, schulte-ladbeck r, pütz m, zimmermann r (2008) appl spectrosc 62:238-247. *Applied Spectroscopy*, 62:238–247, 2008.

[15] C.C. García, J.M. Vadillo, S. Palanco, J. Ruiz, and J.J. Laserna. Comparative analysis of layered materials using laser-induced plasma spectrometry (lips) and laser-ionization time-of-flight mass spectrometry (li-tofms). *Spectrochimimica Acta Part B*, 56:923–931, 2001.

[16] Jose M. Vadillo, J.M.Fernández Romero, C. Rodríguez, and J.J. Laserna. Effect of plasma shielding on laser ablation rate of pure metals at reduced pressure. *Surface Interface Analysis*, 27:1009–1015, 1999.

[17] Jose M. Vadillo, Carmen C. García, Jose F. Alcántara, and J. Javier Laserna. Thermal-to-plasma transitions and energy thresholds in laser ablated metals monitored by atomic emission/mass spectrometry coincidence analysis. *Spectrochimica Acta Part B*, 60:948–954, 2005.

[18] S. M. Hankin, A. D. Tasker, L. Robson, K. W. D. Ledingham, X. Fang, P. McKenna, T. McCanny, R. P. Singhal, C. Kosmidis, P. Tzallas, D. A. Jaroszynski, D. R. Jones, R. C. Issac, , and S. Jamison. Femtosecond laser time-of-flight mass spectrometry of labile molecular analytes: laser-desorbed nitro-aromatic molecules. *Rapid Communications in Mass Spectrometry*, 16:111–116, 2002.

[19] D.L. Huestis, C. Mullen, and H. Oser M.J. Coggiola. Laser-ionization mass spectrometry of explosives and chemical warfare simulants. *International Journal of High Speed Electronics and Systems*, 18(1):159–165, 2008.

[20] V. C. Jyothi Bhasu, M. Munawar Chaudhri, and J. Housden. Rapid mass spectrometric analysis of fragments of trinitrotoluene, picric acid and tetryl generated by laser irradiation. *Journal of Materials Science*, 26:2199–2207, 1991.

[21] R. Martin Smith. *Understanding mass spectra: a basic approach*. Wiley, 2004.

[22] B.V. Pond, C. Mullen, I. Suarez, J. Kessler, K. Briggs, S.E. Young, M.J. Coggiola, D.R. Crosley, and H. Oser. Detection of explosive-related compounds by laser photoionization time-of-flight mass spectrometry. *Applied Physics A*, 86:735–742, 2007.

Bibliography for Chapter 7

[1] E. A. Ash & G. Nicholls. Super-resolution aperture scanning microscope. *Nature*, 237:510–512, 1972.

[2] J. Sabine Becker and Hans-Joachim Dietze. State-of-the-art in inorganic mass spectrometry for analysis of high-purity materials. *International Journal of Mass Spectrometry*, 228(2-3):127 – 150, 2003. Special Issue: In honour of Helmut Schwarz.

[3] R. N. S. Sodhi. Time-of-flight secondary ion mass spectrometry (tof-sims): - versatility in chemical and imaging surface analysis. *Analyst*, 129(6):483–487, 2004.

[4] D. Günther and B. Hattendorf. Solid sample analysis using laser-ablation- inductively coupled plasma mass spectometry. *Trends in Analytical Chemistry*, 24: 255–265, 2005.

[5] E. Abbe. Beitrage zur theorie des mikroskops und der mikroskopischen wahrnehmung. *Archiv für mikroskopische Anatomie*, 9:413–468, 1873.

[6] E. H. Synge. A suggested model for extending microscopic resolution into the ultra-microscopic region. *Philosophical Magazine*, 6:356–362, 1928.

[7] E. H. Synge. An application of piezo-electricity to microscopy. *Philosophical Magazine*, 13:297–300, 1932.

[8] L. Novotny. *The history of near-field optics*, volume 50, chapter 5, pages 137–184. 2008.

[9] G. Binnig, H. Rohrer, C. Gerber, and E. Weibel. Tunneling through a controllable vacuum gap. *Applied Physics Letters*, 40:178–180, 1982.

[10] D.W. Pohl, W.Denk, and M.Lanz. Optical stethoscopy: Image recording with resolution lambda/20. *Applied Physics Letters*, 44:651–653, 1984.

[11] E. Bailo and V. Deckert. Tip-enhanced raman scattering. *Chemical Society Reviews*, 37(5):921–930, 2008.

[12] J. S. Becker, A. Gorbunoff, M. Zoriy, A. Izmer, and M. Kayser. Evidence of near-field laser ablation inductively coupled plasma mass spectrometry (nf-la-icp-ms) at nanometre scale for elemental and isotopic analysis on gels and biological samples. *Journal of Analytical Atomic Spectrometry*, 21(1):19–25, 2006.

[13] M. V. Zoriy, M. Kayser, and J. S. Becker. Possibility of nano-local element analysis by near-field laser ablation inductively coupled plasma mass spectrometry (la-icp-ms): New experimental arrangement and first application. *International Journal of Mass Spectrometry*, 273(3):151–155, 2008.

[14] Alexander Siegel. Femtosekunden-laser-materialablation im optischen nahfeld. Master's thesis, Fachhochschule Koblenz, 2006.

[15] Isas website, http://www.isas.de/.

[16] E. Betzig, J. K. Trautman, T. D. Harris, J. S. Weiner, and R. L. Kostelak. Breaking the diffraction barrier: Optical microscopy on a nanometric scale. *Science*, 251 (5000):1468–1470, 1991.

[17] J. Jersch, F. Demming, L.J. Hildenhagen, and K. Dickmann. Field enhancement of optical radiation in the nearfield of scanning probemicroscope tips. *Appl. Phys. A*, 66:29–34, 1998.

[18] Raoul Stöckle, Beate Sick, Bert Hecht, Urs P. Wild, Christian Fokas, Volker Deckert, and Renato Zenobi. High-quality near-field optical probes by tube etching. *Appl. Phys. Lett.*, 75:160–162, 1999.

[19] David J. Hwang, Hojeong Jeon, Costas P. Grigoropoulos, Jong Yoo, and Richard E. Russo. Laser ablation-induced spectral plasma characteristics in optical far- and near fields. *Journal of Applied Physics*, 104(1):013110, 2008.

[20] D. Hwang, S. . Ryu, N. Misra, H. Jeon, and C. P. Grigoropoulos. Nanoscale laser processing and diagnostics. *Applied Physics A: Materials Science and Processing*, pages 1–18, 2009. Article in Press.

Appendix A

Source Code of LabVIEW^{TM} Software

Here, the source code for the MaSAS LabVIEW^{TM} software developed in our laboratory is shown. The LabVIEW code will be shown in the form of screenshots. Our software uses drivers and libraries copyrighted by National Instrument and Tektronix to connect to the oscilloscope using LabVIEW. The piece of software developed in our laboratory is free software and it is licensed under the terms of the General Public License.[1]

The software is basically a while-loop that can be turn off at choice. Procedure notes for the oscilloscope are shown in Fig. A.1. A few variables are set outside of the loop and are shown in Fig. A.2. While the loop is active, the software contacts the oscilloscope and extracts the desired waveform. Figures A.3 to A.8 show the block diagram. The first conditional step (Fig. A.3) has three different modes. The default mode is shown in the whole block. The other modes are designed to work with mathematically operated waveforms (Fig. A.4) and Reference waveform (Fig. A.5) saved in the memory of the oscilloscope.

[1] License conditions may be found at http://www.gnu.org/licenses/gpl-3.0.txt, last accessed $13^{th} July, 2009$.

Procedure Notes

Standard Operation

Complete the following standard operation steps to transfer waveform data from an oscilloscope:

1. Select a waveform source.
2. Specify a waveform data format.
3. Specify the number of bytes per data point.
4. Specify the portion of the waveform that you want to transfer.
5. Transfer waveform preamble information.
6. Transfer waveform data from the oscilloscope.

Optimized Operation

Optimized Operation for Step 2

The waveform data in the tkdpo7k Default Instrument Setup VI is in signed integer data point format with the most significant byte transfer first. Therefore, the Fetch Waveform VI does not include this step.

Optimized Operation for Step 4

The tkdpo7k Fetch Waveform VI and the tkdpo7k Default Instrument Setup VI transfer the whole waveform from an instrument buffer. Therefore, the tkdpo7k Fetch Waveform VI does not include this step.

Other Considerations

You must have knowledge of different acquisition modes to calculate the data width for a waveform. You also must choose a method to scale raw waveform data. Therefore, this VI includes a step to specify the acquisition mode before specifying the waveform data width. You must scale the data this VI retrieves from an instrument to a format that users can understand.

After performing the above optimization, complete the following optimized operation steps to transfer waveform data from an oscilloscope:

1. Select a waveform source.
2. Query the acquisition mode.
3. Specify the number of bytes per data point.
4. Transfer waveform preamble information.
5. Transfer waveform data from the oscilloscope.
6. Scale raw waveform data.

Detailed Steps

The following steps detail the behavior of this VI:

1. Select a waveform source.
2. Query and determine the acquisition mode. A correct determination is critical to steps 3 and 6.

Acquisition Mode	Data Width
Normal	1
Peak Detect	1
Hi Res	2
Envelope	1
Average	2

3. Specify the number of bytes per data point. For the Hi Res or Average acquisition modes, set the data width to 2. For all other acquisition modes, set the data width to 1.
4. Transfer the waveform preamble information. Necessary preamble information includes XZero, XIncrement, YMultiplier, YOffset, and YZero. This VI uses XZero and XIncrement to configure the x-axis of output waveforms and uses YMultiplier, YOffset, and YZero to scale data values. This VI then parses the return string of the preamble query in step 6.
5. Transfer waveform data from the oscilloscope.
   5.1 Perform a CURV? query.
   5.2 Determine how many digits make up the entry for the number of bytes.
   5.3 Read the data size.
   5.4 Call the VISA Read VI repeatedly with a buffer size of 10000 until you obtain as much data as the data size specifies. Use an 8-bit array to store the raw waveform data you obtain.
   5.5 Continue reading the data remaining in the instrument buffer until the buffer is empty.
6. Scale the raw waveform data.
   6.1 Cast the waveform data to a 16-bit array if the data width is 2. Split the waveform data into a minimum and a maximum data array if the acquisition mode is Peak Detect or Envelope. This VI skips this step if the data width is 1.
   6.2 Parse the preamble information.
   6.3 Scale the waveform data according to the following formula:
      Data_Value_in_units = (Raw_Data_Value - YOffset) * YMultiplier + YZero
      The resulting waveform data has a unit of volts.
   6.4 Build a waveform graph.

Figure A.1: Procedure notes for the MASAS software.

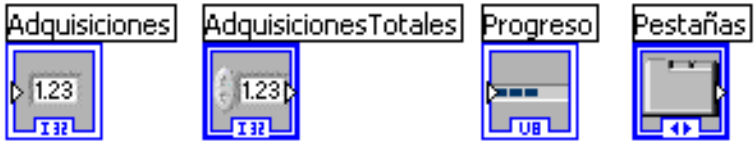

Figure A.2: Along with the while loop running the whole experiment, a few variables were set outside the loop.

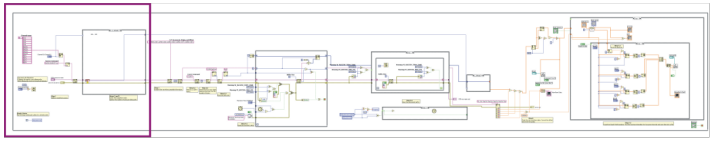

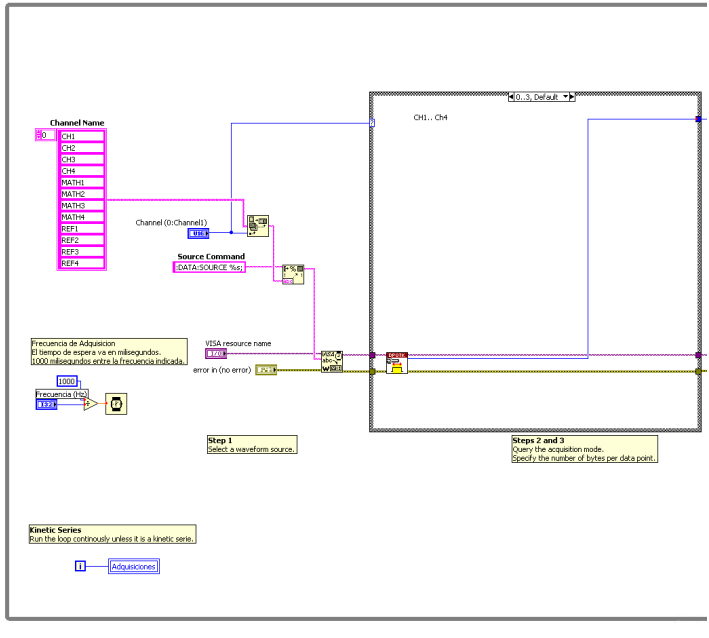

Figure A.3: The diagram block. Continues in Figure A.6.

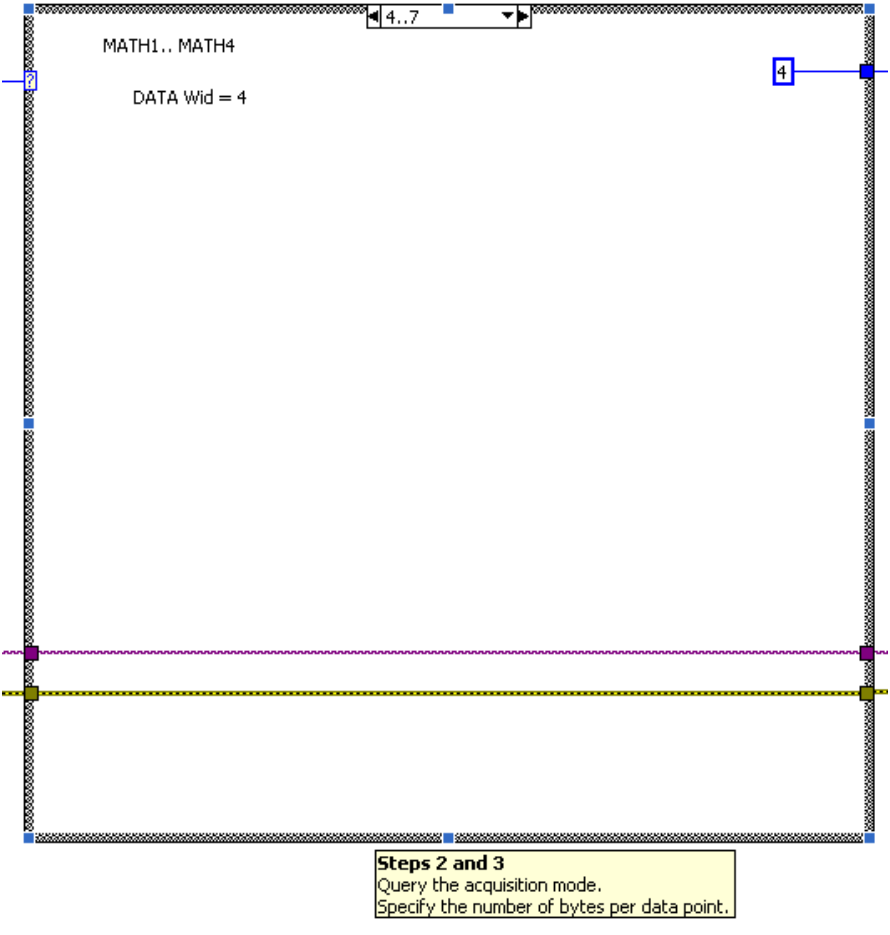

Figure A.4: The diagram block. To capture Math operated Waveforms.

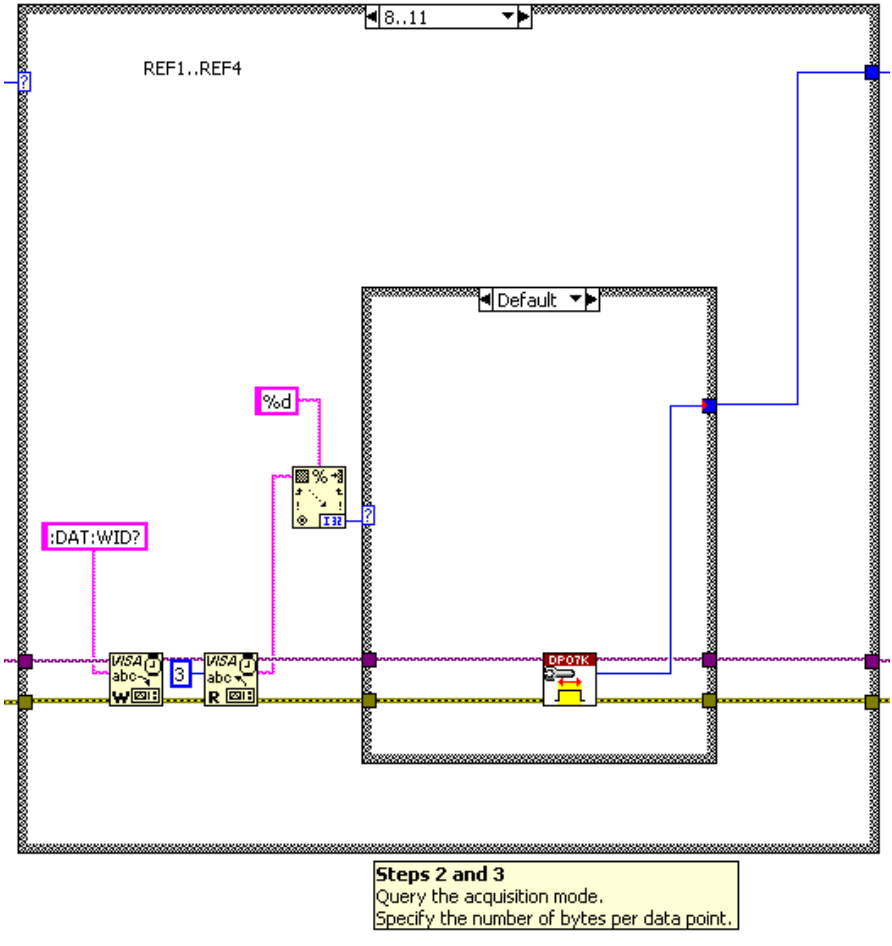

Figure A.5: The diagram block. To capture Reference saved Waveforms.

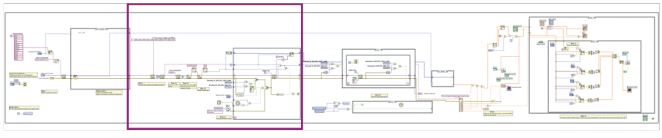

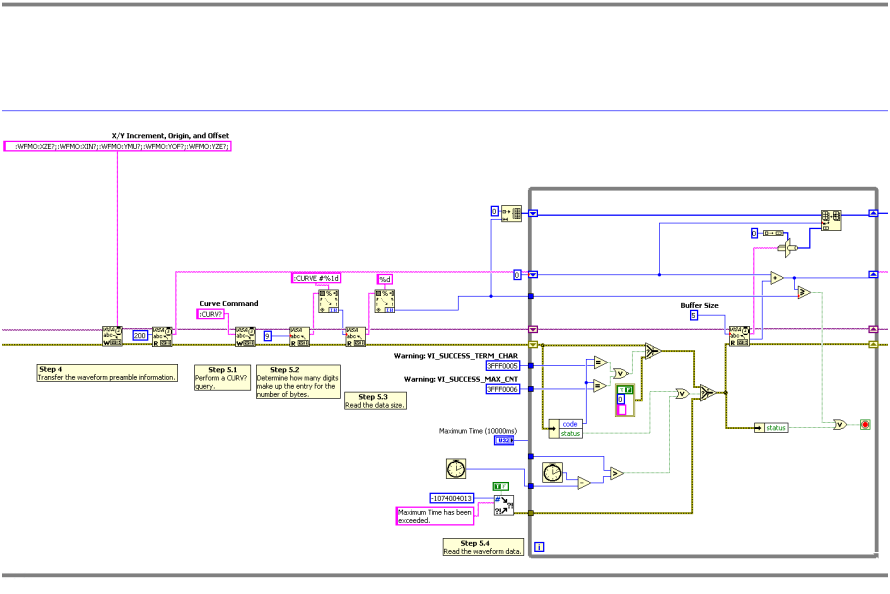

Figure A.6: The diagram block. Comes from Figure A.3. Continues in Figure A.7.

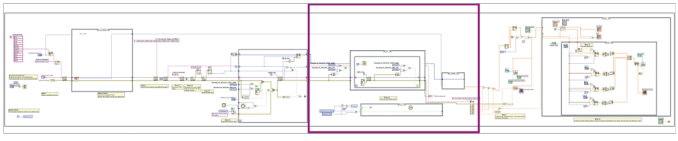

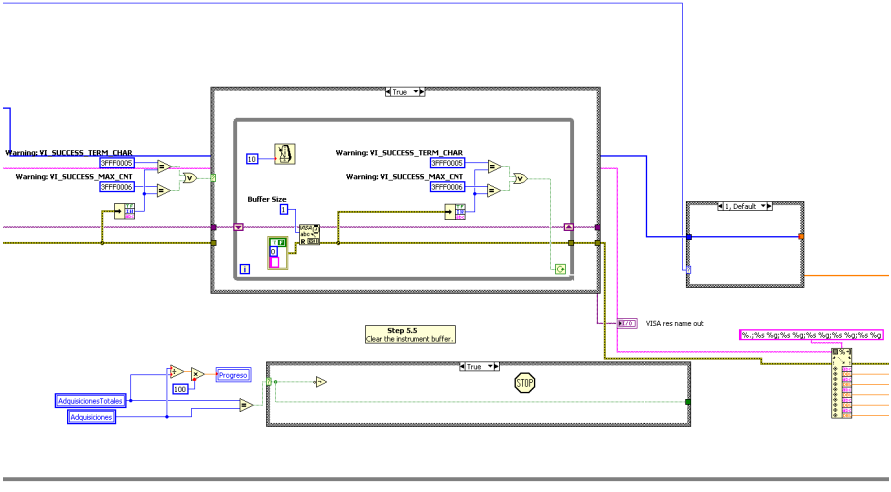

Figure A.7: The diagram block. Comes from Figure A.6. Continues in Figure A.8..

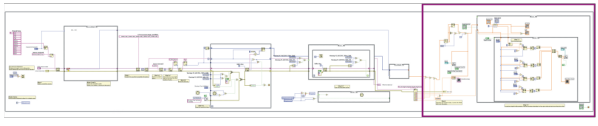

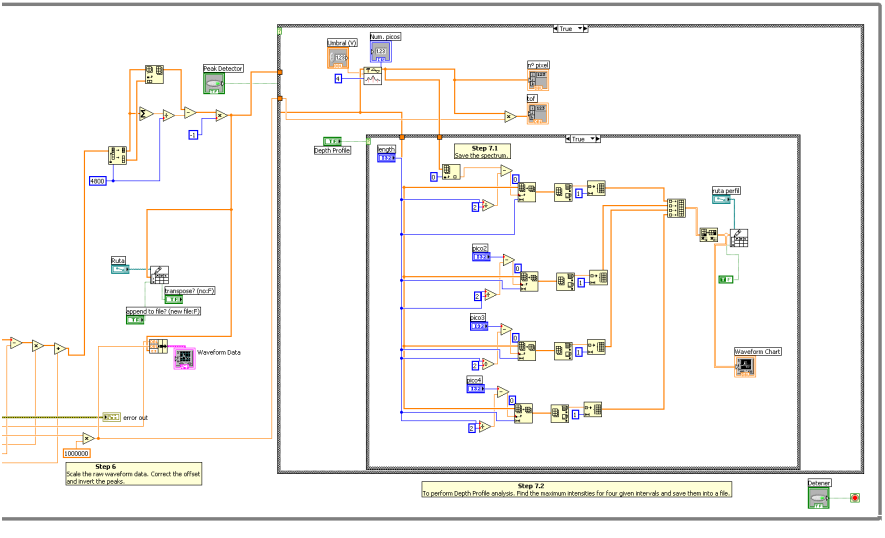

Figure A.8: Final of the the diagram block. Comes from Figure A.7.

Appendix B

Source Code of MATLAB™ Scripts

In this Appendix, the code for the MATLAB™ scripts used for post-processing of acquired data is shown. There are two different routines, depending on the acquiring software used. The first routine, the former one, is used to process data acquired and stored using the TekScope software by Tektronix™. The latter is used to treat stored data acquired using the MASAS Labview application developed in our laboratory, whose block diagram may be found in Appendix A. Both MATLAB™ scripts are free software and are licensed under the Terms and Conditions of the General Public License version 3.0.[1]

B.1 Routine 1, for TekScope Data

```
%
% Script:
% =======
```

[1] License conditions may be found at http://www.gnu.org/licenses/gpl-3.0.txt, last accessed $9^{th} July, 2009$.

```
% fastframe.m
%
% Autor:
% ======
% Jose F. Alcantara (c) 2006-9
%
% Finalidad:
% ==========
% Script para el procesado de datos adquiridos en modo FastFrame
% desde el software TekScope (TekTronix) de un osciloscopio
% digital Tektronix TDS5054B.
%
% Licencia:
% =========
% Este Script esta licenciado como Software Libre bajo la licencia publica
% general GNU GPL 3.0 (ver archivo gpl.txt ubicado en el mismo directorio que
% este script). La copia, modificacion y redistribucion de este script y
% cualquier software derivado esta permitida en tanto se mencione al autor
% y esta nota se mantenga.
%
%

% Queremos construir el string para llamar al archivo
Fecha = input('Introduce la fecha de creacion del archivo = ', 's')

CasiArchivo = [Fecha, '-'];
Extension = '.csv';


% Definimos el primer archivo y el ultimo
PrimerArchivo = input('Primer archivo que sera procesado = ')
UltimoArchivo = input('Ultimo archivo que sera procesado = ')

% Definimos las propiedades del experimento, para guiar la lectura del
% archivo ASCII en el script.
NumEspec = input('Numero de espectros = ')
NumPtos = input('Numero de puntos por espectro = ')
```

```
input('Esta operacion puede durar unos minutos (pulsa ENTER para comenzar)')

% Este es el bucle que procesara los archivos secuencialmente
% del primero al ultimo, se sale cuando se han procesado todos.
while PrimerArchivo <= UltimoArchivo

    PrimerArchivoStr = num2str(PrimerArchivo);
        while length(PrimerArchivoStr) < 3
            PrimerArchivoStr = ['0', PrimerArchivoStr];
        end

    Archivo = [CasiArchivo, PrimerArchivoStr, Extension];
    ArchivoSalida = [CasiArchivo, PrimerArchivoStr, '-proc', Extension];
    Espectros = csvread(Archivo, 0, 4);
    Espectros = reshape(Espectros,NumPtos,[]);



    ciclo = 0;
    % iterar para promediar el fondo y restarlo a cada linea
        while ciclo < NumEspec
            ciclo = ciclo + 1;
            % Eliminamos el fondo considerando los primeros 200 pixels, en
            % los que nunca tenemos iones.
            Fondo = Espectros(1:200,ciclo);
            Offset = Mean(Fondo);
            Espectros(:,ciclo) = Espectros(:,ciclo)*(-1);
            Espectros(:,ciclo) = Espectros(:,ciclo) + Offset;
        end
    % Hacemos la media de los espectros medidos y la guardamos aparte, para
    % evitar hacerla mas adelante de forma manual.
    MediaEspectros = Mean(Espectros,2);
    ArchivoSalidaMedias = [ArchivoSalida, '.media'];
    csvwrite(ArchivoSalidaMedias,MediaEspectros);
    % Escribimos el archivo con los espectros de masas.
    csvwrite(ArchivoSalida,Espectros);
    % Incrementamos el contador y seguimos procesando.
```

```
    PrimerArchivo = PrimerArchivo + 1;
    % Mostramos aviso de control para que el usuario perciba que el pc no
    % se ha bloqueado
    ArchivosQueFaltan = (UltimoArchivo - PrimerArchivo) + 1

end


% Aviso de final de procesado
input('Fin (Pulsa ENTER para salir del script)')

% Borramos todas las variables del espacio de trabajo
% para liberar memoria
clear

%
%
%
% FIN
%
```

B.2 Routine 2, for MASAS Data

```
% Script:
% =======
% reformar.m
%
% Autor:
% ======
% Jose F. Alcantara (c) 2006-9
%
% Finalidad:
% ==========
% Script para el procesado de datos adquiridos en modo Normal+Traspuetos
% desde el software escrito en LabVIEW para controlar
% un osciloscopio digital Tektronix 5054B.
```

```
%
% Licencia:
% =========
% Este Script esta licenciado como Software Libre bajo la licencia publica
% general GNU GPL 3.0 (ver archivo gpl.txt ubicado en el mismo directorio que
% este script). La copia, modificacion y redistribucion de este script y
% cualquier software derivado esta permitida en tanto se mencione al autor
% y esta nota se mantenga.
%
%
%
%
%

% Queremos construir el string para llamar al archivo
Fecha = input('Introduce la fecha de creacion del archivo (AAAAMMDD) = ', 's')

CasiArchivo = [Fecha, '-'];
Extension = '.csv';



% Definimos el primer archivo y el ultimo de la serie que vamos a procesar
PrimerArchivo = input('Primer archivo que sera procesado = ')
UltimoArchivo = input('Ultimo archivo que sera procesado = ')

% Definimos las propiedades del experimento, para guiar la lectura del
% archivo ASCII en el script.
NumEspec = input('Numero de espectros = ')
NumPtos = input('Numero de puntos por espectro = ')

% Aviso, por si fueran muchos archivos...
input('Esta operacion puede durar unos minutos (pulsa ENTER para comenzar)')

% Este es el bucle que procesara los archivos secuencialmente
% del primero al ultimo
while PrimerArchivo <= UltimoArchivo
```

```
    PrimerArchivoStr = num2str(PrimerArchivo);
        while length(PrimerArchivoStr) < 3
            PrimerArchivoStr = ['0', PrimerArchivoStr];
        end

    Archivo = [CasiArchivo, PrimerArchivoStr, Extension];
    ArchivoSalida = [CasiArchivo, PrimerArchivoStr, '-proc', Extension];
    Espectros = csvread(Archivo);
    EspectrosT = reshape(Espectros,NumPtos,[]);
    % escribimos la traspueta
    csvwrite(ArchivoSalida,EspectrosT);
    % Incrementamos en 1 el numero de archivo, para seguir con el bucle.
    PrimerArchivo = PrimerArchivo + 1;
    % Pasamos por pantalla el aviso para que el usuario vea que el
    % ordenador no se ha bloqueado.
    ArchivosQueFaltan = (UltimoArchivo - PrimerArchivo) + 1

end


% Aviso de final de procesado
input('Fin (Pulsa ENTER para salir del script)')

% Borramos todas las variables del espacio de trabajo
% para liberar memoria
clear

%
%
%
% FIN
%
```

Index